

E.T.S. de Ingeniería Industrial,  
Informática y de Telecomunicación

# Test Target for Beacon Alignment in Optical Ground Stations



Bachelor's Degree in  
Telecommunications Engineering

Bachelor's Thesis

Jone Rivas Azpiazu

Dr. Miguel A.G. Laso

Dr. Dirk Giggenbach, IKN (Deutsches Zentrum für Luft- und Raumfahrt)

Pamplona, 10/09/2025



Deutsches Zentrum  
für Luft- und Raumfahrt

upna

Universidad Pública de Navarra  
Nafarroako Unibertsitate Publikoa

## Abstract

Free space optical (FSO) communications are a promising solution for large wireless data transmission, especially with low Earth orbit (LEO) satellite downlinks. A key aspect of ensuring robust communication between the satellite and the optical ground station (OGS), is the proper alignment of the beacon lasers used for indicating the OGS's location to the satellite. Current methods to verify beacon divergence and directional alignment often lack accuracy and reliability and they do not provide both adjustments at the same time.

In this work, a device designed to support beacon alignment in OGSs by combining image processing and measurements taken by photodetectors is presented. The system uses a camera and reflective foils to initially align the beacons as well as capturing its intensity distribution for divergence calculations. The fine directional adjustment is provided by photodetectors, and the receiver power is used to estimate the beacon's divergence. These two methods enable simultaneous directional and divergence adjustment of the beacons. It was evaluated outdoors under realistic conditions, demonstrating its potential as a practical tool for optimizing beacon alignment.

**Keywords:** Free space optical (FSO) communications, optical communications, optical ground station (OGS), beacon alignment, beacon divergence adjustment, low Earth orbit (LEO) satellites, photodetectors, image-based alignment, satellite data downlink, image processing, link budget

## Acknowledgements

I would like to sincerely thank my supervisor at the German Aerospace Center (DLR), Dr. Dirk Giggenbach for his guidance and support through this project and specially for giving me the opportunity to carry out my internship at DLR. To Florian and especially Andrea for their help on developing and testing the Test Target.

I would like to thank my family and friends from Mutriku for always supporting me, even when I was rarely at home.

Finally, I am very thankful to my university colleagues for being by my side throughout my degree, and especially to Idoia and Itzi for their constant support, reminding me that everything can be overcome, even surviving this degree.

# Table of contents

1	Introduction .....	9
2	Theoretical Framework .....	10
2.1	Free Space Optical Communications .....	10
2.1.1	Low Earth Orbit satellites .....	11
2.1.2	Optical Ground Stations .....	11
2.1.2.1	Beacons .....	12
2.2	Gaussian beam .....	13
2.2.1	Propagation characteristics of Gaussian beams .....	15
2.3	Beacon alignment.....	17
2.3.1	Directional alignment .....	17
2.3.2	Divergence adjustment .....	18
2.3.3	Challenges .....	18
2.4	Link budget .....	21
3	Implementation and validation metrics .....	23
3.1	System design .....	23
3.1.1	Beam power detection .....	25
3.1.2	Back-reflecting foil & camera .....	26
3.1.3	Beacon design.....	27
3.2	Components .....	29
3.2.1	Camera.....	29
3.2.1.1	Lens.....	30
3.2.1.2	Filter.....	31
3.2.1	Collimators .....	32
3.2.2	Indium Gallium Arsenide switchable gain photodetector .....	33
3.2.2.1	Lens.....	34
3.2.3	Retroreflective foil.....	35
3.3	Test conditions and validation parameters.....	38
3.3.1	Controller output power test .....	38
3.3.2	Filter Attenuation Test.....	39
3.3.3	Link Budget .....	41
3.3.3.1	Beacon to photodetector Link Budget .....	41
3.3.3.2	Beacon to camera.....	42
3.4	Telemetry .....	45
4	Experimental development.....	47
4.1	Data acquisition .....	48

4.1.1	DAQami.....	49
4.1.2	Vimba X Viewer.....	50
4.1.3	Alignment process .....	51
4.1.4	Divergence calculation .....	52
4.1.4.1	Camera image processing .....	52
4.1.4.2	Photodetector data processing.....	56
4.1.4.3	Interface for real time processing.....	56
4.2	Results & Discussion .....	58
4.2.1	Divergence from camera images .....	58
4.2.2	Divergence from detected power.....	60
4.2.3	Discussion.....	62
5	Conclusion.....	66
5.1	Future work.....	66
6	Bibliography.....	68
7	Annex 1 (Camera interface scripts).....	71
8	Annex 2 (Radio frequency link setup).....	78
8.1	Power beams .....	78
8.1.1	Access Point .....	78
8.1.2	Station.....	81
8.2	MCC DAQ.....	83
8.3	Final setup.....	84

# Figures

Figure 1: Classification of wireless optical communication systems. Modified from [5].....	10
Figure 2: Phases in LEO data downlink where two beacon beams are represented in blue cones pointing to the LEO satellite .....	11
Figure 3: Transmitter diversity (MISO) [13] .....	12
Figure 4: Gaussian distribution [14].....	13
Figure 5: Gaussian beams representation where the beam waist ( $w_0$ ) is defined [15].....	13
Figure 6: Gaussian distribution with the Full Width at Half Maximum and $1/e^2$ diameters marked [16].....	14
Figure 7: A thin lens, with focal length $f$ , is shown inserted in a Gaussian beam. In the modified thin-lens equation, the object is the input beam's waist, located at a distance from the input side of the lens [21] .....	15
Figure 8: a) Convergent beam. b) Collimated beam c) Divergent beam [28] .....	16
Figure 9: Fiber position regarding lenses focus point and convergent (blue), collimated (orange) and divergent (purple) beams.....	16
Figure 10: Beacon beams from OGS (Left) to LEO satellite (Right). a) Converging beacons. b) Parallel beacons. c) Diverging beacons .....	17
Figure 11: Retroreflective Corner Cube use example [23].....	18
Figure 12: Example of adjustable collimator methods by axial translation light source (Left) and use of a mirror (Right) [25] .....	19
Figure 13: Defocusing fiber with larger lens to get larger divergent beam spot. a) Focused fiber with small spot size. b) Defocused fiber with divergent beam .....	19
Figure 14: Example of divergence with conventional fiber (a) and a fiber with an end cap (b) [27].....	20
Figure 15: Losses due to beam divergence [28].....	22
Figure 16: Link distance and locations at DLR Oberpfaffenhofen .....	24
Figure 17: Gaussian distribution shown from different planes [14].....	25
Figure 18: Transmitter design sketches.....	25
Figure 19: Test Target design sketches with sensor mount set up and lenses .....	26
Figure 20: Final sketches from both the Test Target and transmitter side .....	27
Figure 21: Custom beacon setup with components.....	28
Figure 23: Typical responsivity for silicon, InGaAs, and germanium [31].....	29
Figure 22: Goldeye G-130 TEC1 camera and its specifications [30].....	29
Figure 24: Goldeye G-130 TEC1 camera's quantum efficiency [30].....	30
Figure 25: FBH1550-30 filter (left) and its transmission vs wavelength graph [34].....	31
Figure 26: Camera tube setup .....	32
Figure 27: Converging beam schema with fiber getting away from the focus point (left). Diverging beam with fiber getting past the focus point (right) [35] .....	33
Figure 28: PDA20CS2 responsivity at each wavelength graph [36].....	34
Figure 29: Photodetector tube setup.....	35
Figure 30: Retroreflective material options. Sphere with reflective coating on the back (Left) and corner cube (Right) [37] .....	35
Figure 31: Observation angle $\alpha$ (Left) and entrance angle $\beta$ (Right) [37].....	36
Figure 32: Top (Left) and front (Right) view of the camera and laser set up for the retroreflective foil test.....	36
Figure 33: All the retroreflective foils to be tested on a box that was horizontally moved for the test.....	36
Figure 34: Graph for visual representation of input current to output power conversion from the controllers .....	39
Figure 35: Filter test setup.....	40
Figure 36: Colleague's measurements in order to correlate the brightness value of a pixel with the incident power depending on the exposure.....	43
Figure 37: Multifunction Ethernet DAQ Device (MCC E-1608) (Left) and Airmax Powerbeam 5ac gen2 (Right) used for telemetry [39], [40] .....	45
Figure 38: RF Link setup .....	46
Figure 39: Test setup. Test Target at IKN (Left) and Transmitter at GSOC (Right) .....	48
Figure 40: DAQami interface example [41].....	49
Figure 41: Vimba X Viewer interface example [42].....	50

Figure 42: Directional alignment with camera and reflective foil. Camera image with high exposure to see the test target (Left). Lower exposure to show the beam alignment in the test target (Right) .....	51
Figure 43: Directional alignment with photodetectors received power/voltage. Green and red plots are the voltage values of the two photodetectors. X axis is time and Y axis is the voltage value.....	51
Figure 44: Atmospheric turbulences [13].....	52
Figure 45: Single captured image (Left) and the mean of 200 captured images (Right).....	53
Figure 46: Example of captured images with unwanted reflections that were filtered in image processing .....	53
Figure 47: Beam centered and not centered on photodetectors. Center of the beam indicated with a red circle. Vertical cut for intensity distribution below each beam spot. Non-Gaussian distribution (Left) and Gaussian distribution (Right).....	54
Figure 48: Divergence calculation with and without interpolation. Both zoomed in for better representation.....	54
Figure 49: Flow graph of divergence calculation process from camera images .....	55
Figure 50: Interface created for adjustable collimator calibration with low exposure .....	57
Figure 51: Interface created for adjustable collimator calibration with high exposure .....	57
Figure 52: Atmospheric turbulence example: 0.545 mrad beam at 500 $\mu$ s exposure at different times.....	58
Figure 53: Graphical representation of the divergence calculations from camera images with uncentered beam in photodetector and fixed divergence collimators .....	59
Figure 54: Graphical representation of the divergence calculations from camera images with beam uncentered in photodetector from previous test with fixed divergence collimators .....	60
Figure 55: Graphical representation of the results of the received power at the photodetectors with fixed divergence collimators .....	61
Figure 56: Divergence calculation from receiver power .....	62
Figure 57: Comparison graph of calculated divergences from images and detected power as well as the datasheet divergences .....	63
Figure 58: Interface with collimated beams of adjustable collimators .....	64
Figure 59: Interface with two divergent beams of the adjustable collimators.....	65
Figure 60: Interface with one collimated beam (Right) and one divergent beam (Left) of the adjustable collimators.....	65
Figure 61: Interface with the maximum divergence adjustable collimators.....	65
Figure 65: Final setup .....	78
Figure 66: Ip change .....	79
Figure 67: Starting portal .....	79
Figure 68: Access Point's wireless configuration.....	80
Figure 69: Access Point's network configuration.....	80
Figure 70: Access Point's configuration's verifying ping.....	80
Figure 71: Station's wireless configuration .....	81
Figure 72: Station's network configuration .....	81
Figure 73: Station's configuration's verifying ping .....	82
Figure 74: SSID options in the Station antenna 's wireless configuration .....	82
Figure 75: Starting portal where the connection can be seen .....	82
Figure 76: Atablesll pings from notebook to check the connections.....	84

## Tables

Table 1: Transmitter base parameters.....	24
Table 2: Receiver base parameters .....	24
Table 3: FPL1009S laser diode's specifications. Typically centered in 1550 nm (in our case 1562 nm). Typical power of 100 mW [29].....	28
Table 4: Reference, $1/e^2$ divergence and FWHM divergence of fixed collimators .....	32
Table 5: 30 dB gain settings in the InGaAs photodetector [36] .....	33
Table 6: Electronic offset for both photodetectors .....	34
Table 7: Retroreflective material test with the entrance angle of $0^\circ$ .....	37
Table 8: Retroreflective material test with the entrance angle of $7^\circ$ .....	37
Table 9: Measurements for input current to get a set output power .....	38
Table 10: Results for the transmission coefficient calculations for FBH1550-30 filter with 30dB gain .....	40
Table 11: One-way link budget .....	41
Table 12: General data for power to voltage conversion [36] .....	42
Table 13: Power to voltage conversion for photodetector.....	42
Table 14: Camera link budget calculation.....	44
Table 15: Final specifications for test .....	47
Table 16: Components used for the project.....	47
Table 17: Example of divergence calculation from detected power .....	56
Table 18: Divergence calculation results from camera images with fixed divergence collimators .....	58
Table 19: Power detected at the photodetector with the theoretical power for comparison with fixed divergence collimators .....	60
Table 20: Conversion from received power to Full Width at Half Maximum divergence.....	62

## Abbreviations

<b>ASTM</b>	American Society for Testing and Materials
<b>ATP</b>	Acquisition, Pointing and Tracking
<b>BW</b>	Bandwidth
<b>CCR</b>	Corner Cube Retroreflectors
<b>DAQ</b>	Data Acquisition
<b>DLR</b>	Deutsches Zentrum für Luft- und Raumfahrt
<b>FC/APC</b>	Fiber Channel / Angled Physical Contact
<b>FC/PC</b>	Fiber Channel / Physical Contact
<b>FL</b>	Focal Length
<b>FOV</b>	Field of View
<b>FSO</b>	Free Space Optical
<b>FWHM</b>	Full Width at Half Maximum
<b>GSOC</b>	German Space Operation Center
<b>IKN</b>	Institute of Communication and Navigation
<b>IRT</b>	Infrared Turbulence
<b>LEO</b>	Low Earth Orbit
<b>MISO</b>	Multiple Input Single Output
<b>OAP</b>	Off-Axis Parabolic
<b>OGS</b>	Optical Ground Station
<b>PVC</b>	Polyvinyl Chloride
<b>RF</b>	Radio Frequency
<b>SDK</b>	Software Development Kit
<b>SMF</b>	Single Mode Fiber
<b>WD</b>	Working Distance

# 1 Introduction

Free space optical (FSO) communication is increasingly being explored as a solution for satellite data downlinks, particularly for low Earth orbit (LEO) satellites. Compared to traditional radio frequency (RF) systems, FSO offers potential advantages such as higher data rates, lighter equipment, and operation in unlicensed spectrum bands.

However, FSO systems depend on the precise alignment of beacons that point from the optical ground station (OGS) to the satellites, for the satellites to track the OGS correctly. Directional alignment and divergence adjustments of beacon beams are key to precise satellite tracking. Narrow beams offer higher signal power but have smaller alignment tolerances as well as requiring more pointing accuracy. Larger divergences do not require a high pointing accuracy but have lower signal power [1].

Recent literature has proposed dynamic divergence control systems that adapt the beam divergence by changing the link conditions, using variable optics and adaptive designs. In addition, beacon based alignment methods for FSO systems typically use coarse and fine stages [2], [3]. The existence of acquisition, pointing and tracking (ATP) system should also be mentioned, where a combination of fast steering mirrors and gimbals are used to improve angular tracking [1].

Despite these advances, many existing solutions focus on divergence control or precise pointing, but not both simultaneously. In this project, a device for accurate directional alignment and divergence adjustment of beacons is proposed. The device combines hardware and software in a two-step process. A camera and retroreflective foils are used to determinate the beacon's initial directional alignment and its divergence through image processing. Photodetectors are used to measure the received beam power to estimate the divergence and align the beacons precisely. By integrating two adjustment methods, the system allows the operator to both align the beacon's direction and monitor its divergence with high accuracy.

The two main objectives of the work are to provide a practical method for directional alignment of optical ground station's (OGS) beacons, as well as to offer a way to accurately measure the divergence of the beam using photodetectors and camera feedback. This project validates the beacon setup under outdoor experimental conditions, recreating the environment of OGSs.

The thesis is structured into five chapters, starting with the introduction, followed by the theoretical framework. The system design and verification data acquisition are discussed next, followed by the data collection and processing conducted in this project. Finally, an overall summary and conclusions are presented, along with proposed improvements and future research paths for the designed device.

The results demonstrate that this device offers a reliable and effective tool for beacon adjustment in free space optical communications, with the potential to improve the robustness of LEO satellite data downlink by making the beacon pointing more precise.

## 2 Theoretical Framework

The following sections explain the theoretical knowledge required to conduct the different processes involved in executing the project. Free space optical (FSO) communications and their current importance are discussed, as well as their use in low Earth orbit downlink communications and the components that make an optical link work, such as optical ground stations.

As mentioned in the introduction, the thesis focuses on the analysis and verification of the correct adjustment of the beacons used in FSO communications, specifically in optical satellite data downlinks. To do so, this section describes the properties of a Gaussian beam, previously used alignment methods, and both tools and important problems in the alignment process.

### 2.1 Free Space Optical Communications

Right now, fast, secure, and global data connection and transmission are among society's biggest interests. In addition to the traditional use of radio frequency (RF) connections, there is an alternative that offers several benefits, which is discussed in this section. Free space optical (FSO) communication is a type of wireless communication that uses light and lasers to transmit data between two points instead of using RF waves [4].

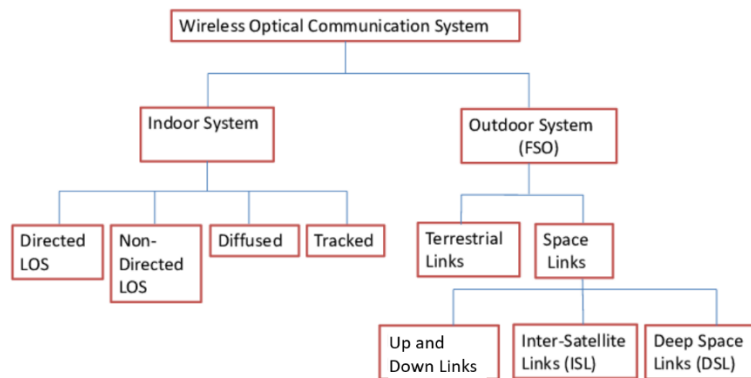


Figure 1: Classification of wireless optical communication systems. Modified from [5]

FSO communication consists of transmitting a beam of light using a laser, where, if the line of sight is clear and unobstructed, the beam is received by a receiver. For the process to be viable, the laser must be well aligned and its orientation calibrated so that only the predetermined receiver establishes communication with the transmitter. This calibration and beam directivity make it more robust against possible unwanted interceptions [6].

In addition, the use of light as a method of data transmission makes it possible to achieve higher speeds when transmitting data, while overcoming the bandwidth limitations of radio frequency communications [7]. Furthermore, the infrastructure required for FSO communications, such as terminals or optical ground stations (OGSs), require less space and material and are generally much cheaper and lighter than those used in radio frequency communications [5].

Although the advantages of free space communications are undeniable, it should be noted that there are significant difficulties in planning and establishing such connections. The atmosphere is a heterogeneous medium that consistently attenuates the transmitted signal due to clouds, rain, and atmospheric turbulence [4].

On the other hand, the precise alignment that provides greater security is not so easy to achieve. This alignment is exactly what this project is focused on. Of the various types of FSO communications, the focus is on downlink communications with low Earth orbit (LEO) satellites.

### 2.1.1 Low Earth Orbit satellites

A low Earth orbit (LEO) satellite is a satellite that orbits the Earth at an altitude typically between 300 km and 2000 km [8]. Low Earth orbit offers various advantages to spacecraft, such as proximity to Earth and low communication latency. LEO satellite data downlinks are the communication links used to transmit data from the satellite to an optical ground station (OGS) on Earth. The most important applications are direct-to-ground downlinks, since the main objective is to download to Earth the increasing amount of data gathered in missions [9].

### 2.1.2 Optical Ground Stations

An optical ground station (OGS) is a terrestrial receiving infrastructure for FSO communications. Unlike radio frequency stations that use parabolic antennas, an OGS uses telescopes to capture the laser beam coming from the satellite.

LEO satellite communications with the OGS work as follows: the OGS telescope acts as a large aperture “antenna” that collects the laser light. When the satellite is in the line of sight, the OGS transmits a beacon signal with the divergence big enough to cover the satellite while the satellite directs its tracking sensor to the OGS. With the beacon transmitted by the OGS, the satellite is able to track the OGS and transmit the downlink signal while the link lasts [9].

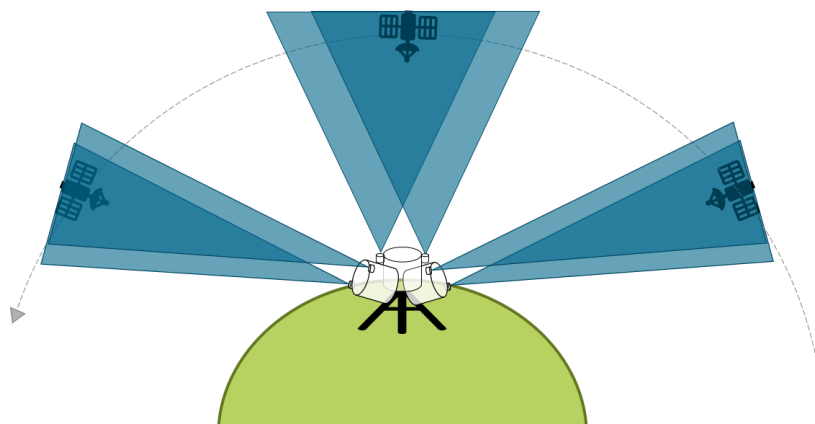


Figure 2: Phases in LEO data downlink where two beacon beams are represented in blue cones pointing to the LEO satellite

Overall, the OGS has two primary functions: to receive the downlink beam from the satellite and to transmit the beacon lasers, enabling the satellite to track the OGS while in orbit.

### 2.1.2.1 Beacons

In free space optical (FSO) satellite communications, a beacon is a continuous or modulated laser beam that acts as a directional guide. It carries no data and serves to enable the satellite and OGS to accurately point and track each other. The beacon signal may be brighter, wider, differently modulated or at a different wavelength than the data beam [10]. These beacons used in OGSs for tracking are the ones the project is based on.

Instead of a narrow, collimated beam with a small divergences around  $100\ \mu\text{rad}$ , beacons often use a more divergent beam of  $500\ \mu\text{rad}$ , for example. To understand this, it is first necessary to explain the three behaviors that a laser beam can exhibit.

A collimated beam of light propagates in a homogeneous medium with a low beam divergence, so that its radius does not undergo significant changes over propagation distances [11]. A divergent beam, on the other hand, increases its spot size while it propagates. Finally, a convergent beam reduces its spot size before increasing it again during propagation. This topic is discussed in more detail in section 2.2.1.

Using a divergent beam is key to an easier tracking. A collimated beam is difficult to track and maintain. A narrower divergence may miss the receiver entirely and it is not eye safe at ground level. A divergent beam creates a large beam spot at the receiver, expanding the “capture area” of the satellite and making detection easier.

However, with the large divergences, the received power at the satellite is too low to transmit high speed data. This is why no data is transmitted through these laser beams, and they are only used for tracking. A compromise between divergence, power and beam spot size must be found to ensemble an effective beacon.

Transmitter diversity should also be noted in order to understand the objective of this project. Transmitter diversity is a technique used in communications to improve link reliability by sending the same information over multiple communication channels. In such a system, two or more spatially separated lasers from the same terminal are used. Since different atmospheric paths experience uncorrelated fading effects, this spatial diversity technique helps overcome atmospheric disturbances. This increases the probability of link acquisition and achieves more stable tracking by reducing fading at the satellite [7], [12].

Another advantage of using multiple transmitters is achieving the same received power at the receiver while using less power per individual transmitter. When using one transmitter, the power at the receiver comes from only one source and is relatively high. By distributing the power, the same received power can be detected due to the superposition of correctly aligned beams. Using lower power in each individual beacon also improves eye safety at ground level.

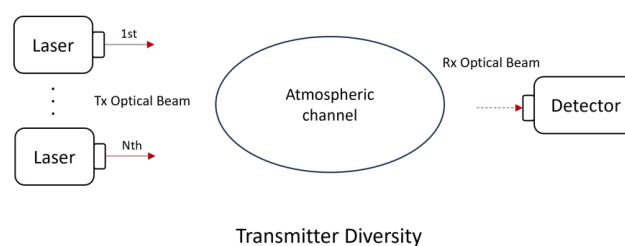


Figure 3: Transmitter diversity (MISO) [13]

## 2.2 Gaussian beam

In optical communications, when an ideal laser emits light, the transverse distribution of the beam follows a Gaussian distribution profile, as shown in Figure 4. This implies that the maximum intensity is at the center of the beam.

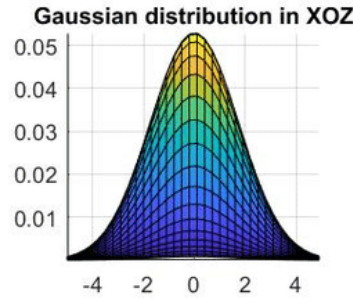


Figure 4: Gaussian distribution [14]

As mentioned, the laser beam is assumed to be Gaussian with an ideal Gaussian distribution. In reality, most laser beams have some deviation from the ideal Gaussian behavior [15]. In this section, some of the key characteristics of Gaussian beams are described, and collimated, divergent and convergent beams are also explained.

First, the different characteristics and standard measurement guides must be understood to properly work with Gaussian beams. When a Gaussian beam propagates through a medium, it has the shape seen in Figure 5.

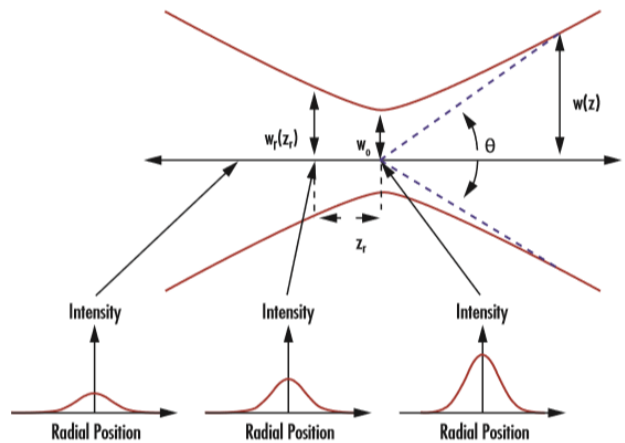


Figure 5: Gaussian beams representation where the beam waist ( $w_0$ ) is defined [15]

The beam propagates in the  $z$  axis, and its amplitude envelope has a Gaussian form. The waist of the beam ( $w_0$ ) is a measure of the beam size at its focus, where the beam width  $w(z)$  is smallest. Due to diffraction, a Gaussian beam converges toward the beam waist and diverges from it [15].

Additionally, the two common ways to measure the divergence of a Gaussian beam should be explained. In Figure 6 shown in the next page, the divergence measured at Full Width at Half Maximum (FWHM) and  $1/e^2$  can be seen.

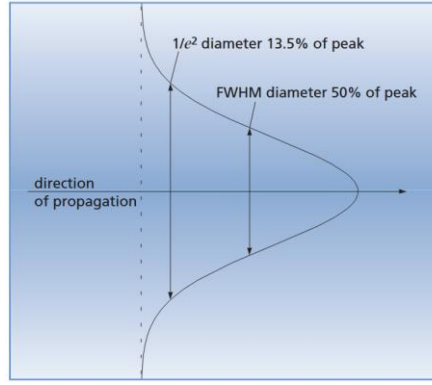


Figure 6: Gaussian distribution with the Full Width at Half Maximum and  $1/e^2$  diameters marked [16]

Both divergences can be related by the following formula, taken from [17].

$$\theta_{FWHM} = \sqrt{\frac{\ln(2)}{2}} \theta_{e^{-2}} \quad (1)$$

Where  $\theta_{FWHM}$  is the full divergence at Full Width at Half Maximum and  $\theta_{e^{-2}}$  is the full divergence at  $1/e^2$ .

A Gaussian beam is an idealized beam whose amplitude envelope is given by a Gaussian function; this also implies that a Gaussian intensity profile can be expressed by the formula below [15].

$$I(r, z) = I_o \exp\left(\frac{-2r^2}{w(z)^2}\right) = P_o \frac{2}{\pi w_0(z)^2} \exp\left(\frac{-2r^2}{w_0(z)^2}\right) \quad (2)$$

Where the  $I_o$  is the maximum intensity at the waist center and  $w_0(z)$  is the beam radius at  $1/e^2$ .

On the other hand, if the intensity distribution is integrated from 0 to  $r$ , the power contained within a radius  $r$  can be obtained (equation 3). This formula is useful for our link budget calculation since the link budget will be adapted for a Gaussian distribution instead of a flat-top one [16].

$$P(r, z) = P_o \left[ 1 - e^{-\frac{2r^2}{w_0^2(z)}} \right] \quad (3)$$

Where  $w_0$  is the beam radius at  $1/e^2$  and  $P_o$  is the total power of the beam that can be calculated with the peak axial intensity ( $I_o$ ) like so [16]:

$$P_o = \frac{1}{2} \pi I_o w_0^2 \quad (4)$$

### 2.2.1 Propagation characteristics of Gaussian beams

When a laser beam propagates through free space or optical components, its shape changes according to Gaussian beam optics. In everyday ray optics, light is portrait as straight lines that can be bent or focused by a lens. However, real laser beams are not just thin rays, diffraction effects and wavefront curvatures must be considered. A gaussian beam can be characterized by two parameters: the beam waist mentioned earlier and the wavelength. From these parameters, one can get the Rayleigh range and divergence angle, for example [18]. For this work, the behavior of beams through single-mode fibers is discussed, since only one wavelength is used for the project.

As the beam travels, its radius evolves according to

$$w(z) = w_o \sqrt{1 + \left(\frac{z}{z_R}\right)^2} \quad (5)$$

Where  $z_R = \frac{\pi w_o^2}{\lambda}$  is the Rayleigh range. This range indicates how long the beam stays nearly constant in size before it starts diverging. This relationship can be used to explain how Gaussian beams alternate between collimated, convergent and divergent forms depending on its position relative to the beam waist and optical elements in the system [15].

When a Gaussian beam passes through a lens, the lens does not just bend the rays, it also changes the wavefront curvature of the beam. This shifts the position of the beam waist and alters its size. The exact output can be calculated using the ABCD matrix method [19], [20].

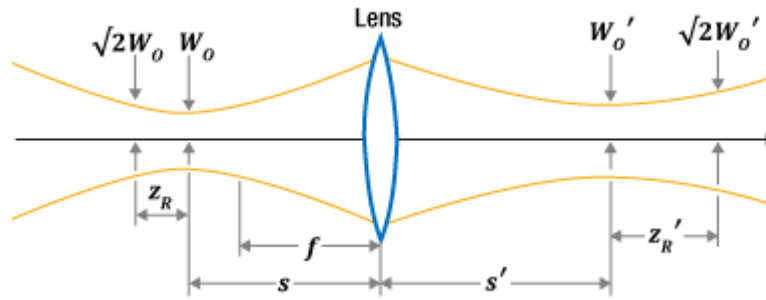


Figure 7: A thin lens, with focal length  $f$ , is shown inserted in a Gaussian beam. In the modified thin-lens equation, the object is the input beam's waist, located at a distance from the input side of the lens [21]

It is important to note that the actual waist positioning does not always coincide with the geometric focal plane predicted by ray optics. It may be shifted due to diffraction effects, initial curvature and input beam divergence. This effect is known as focal shift, where the point of maximum intensity of a diffracted field is located not at the geometric focus, but rather closer to the diffraction plane [22].

A practical case, and the one used in this project, is the light that emerges from an optical fiber. At the fiber exit, the beam behaves like a gaussian beam with the waist located at the fiber's end face. The beam waist is approximately half of the fiber's mode field diameter. Because the waist is so small, the beam immediately begins to diverge. To control the divergence, lenses are placed at the fiber output.

Depending on the lens position and its focal length, the beam can become:

1. **Convergent:** The rays are directed inward towards a focus, where the beam reaches a new waist. This occurs when the fiber waist is placed away from the lens and behind the focal plane (Figure 8 sketch a). Having another waist along the beams path is not eye safe, as a high intensity is gathered at the beam waist. In optical communications, this configuration is generally avoided due to the associated safety risks.
2. **Collimated:** The rays are nearly parallel, so the beam radius remains almost constant over a long distance. This occurs if the fiber waist is placed exactly at the lense's focal plane (Figure 8 sketch b).
3. **Divergent:** The rays are directed outward, and the beam expands immediately after leaving the lens. This occurs when the fiber waist is closer to the lens, and in front of the lense's focal plane (Figure 8 sketch c). In this configuration, the intensity is reduced at long distances, but it is extremely useful for scanning or using them as a beacon.

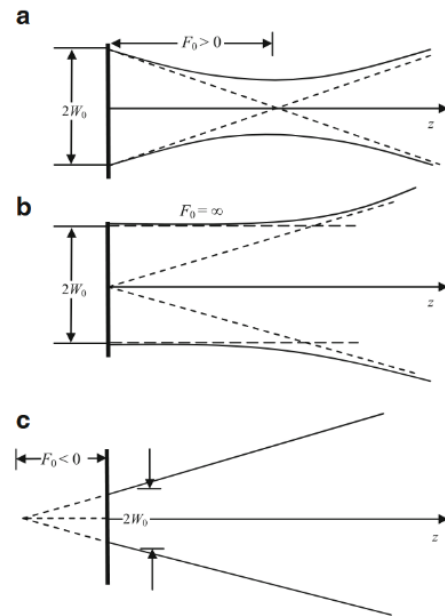


Figure 8: a) Convergent beam. b) Collimated beam c) Divergent beam [28]

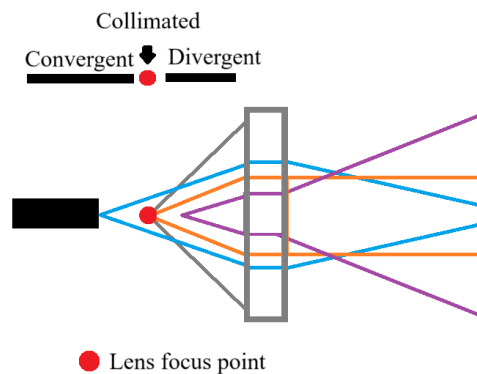


Figure 9: Fiber position regarding lenses focus point and convergent (blue), collimated (orange) and divergent (purple) beams

By choosing the lenses' focal length and their position relative to the beam waist, the behavior of the beam can be adjusted.

## 2.3 Beacon alignment

Beacons adjustment is the focus of this project. Improving and maintaining alignment using optical beacons is essential for reliable FSO communications. As mentioned in section 2.1.2.1, beacons are part of a tracking system used in FSO communications for the satellite to point and track the OGS. If the tracking is not performed correctly, the communication link could be lost. In this section, an overview of the beacon directional alignment and divergence adjustment is provided. The problems and challenges associated with each type of adjustment are also discussed.

### 2.3.1 Directional alignment

Directional alignment ensures that the beacon's beam from the terminal, hits the receiver's detector area, even under movement or vibration. Due to transmitter diversity, more than one beacon is used at the OGS to increase the probability of the satellite tracking the OGS. The chosen beacons must be aligned parallel to each other to ensure that none of them cross over and miss the receiver, as shown in Figure 10.

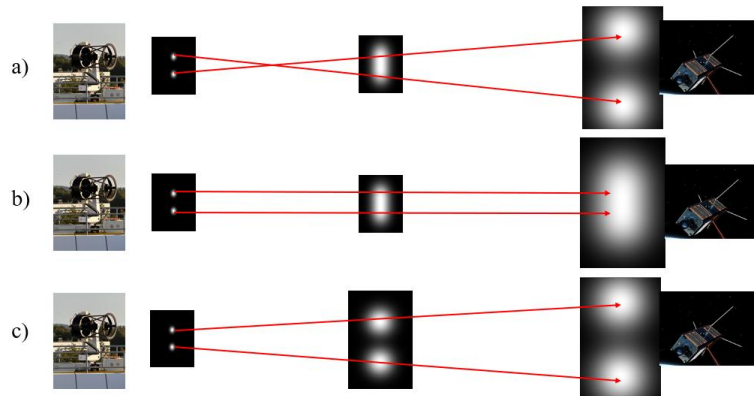


Figure 10: Beacon beams from OGS (Left) to LEO satellite (Right). a) Converging beacons. b) Parallel beacons. c) Diverging beacons

Figure 10 illustrates how the direction of the beacons affects the tracking. If the beacons are not adjusted properly, as in cases a) and c) from Figure 10, tracking is not possible because the satellite's detector does not capture the beacons.

There are several methods to align the direction of the beacons. One example is the use of corner cube retroreflectors (CCR). A CCR reflects light back exactly in the direction it came from, regardless of the incidence angle. This device can be used as follows: one terminal sends a beacon signal and the CCR reflects it back. The transmitting section can then detect the signal and use it for precise alignment. Because CCRs do not require adaptative pointing, they provide a robust alignment method [23].

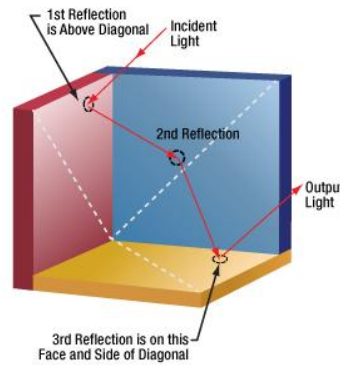


Figure 11: Retroreflective Corner Cube use example [23]

Another method of directional alignment is coarse scanning. There are several patterns, such as the spiral, raster and conical scans [24] to scan the area. When the uncertainty of the pointing direction is large and CCRs are not used, the beacons can be swept around until the receiver on the satellite detects the signal. This method of directional alignment via scanning is used in this project. Instead of using a receiver on the satellite, the device developed for this project is employed.

### 2.3.2 Divergence adjustment

For all the beacons to overlap at the receiver, the beacon divergence must also be carefully adjusted. If the divergence is too large, the received intensity at the receiver may be insufficient, and the satellite's detector may not detect the beams. On the other hand, if the divergence is too small, the beacon signals may not overlap in the receiver, and the alignment becomes more difficult.

In FSO communications, a compromise must be made to achieve sufficient intensity at the detector while still maintaining eye safety measures at ground level.

Currently, verification of the divergence setting can be performed by checking the power distribution on the detector plane or capturing the beam patterns with cameras or position sensitive devices to ensure the beam shape and radius are appropriate.

### 2.3.3 Challenges

To achieve the most accurate alignment possible, several alignment methods have been discussed in the previous section. However, many sources of error exist. While effective, traditional beacon alignment methods present some challenges. For example, scanning can be too time-consuming, which may delay the link setup. Similarly, when considering divergence adjustment, there are many of factors to consider.

To begin with, there are different situations in optical communications where specific divergences are needed for different beams. Collimators with these specific divergences may or may not be available from manufacturers. To achieve the required divergence, the use of adjustable focus collimators is often recommended.

These types of collimators are extremely sensitive and adjusting them to the desired divergence is not an easy task. The adjustment must be performed manually, and it can become a source of error if not properly supervised.

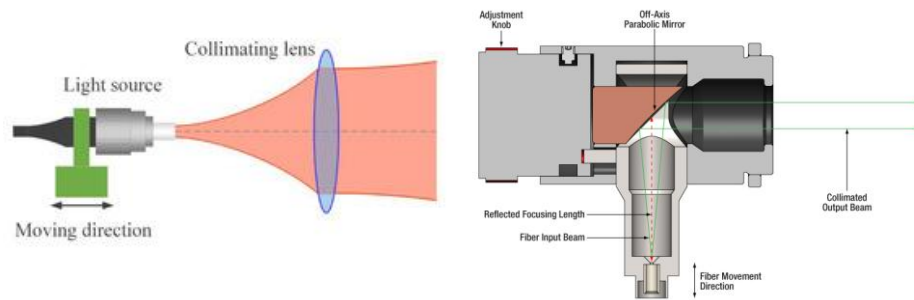


Figure 12: Example of adjustable collimator methods by axial translation light source (Left) and use of a mirror (Right) [25]

On the other hand, when dealing with OGSs with high-power beacon lasers in the range of 1 – 10W, eye safety issues may arise. In some cases, having a larger spot size without changing the divergence is preferable. With the larger spot size, the power is more evenly distributed than with a small beam, making it relatively more eye safe.

To achieve the same divergence with a larger lens, the fiber tip is moved closer to the collimation lens to defocus it and produce a more divergent beam (Figure 13). Collimators usually do not have the option to move the fiber tip closer to the lens and, if they do, it must be adjusted carefully, creating another potential source of error.

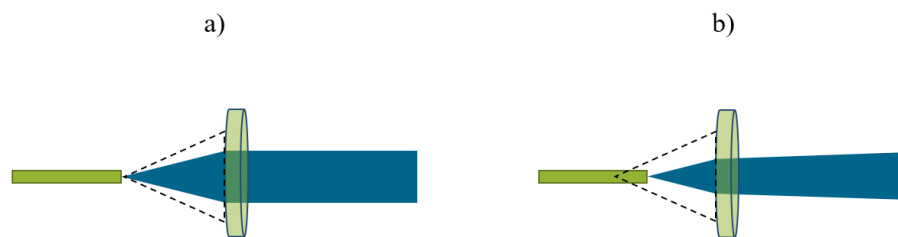


Figure 13: Defocusing fiber with larger lens to get larger divergent beam spot. a) Focused fiber with small spot size. b) Defocused fiber with divergent beam

Lastly, the fiber end-cap should be discussed. For a single-mode (SM) core fiber, the divergence of the beam begins at the fiber exit. The maximum power that can be guided within a fiber is primarily limited by the power density at the fiber end-face. Due to the small diameter of fibers, extremely high-power densities can cause scorching and damage to the end-face [26]. To protect the fiber, end-caps are used. Fiber end-caps are usually cylindrical, homogeneous pieces of optical glass, a few millimeters in length, and without the SM core. Since the end caps contain no waveguide (fiber core), light propagates through these regions as beams which expand toward the ends, reducing the power density at the new end-face.

Because of this change in medium, the divergence of the beam also changes, and it is distorted by the end-cap. As a result, collimators used with the additional end-cap may not properly collimate the beam. To achieve a proper collimation, adjustable focus collimators must be used to focus the fiber correctly. This adjustment is also performed manually and is another source of error.

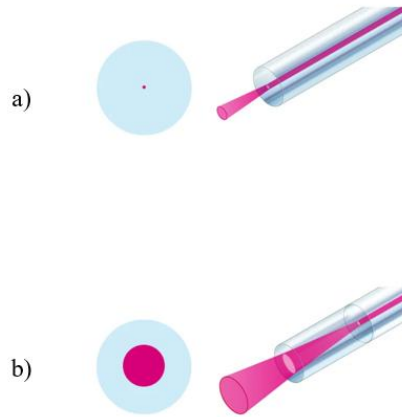


Figure 14: Example of divergence with conventional fiber (a) and a fiber with an end cap (b) [27]

Taking into consideration all the problems and potential sources of error discussed, this project proposes a solution to supervise the beam output. The beam's shape, power and direction must be monitored to detect any possible abnormalities in the beam.

The main objectives are to verify the direction and divergence of the beacons, as well as the received power, ensuring that the beacons are properly adjusted. To achieve this, the intensity and power of the beam at the receiver will be analyzed, along with verification of the beam's Gaussian distribution.

The ultimate goal is to use the system with the OGS to observe and verify beam distributions, divergences and received power in real time.

## 2.4 Link budget

In any optical communication system, a key step in evaluating its performance is the link budget calculation. This calculation determines the received optical power at a detector, given the known transmitted power, propagation conditions and receiver characteristics. The link budget accounts for all gains and losses along the propagation path, allowing one to determine whether the received signal has sufficient power to enable communication.

According to research, the total mean received power, taking into account all gains and attenuations that have a negative value, can be calculated as the sum of all link budget components in dB [17]:

$$p_{rx} = p_{tx} + a_{Tx} + g_{Tx} + a_{BW} + a_{FSL} + a_{Atm} + a_{Sci} + g_{Rx} + a_{Rx} \quad (6)$$

Where

$p_{Tx}$	average transmit optical source power	[dBm]
$a_{Tx}$	optical power loss inside the transmitter terminal	[dB]
$g_{Tx}$	transmitter antenna (telescope) gain	[dB]
$a_{BW}$	average loss by dynamic beam miss-pointing and beam wander	[dB]
$a_{FSL}$	free-space loss by link distance	[dB]
$a_{Atm}$	sum of atmospheric attenuation effects	[dB]
$a_{Sci}$	losses through atmospheric scintillation	[dB]
$g_{Rx}$	receiver antenna gain	[dB]
$a_{Rx}$	optical losses inside receiver terminal (attenuation and splitting)	[dB]
$p_{Rx}$	received power on detector	[dBm]

The method shown above could be used. However, for a short-range terrestrial test, many orbital dynamics and elevation effects are irrelevant, and the environment is controlled. In this work, the receiver power can be evaluated using a geometrical approach that incorporates both the physical beam spreading and the Gaussian intensity distribution.

This general approach is described in the following pages. Some simplifications have been made to adapt the full optical link budget to our test environment.

Firstly, instead of using separate attenuation losses for miss-pointing, beam wonder, free-space loss, atmospheric loss and scintillation loss as well as optical losses, most of the attenuation factors are ignored and the project only focuses on the attenuation caused by filters and lenses. This new attenuation factor is called X.

It is important to note that divergence losses are taken into consideration. As it is shown in Figure 15, since a divergent beam is used for the tests, the beam spreads and the power is distributed across the beam spot. If the receiver aperture area is smaller than the beam spot, some power is lost. On the other hand, if the beam spot is smaller than the receiver aperture area, all power is detected and there are no losses.

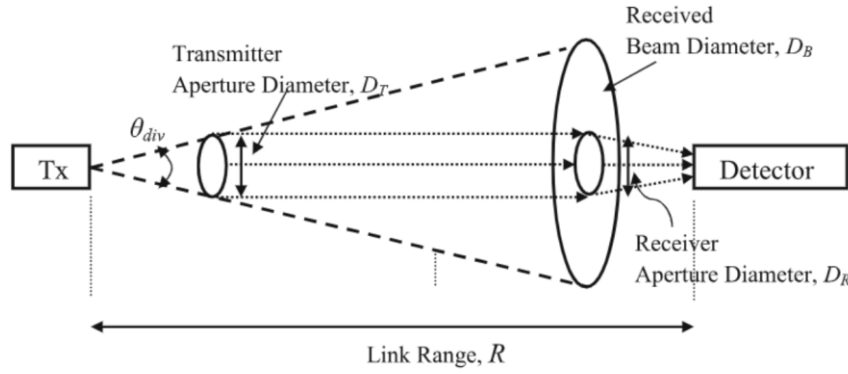


Figure 15: Losses due to beam divergence [28]

In the figure, a flat-top distribution is shown. This scenario can occur if the beam spot is much larger than the receiver aperture. In most cases of this project, the beam is not significantly larger than the receiver aperture. To calculate the received power accurately, the Gaussian distribution of the beam must be taken into consideration.

Finally, with the use of equation 3, the received power looks like so:

$$p_{rx} = (p_{tx} \cdot X) \left[ 1 - e^{-\frac{2r^2}{w_0^2(z)}} \right] \quad (7)$$

Where  $r$  is the detectors aperture radius,  $w_0^2(z)$  is the radius at which the intensity has decreased to  $1/e^2$  or 0.135 of its axial, or peak value, and the product  $(p_{tx} \cdot X)$  gives us the total power at the receiver after losses.

Using this approach, a link budget for our controlled environment is established, taking into consideration the beam characterization, receiver geometry and loss estimation. Although simplified compared to a full orbital link budget model, this methodology captures essential physics relevant on a short-range terrestrial link.

In this section, all the theoretical knowledge has been presented, along with an introduction to the current requirements and challenges in beacon alignment. These challenges have motivated this project and led to the development of a Test Target for supervising the beacons of optical ground stations.

### 3 Implementation and validation metrics

As mentioned in previous sections, the main objective of this work is to develop a new method to verify the alignment and adjustment of the beacons used in OGSs in FSO communications. Ideally, this adjustment is performed in real time, and the device and software developed are intended to visualize the beam's distribution, which is ideally Gaussian. For this verification, data and measurements of parameters such as beam divergence and received power at the receiver are required.

In this section, the decisions made prior to executing the tests are explained and justified. The design of the test target, its components, and the function of these components are described. The assembly of custom beacons which act as an OGS, is also clarified.

Furthermore, all the calculations and tests necessary for making component and parameter selection decisions are explained. Since the project focuses on a verification method, this section also presents the calculations used to obtain the required theoretical data for verification, such as the power at the receiver. This data is later used to compare the theoretical results with the measurements obtained through the Test Target.

#### 3.1 System design

The initial design of our project, referred to as the "Test Target", is described in this section. It is important to emphasize that the project has two primary objectives, which are achieved as follows: directional alignment is verified by measuring the intensity and power of the beam at the receiver and divergence adjustment by surveilling the distribution or shape of the beam as well as its divergence. The Test Target has been designed to fulfil both objectives simultaneously.

The location where the project was carried out is one of the fundamental factors that influenced other design decisions. From the beginning, two main components were established: the Test Target and a transmitter that acts as the OGS's beacons, instead of using the OGS located on the rooftop of the Institute of Communications and Navigation (IKN) at the DLR Oberpfaffenhofen site. The two components are 325 m apart, as shown in Figure 16 and the Test Target has a mirroring setup to the transmitter. The transmitter is located in the German Space Operation Center (GSOC) building, while the receiver, or Test Target, is in IKN.

Other parameters were also established in advance, such as wavelength, the different fixed divergences used, and the maximum power to ensure the tests remain eye safe. It is worth mentioning that the final device, the Test Target, is intended to be used with an OGS. As mentioned in section 2.1.2.1, OGSs use multiple beacons for redundancy and satellite tracking. In our case, the project simulates the alignment of two OGS beacons.

To summarize, Table 1 and 2 show all the pre-established parameters that were used in making decisions.



Figure 16: Link distance and locations at DLR Oberpfaffenhofen

Transmitter	
Description	Value
Altitude	580 m s.l.
Location	48.09, 11.28
Wavelength	1550 nm $\rightarrow$ 1562 nm
Number of transmitters	2
Divergence angle at FWHM*	924 $\mu$ rad, 545 $\mu$ rad, 329 $\mu$ rad, 164 $\mu$ rad
Theoretical output beam diameter ( $1/e^2$ )	0.84 mm, 1.68 mm, 2.54 mm, 5.24 mm
Maximum transmitter power	50 mW

Table 1: Transmitter base parameters

Receiver / Test Target	
Description	Value
Altitude	580 m s.l.
Location	48.08, 11.28
Wavelength	1550 nm $\rightarrow$ 1562 nm
Number of receivers	2

Table 2: Receiver base parameters

In this section, the different components that are part of the design are described. The design of the custom beacons, which simulate those used in OGSs, is briefly discussed, along with an overview of the setup to ensure clarity.

### 3.1.1 Beam power detection

This subsection focuses on beam power detection at the receiver. Power detection is used both as an alignment method and as a verification tool for the collimator's divergence, based on the precalculated link budget. The use of received power as an alignment method refers to the following. As discussed in section 2.2, the laser beam ideally has a Gaussian distribution. This means that the maximum intensity is located at the center of the beam, as illustrated in the example of a Gaussian distribution shown in Figure 17.

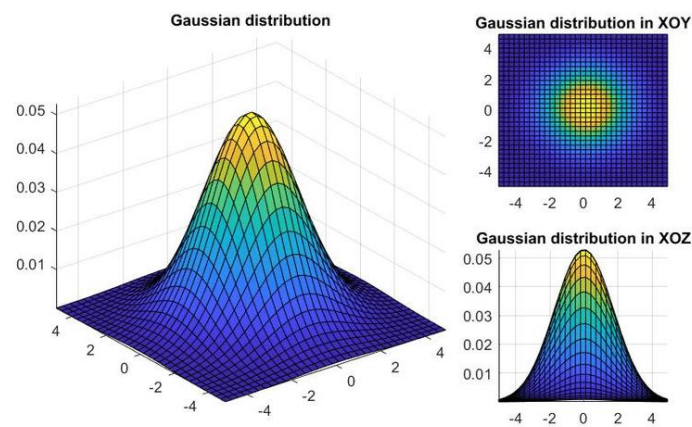


Figure 17: Gaussian distribution shown from different planes [14]

Figure 17 shows how the beam loses intensity as it moves away from the center. Based on this principle, the received value can be used as an alignment method by detecting the maximum power with a photodetector.

The following setup was designed to achieve this first objective:

- Transmitter acting as OGS beacons: A tripod holds a 1m long metal bar with two collimators mounted at each end. The collimators are fixed at 0.8 m from each other, which was made feasible by the bar length. Their positioning and alignment are ensured using sledges and kinematic mounts.

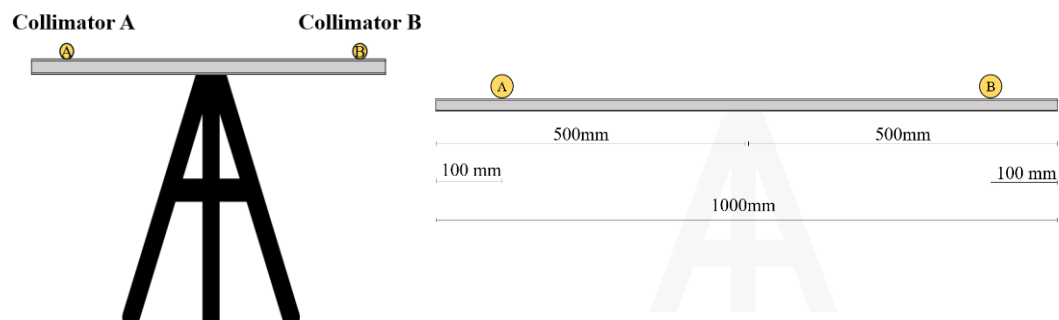


Figure 18: Transmitter design sketches

- **Test Target:** The receiver setup consists of two photodetectors positioned at the same distance from each other as the collimators on the transmitter side. For the project, this distance is 0.8 m and, as with the transmitter, a 1 m long metal bar was chosen on which the sledges and detectors were placed. Since the tests and measurements are carried out during daytime, the photodetector design includes additional optical elements. Specifically, filters and lenses are placed in front of each photodetector to filter out background light and increase the photodetector's field of view (FOV). The specifications are discussed in section 3.2.

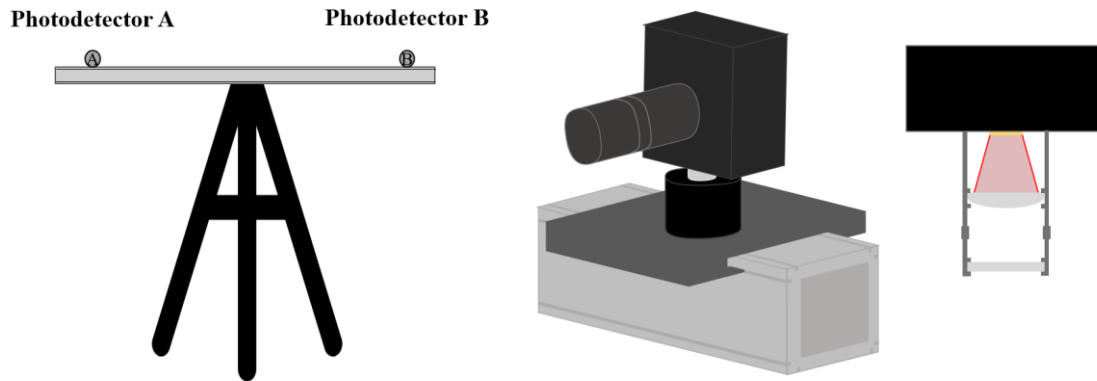


Figure 19: Test Target design sketches with sensor mount set up and lenses

Therefore, by equipping the photodetectors with the appropriate lens and filters, and collimators, it is possible to simulate a realistic scenario and fulfill the objective of aligning and adjusting the beacon's direction based on the detected power at the receiver. The power received is further validated by comparing it with the values predicted from the link budget. This comparison ensures that the transmitter divergences are within the expected bounds. In cases where discrepancies occur, the divergence corresponding to the measured power can be recalculated and compared, providing additional means of verification.

### 3.1.2 Back-reflecting foil & camera

To verify the beam distribution and divergence, a more visual approach also implemented. An initial option considered was to use the chosen photodetectors by moving them horizontally analyzing the measured values to verify the Gaussian distribution. However, this approach was disregarded, as manually shifting the photodetectors is inefficient, time consuming and introduces the risk of defocusing optical components such as lenses.

Instead, a retroreflective material was placed around the photodetectors, combined with a camera to capture the reflection of the beams. Thus, on the transmitter side, a camera sensitive to the laser wavelength is installed, and on the Test Target side retroreflective foils were placed. This configuration allows the beam profile to be visualized remotely through the camera. Like the photodetectors, the camera requires a filter for the background light and a lens to ensure proper focusing. Detailed specifications of the lenses and filters are provided in sections 3.2.2 and 3.2.3.

The final setup can be seen in Figure 20 on the next page.

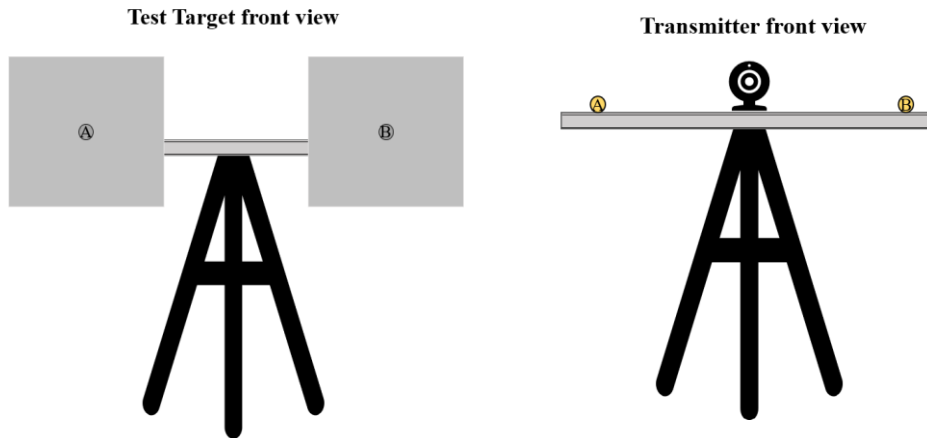


Figure 20: Final sketches from both the Test Target and transmitter side

The decision to surround the photodetectors with retroreflective material was made because the objective is to align the collimators with the photodetectors and, therefore, it is sure that the beam will be within the surrounding area.

That said, with adequate exposure and proper alignment, the camera can capture the beam profile, allowing the analysis of both its distribution and divergence. This method not only fulfills the objective of verifying the beam distribution and divergence but also accelerates the alignment process. By providing a visual reference of the test target, it enables a more intuitive and quicker coarse alignment. The retroreflective foil is thus used initially to roughly locate the beam, after which a fine alignment can be performed more precisely using the received power measurements from the photodetectors.

### 3.1.3 Beacon design

As previously mentioned, the project requires simulating the beacons used in optical ground stations (OGS). This subsection briefly outlines the elements selected for this simulation. It is important to emphasize that, although an optical link is established, no data is transmitted through it.

The custom-built beacons consist of the following components:

- Collimators: As discussed in the theory section, the outgoing beam must either be diverging or collimated. In this project, collimators with divergences ranging from 0.164 mrad to 1 mrad are employed. Collimators with fixed divergence and adjustable focus collimators are alternated during the tests. The collimators are discussed in more detail in section 3.2.1.
- Laser diode: A laser diode is required to generate the beam that passes through the collimators with sufficient power to reach the project's maximum operating level of 50 mW. The selected source is the FPL1009S from Thorlabs, specified as a laser diode centered in 1550 nm. However, the specifications of the particular lasers states that the laser wavelength is 1562 nm. This change in parameters is considered in the calculations made in the following sections.

FPL1009S				
	Symbol	Min	Typical	Max
<b>Electrical</b>				
Operating Current	$I_{OP}$	-	400 mA	500 mA
Center Wavelength	$\lambda_C$	1530 nm	1550 nm	1570 nm
Spectral Bandwidth (RMS)	$\Delta\lambda$	-	10 nm	20 nm
Output Power over C-Band	$P_{OUT}$	80 mW	100 mW	-
Threshold Current	$I_{TH}$	-	35 mA	55 mA
Slope Efficiency	$\Delta P / \Delta I$	0.2 W/A	0.3 W/A	-
Forward Voltage	$V_F$	-	1.4 V	1.8 V
<b>TEC Operation (Typical / Max @ <math>T_{CASE} = 25^\circ\text{C} / 70^\circ\text{C}</math>)</b>				
TEC Current	$I_{TEC}$	-	0.18 A	1.5 A
TEC Voltage	$V_{TEC}$	-	0.5 V	3.5 V
Thermistor Resistance	$R_{TH}$	-	10 k $\Omega$	-

Table 3: FPL1009S laser diode's specifications. Typically centered in 1550 nm (in our case 1562 nm). Typical power of 100 mW [29]

- Compact laser diode controller: Controllers are required to regulate the laser's output power. These devices also offer the possibility of limiting the laser's maximum output power, which is essential to ensure eye safety guidelines. The CLD101x Compact Laser Diode Controller from Thorlabs was chosen.
- Fibers and connectors: The laser diodes are not directly connected to the collimators, as the system is very sensitive. For this reason, intermediate fiber cables and connectors are used, considering the FC/APC or FC/PC connection type of each element. Precision kinematic mirror mounts were also purchased to adjust the setup with precision.

With these components, the transmitter simulating the OGS beacons was assembled. A schematic of the beacon setup is shown in the following figure. Both collimators are identical and operate under the same conditions to ensure consistent performance.

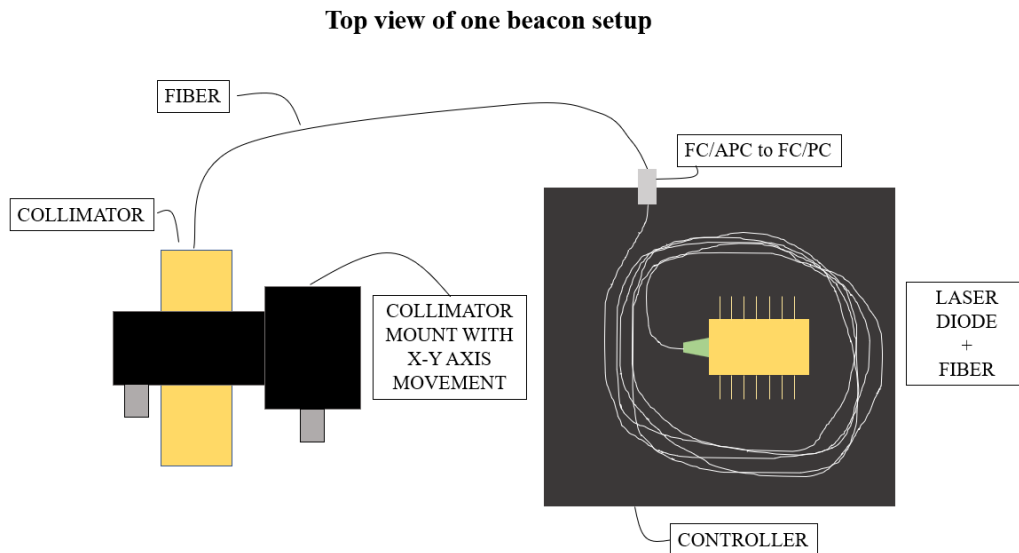


Figure 21: Custom beacon setup with components

## 3.2 Components

Now that the overall design of the project has been explained and illustrated, this section specifies the components used in the setup. The specific technologies and parameters that make the components suitable for the project are discussed, along with justifying the selection.

The transmitter side is described first, followed by the receiver side.

### 3.2.1 Camera

One of the most important components for this project is the camera. The chosen camera needed sufficient resolution to observe the beam at the required distance. Additionally, since a wavelength of approximately 1550 nm (1562 nm to be precise) was selected for the project, the camera must be capable of capturing clear images at this wavelength.

The camera selected for the project is the Goldeye G-130 TEC1. This is an Indium Gallium Arsenide (InGaAs) camera capable of capturing 94 frames per second at a resolution of 1.3 MP. The camera contains a Sony IMX990 sensor with a wavelength range of 400 nm to 1700 nm, making it fully suitable for the 1562 nm laser used in the project. Its pixel size of  $5\ \mu\text{m} \times 5\ \mu\text{m}$  is useful to more easily distinguish the Gaussian distribution of a very small beam [30].

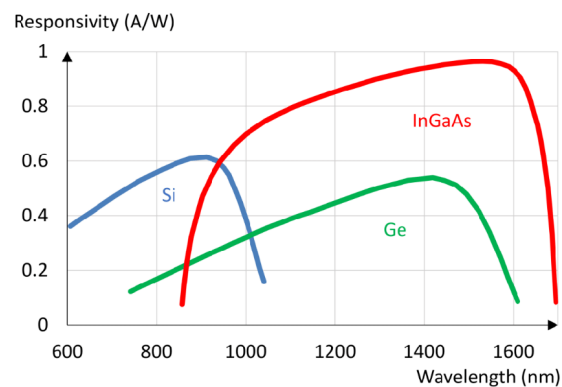


Figure 23: Typical responsivity for silicon, InGaAs, and germanium [31]



Specifications	
Interface	IEEE 802.3 1000BASE-T, IEEE 802.3af (PoE)
Resolution	1280 (H) × 1024 (V)
Spectral range	400 nm to 1700 nm
Sensor	Sony IMX990   InGaAs
Sensor type	InGaAs
Shutter mode	GS (Global shutter)
Sensor size	Type 1/2 VSWIR
Pixel size	$5\ \mu\text{m} \times 5\ \mu\text{m}$
Lens mount (default)	C-Mount
Max. frame rate at full resolution	94 fps
ADC	12 Bit

Figure 22: Goldeye G-130 TEC1 camera and its specifications [30]

When analyzing the quantum efficiency shown in Figure 24, the camera has a slight drop from 1500 to 1600 nm, with a quantum efficiency of approximately 68%.

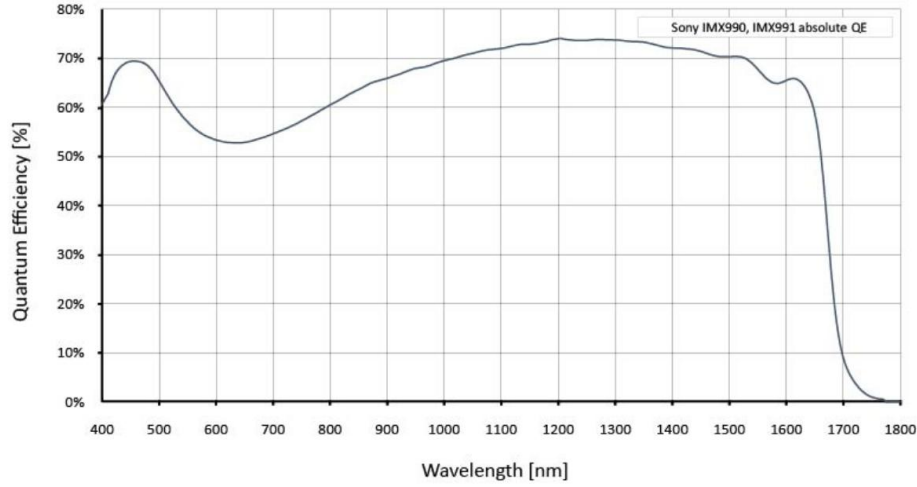


Figure 24: Goldeye G-130 TEC1 camera's quantum efficiency [30]

Although this camera's quantum efficiency is slightly lower compared to other sensors, since the pixel value is not used to calculate the received power, more importance is given to pixel size and resolution. The  $5\ \mu\text{m} \times 5\ \mu\text{m}$  pixel size enables an image resolution of  $1280 \times 1024$ , which is significantly higher than that of an alternative model such as the Goldeye G-008 TEC1 ( $320 \times 256$ ).

Another advantage of the chosen camera is its easy software integration with Vimba / Vimba X and its compatibility with the most popular third-party image-processing libraries. For this project, the vmbpy library is used to develop a custom interface, which is explained in section 4.2.

In summary, this camera has the necessary resolution to visualize the beams, accessible tools to save and process the images, and the right sensor to work with the lasers at a 1562nm wavelength.

### 3.2.1.1 Lens

To understand the choices made when selecting lenses for each device, it is important to review some properties of lenses and their focal length. The focal length ( $fl$ ) of a lens is directly related to the magnification ( $m$ ) and its field of view (FOV). As the focal length increases, magnification increases while the FOV decreases (equations 8 and 9 where  $H$  is the sensor size and  $WD$  is the working distance) [32].

$$m = \frac{H}{FOV} \quad (8)$$

$$fl = \frac{(H \cdot WD)}{FOV} \quad (9)$$

Working at a considerable distance and aiming to analyze the distribution of a small beam, a lens with a focal length of 200 mm was selected to achieve the necessary magnification, with less emphasis on the FOV.

The specific lens chosen is the AC254-200-C from Thorlabs. This lens is an achromatic doublet composed of two types of cemented glass to correct chromatic aberration. Chromatic aberration is an optical defect that occurs when the lens fails to focus all wavelengths at the same point. This is because the refractive index of glass varies with each wavelength [33]. Achromatic doublets are specifically designed to correct this. Additionally, this lens features an anti-reflective coating for 1050-1700 nm, making it ideal for the wavelength used in this project.

### 3.2.1.2 Filter

As discussed in the design section, the tests are conducted during the day, so background light interference must be minimized. To achieve this, a filter centered around 1550 with the largest full width at half maximum (FWHM) bandwidth possible was selected. With the FWHM BW of 30 nm, which includes the 1562 nm wavelength used for the tests, the FBH1550-30 filter from Thorlabs was chosen [34].

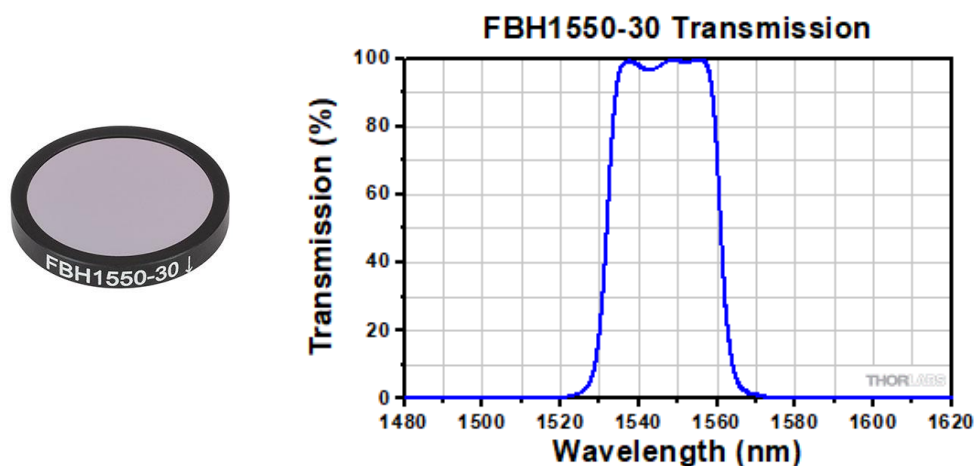


Figure 25: FBH1550-30 filter (left) and its transmission vs wavelength graph [34]

This filter's transmissivity graph can be seen in Figure 25. It can be observed that the transmissivity at 1562 nm wavelength is not 100%, which affects the power reaching the camera. This loss has been considered in the link budget calculation and verified experimentally (section 3.3.3).

Finally, Figure 26 illustrates the design of the camera tube setup, including filters and lens. Although all elements should ideally be placed at a precise distance, it is recommended to focus the camera lens before use.

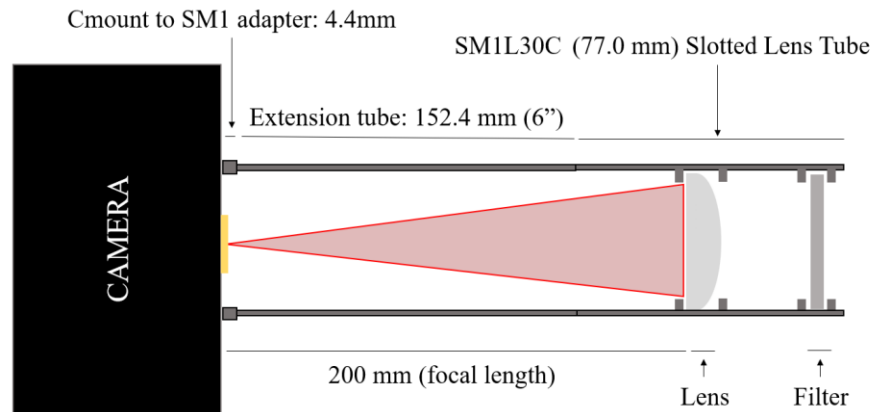


Figure 26: Camera tube setup

### 3.2.1 Collimators

The collimators used in the project are another important component. In the end, one of the aims is to verify the adjustment and properties of the beam and the collimators' divergences take a central role. For this purpose, four fixed divergence collimators were selected for the verification process, along with a fifth adjustable focus collimator to test the setup and perform in real time adjustments.

The initial goal is to validate the setup using the four fixed divergence collimators. Once the setup is tested, the adjustable focus collimator can be adjusted for a desired divergence. The fixed divergence collimators chosen have FWHM divergences of 924  $\mu\text{rad}$ , 545  $\mu\text{rad}$ , 329  $\mu\text{rad}$  and 164  $\mu\text{rad}$ .

The adjustable collimator used is the adjustable focus reflective collimator with a protected silver coating from Thorlabs. This off-axis parabolic (OAP) mirror collimator uses a mirror to adjust the beam's focus. When the collimator is at the position marked by  $\infty$  on the focusing distance scale, the collimator collimates the output beam. The beam divergence can be modified by moving the fiber within the focusing distance range -2.2 m to 0.15 m, which shifts the beam from diverging behind the mirror to focusing in front of it [35]. The defocusing and fiber movement direction are illustrated with an arrow in Figure 27.

Table 4 bellow summarizes the references and divergences of the collimators used in the project.

Reference	$1/e^2$ divergence (mrad)	FWHM divergence (mrad)
F110FC-1550	1.57 mrad	0.925 mrad
F220FC-1550	0.925 mrad	0.545 mrad
F280FC-C	0.558 mrad	0.329 mrad
F810FC-1550	0.279 mrad	0.164 mrad
RCF-15A-P01 (collimated)	0.698 mrad	0.411 mrad

Table 4: Reference,  $1/e^2$  divergence and FWHM divergence of fixed collimators

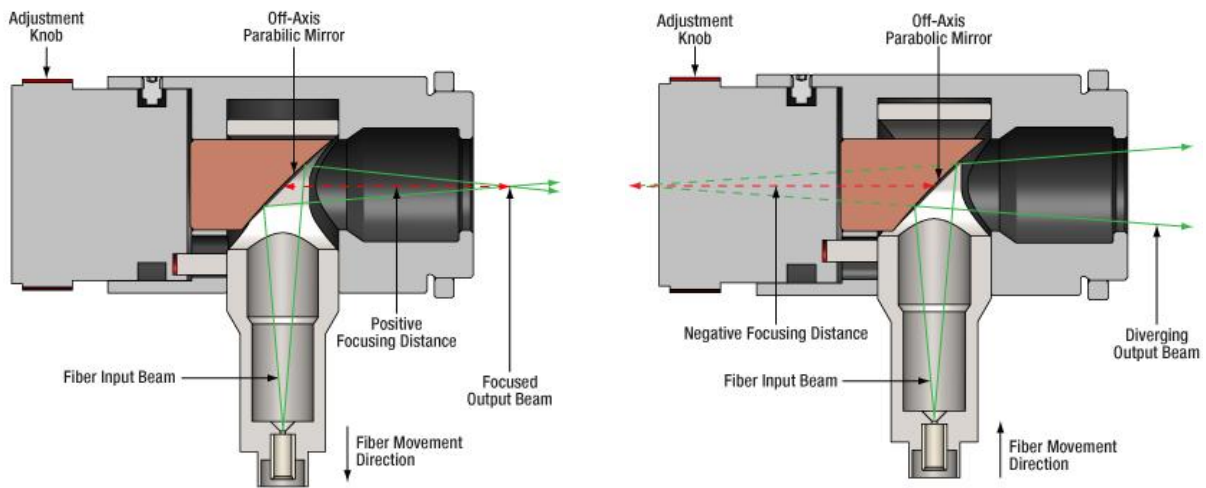


Figure 27: Converging beam schema with fiber getting away from the focus point (left). Diverging beam with fiber getting past the focus point (right) [35]

### 3.2.2 Indium Gallium Arsenide switchable gain photodetector

As mentioned in section 3.2.1, an InGaAs photodetector is the most suitable choice for the wavelength used in this project. The PDA20CS2 InGaAs switchable gain photodetector was selected. Since different collimators produce varying power levels, depending on their divergence, a switchable gain photodetector allows adjustment of the sensitivity accordingly. However, to reduce variables during testing, only the 30 dB gain setting is used in this project.

Several operational decisions were made regarding the photodetector. The photodetector has two usable modes: with a 50  $\Omega$  load and without one. For this project, the Hi-Z setting (without the 50  $\Omega$  load) is used, and the calculations are done accordingly.

30 dB Setting	
Gain (Hi-Z)	$4.75 \times 10^4$ V/A $\pm 2\%$
Gain (50 $\Omega$ )	$2.38 \times 10^4$ V/A $\pm 2\%$
Bandwidth <sup>3</sup>	260 kHz
Noise (RMS)	234 $\mu$ V
NEP	$2.19 \times 10^{-12}$ W/ $\sqrt{\text{Hz}}$
Offset	$\pm 8$ mV (Typ.) $\pm 12$ mV (Max)

Table 5: 30 dB gain settings in the InGaAs photodetector [36]

Additionally, the responsivity of the photodetector was also considered. The graph shown in Figure 28 indicates that the responsivity at 1562 nm is approximately 1.02 A/W. This value is incorporated into the link budget calculations.

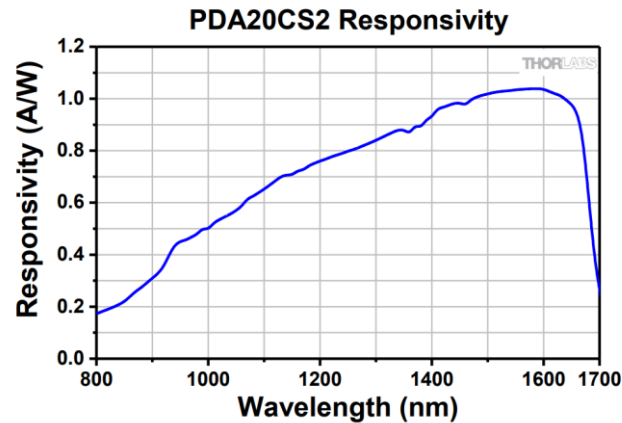


Figure 28: PDA20CS2 responsivity at each wavelength graph [36]

Finally, the electronic offset associated with each gain setting was analyzed to include it in the link budget. To determinate this, each photodetector was sampled at 5000 samples per second for 15 seconds. The mean value of the collected data was then calculated for each gain setting to estimate the electrical offset. The results are presented on the table below.

dB Gain	Electronic offset	
	LEFT DETECTOR (V)	RIGHT DETECTOR (V)
0	0.0055	0.0078
10	0.0118	0.0143
20	0.0118	0.0143
30	0.0119	0.0143
40	0.0121	0.0143
50	0.0124	0.0142
60	0.0118	0.0115
70	0.0142	0.0094

Table 6: Electronic offset for both photodetectors

### 3.2.2.1 Lens

As discussed in section 3.2.1.1, there is a relationship between focal length, magnification, and FOV. While the camera required considerable magnification, the photodetectors prioritize capturing the largest possible FOV to maximize received power. This is achieved by selecting a lens with a short focal length.

For the same reasons outlined in section 3.2.1.1, an achromatic lens was selected to minimize chromatic aberration. The lens chosen for the photodetectors is the Thorlabs AC254-030-C which has a focal length of 30 mm, the shortest focal length offered by Thorlabs in achromatic lenses. It also has an anti-reflective coating between 1050 and 1700 nm.

The filter used is the same as the camera: the FBH1550-30 filter from Thorlabs.

The setup of the tube is shown in the figure below. As with the camera setup, it is advisable to focus the lenses before use, as there is a slight focal shift in each lens for each wavelength.

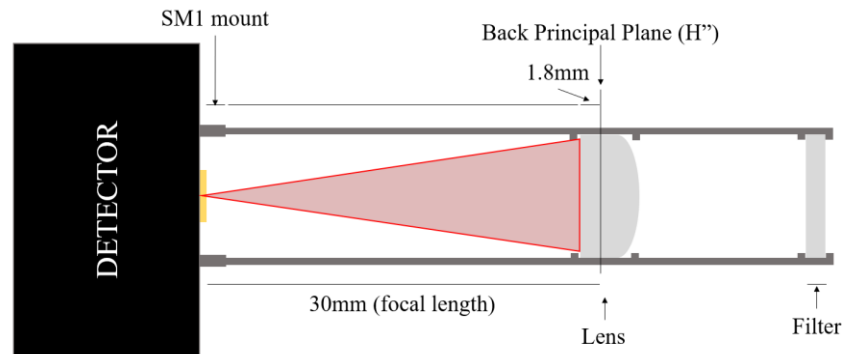


Figure 29: Photodetector tube setup

### 3.2.3 Retroreflective foil

The last crucial component for this project is the retroreflective foil. Retroreflective materials reflect incident light back towards the source. They can be constructed either as a 90° corner cube configuration or a high index-of-refraction transparent spheres with a reflective backing [37].

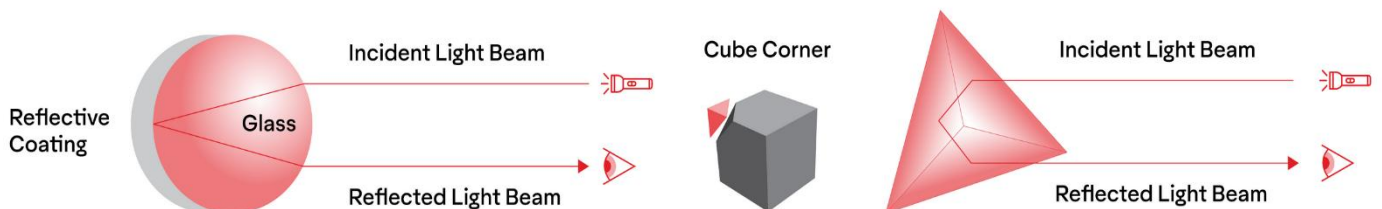


Figure 30: Retroreflective material options. Sphere with reflective coating on the back (Left) and corner cube (Right) [37]

Two angles are commonly used to describe the behavior of retroreflectors: the observation angle,  $\alpha$  and the entrance angle,  $\beta$ . The observation angle is defined as the angle between the illumination direction and the viewing direction while the entrance angle is the angle between the illumination axis and the normal to the retroreflector surface. Both are shown in Figure 31.

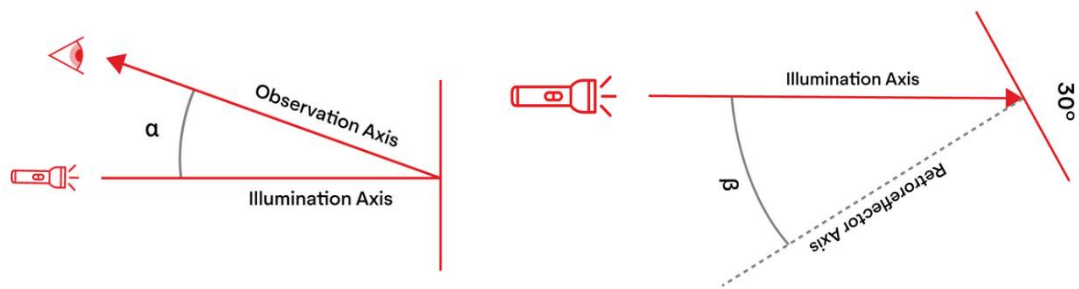


Figure 31: Observation angle  $\alpha$  (Left) and entrance angle  $\beta$  (Right) [37]

The retroreflecting properties of the material are highly important to clearly visualize the beam distribution. A variety of retroreflective foils were selected and tested, as most retroreflective materials are characterized for visible light but not for the 1562 nm wavelength used in this project. To evaluate them, the 1562 nm laser previously described was used. The camera and laser source were aligned as parallel and close as possible, and the retroreflective foil was positioned with an entrance angle close to  $0^\circ$  and  $7^\circ$  to see the effect of the entrance angle.

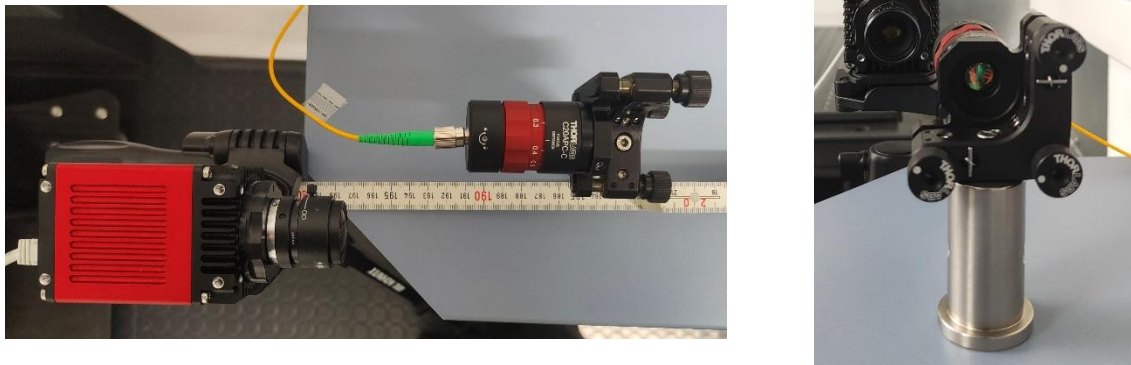


Figure 32: Top (Left) and front (Right) view of the camera and laser set up for the retroreflective foil test

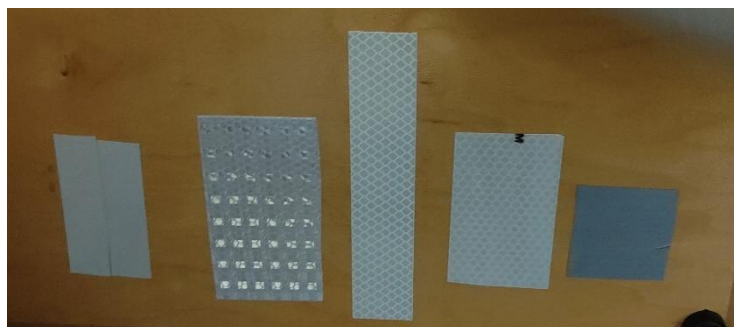


Figure 33: All the retroreflective foils to be tested on a box that was horizontally moved for the test

The test was made with a 500  $\mu$ s exposure time and a 4 m distance for the camera and 3.85 m for the laser source. The results can be seen on the table below.

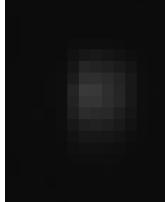
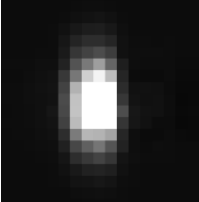
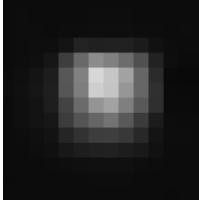

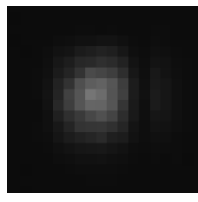
ENTRANCE ANGLE OF 0°					
Type	Silver 3M 610C	Diamond grade 3M	468 MP Zuschneidbar	Grade 983	Polyvinyl Chloride (PVC)
Maximum pixel value (255)	57	255	215	56	117
Mean value in 12x12 pixels (1)	0.072	0.24	0.156	0.079	0.127
Image					

Table 7: Retroreflective material test with the entrance angle of 0°

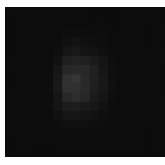

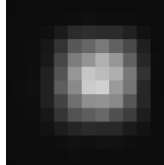

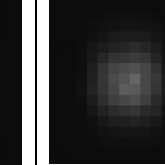
ENTRANCE ANGLE OF 7°					
Type	Silver 3M 610C	Diamond grade 3M	468 MP Zuschneidbar	Grade 983	Polyvinyl Chloride (PVC)
Maximum pixel value (255)	54	255	209	42	101
Mean value in 12x12 pixels (1)	0.071	0.193	0.17	0.072	0.144
Image					

Table 8: Retroreflective material test with the entrance angle of 7°

It was observed that the Diamond grade 3M retroreflective foil outperformed the others in both test conditions, with and without an entrance angle. This sheeting meets all current performance requirements of ASTM D4956 for Type IX and Type XI retroreflective sheeting [38]. Its superior performance can be seen in the maximum pixel value and overall mean of the 12 x 12 pixel area.

With this, all components used in the project, along with their characteristics and selection justifications, have been described.

### 3.3 Test conditions and validation parameters

This section describes the various tests carried out throughout the project to determine different characteristics, measurements, and theoretical values of parameters such as power and potential attenuations. It also presents the calculated link budgets and provides a summary of the final setup.

#### 3.3.1 Controller output power test

As explained in the design section, the project employs two lasers and controllers to simulate the OGS beacons. Although two supposedly identical lasers were purchased, this subsection discusses the measurements taken for each laser and any observed differences.

The controllers operate in such a way that the input is a specific current that subsequently generates output power. To perform the tests, each laser was connected to a controller and a specific fiber, ensuring that the measurements closely resembled the actual test environment. After testing, the fibers and the lasers were left connected; only the collimators, which were properly marked, were changed.

Using several power meters, measurements of the relationship between input current and output power were collected on two separate occasions. The mean of both measurement sets was then calculated and used in the tests. Although only 10 mW and 1 mW output power were used, the behavior of the lasers at different power levels was evaluated. The results are presented in the tables and figures below.

Optical power wanted (mW)	Electrical input current (mA)					
	Power meter up to 1 W		Power meter up to 40 mW		Mean Current for same power output	
	Controller A	Controller B	Controller A	Controller B	Controller A	Controller B
0.2	-	-	33	31.2	33	31.2
0.5	-	-	34.1	32.2	34.1	32.2
0.6	-	-	34.4	32.6	34.4	32.6
0.8	38	37	35.2	33.4	36.6	35.2
1	39	37.8	36.1	34.2	37.55	36
1.5	41	39.6	38.3	36.3	39.65	37.95
2.5	44	43.6	42.7	40.3	43.35	41.95
3	46	45.3	44.4	42.4	45.2	43.85
5	52.6	52	51.5	49.2	52.05	50.6
7	59.6	58.8	58.5	56	59.05	57.4
10	70	68.8	69	66.3	69.5	67.55
15	87.2	85.2	86.6	83.4	86.9	84.3
20	104.6	101.2	104.2	100.4	104.4	100.8
25	121.6	118	122.2	117.6	121.9	117.8
30	138.3	134.2	139.6	134.8	138.95	134.5
40	174.3	168.2	-	-	174.3	168.2
50	210	204	-	-	210	204

Table 9: Measurements for input current to get a set output power

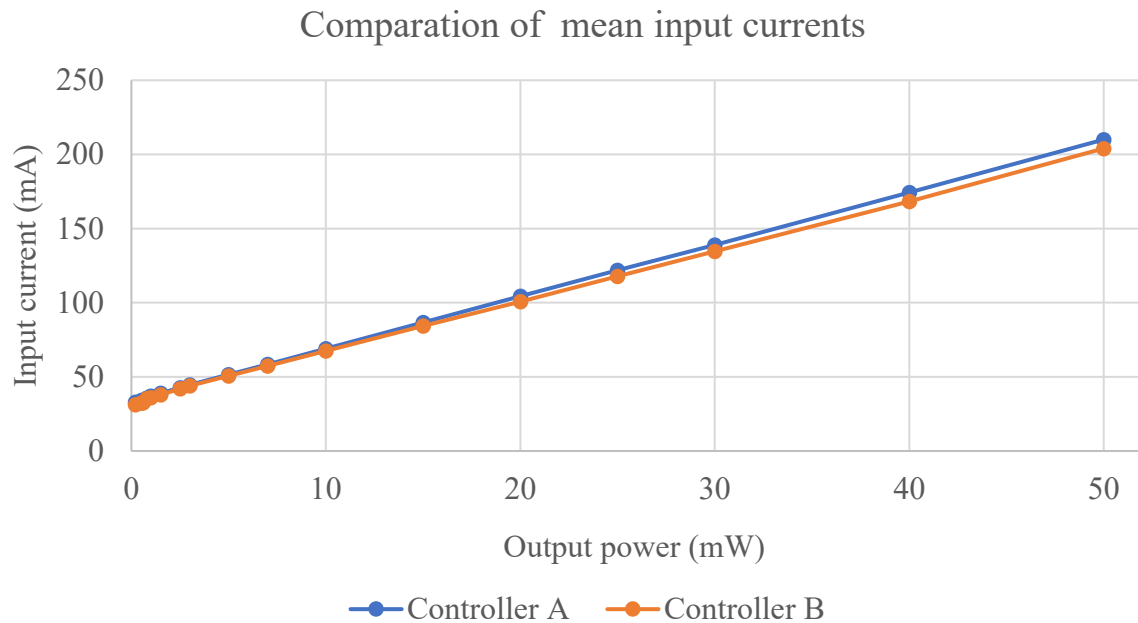


Figure 34: Graph for visual representation of input current to output power conversion from the controllers

As shown in the graph, one of the lasers requires a higher input current to achieve the same output power. If only one of the lasers was tested, the current values applied to the other laser would not have been adequate.

That said, environment conditions like heat can deviate the performance of the laser even though the measurements were done various times. This must be considered when it comes to analyzing the results.

### 3.3.2 Filter Attenuation Test

As mentioned in previous sections, the selected filters (FBH1550-30 from Thorlabs) centered at 1550 nm with a 30 nm bandwidth, are designed to transmit the 1562 nm laser. From the transmission graph shown in Figure 25, the transmission index value can be initially estimated to be around 40%. This section describes the tests performed to determine the transmission index more accurately.

The test procedure was as follows: the photodetectors are illuminated with the selected lasers at a known output power using the appropriate focusing lens. The beam was recorded by the photodetector for 15 seconds at a sample rate of 5000 samples per second. The filter was then placed between the focusing lens and the fiber, and another 15 second measurement was taken. The process was done only with the 30dB gain stage selected, which is what is used in this project. Finally, the ratio between the values is calculated to determine the attenuation introduced by the filter. The setup can be seen in Figure 35.

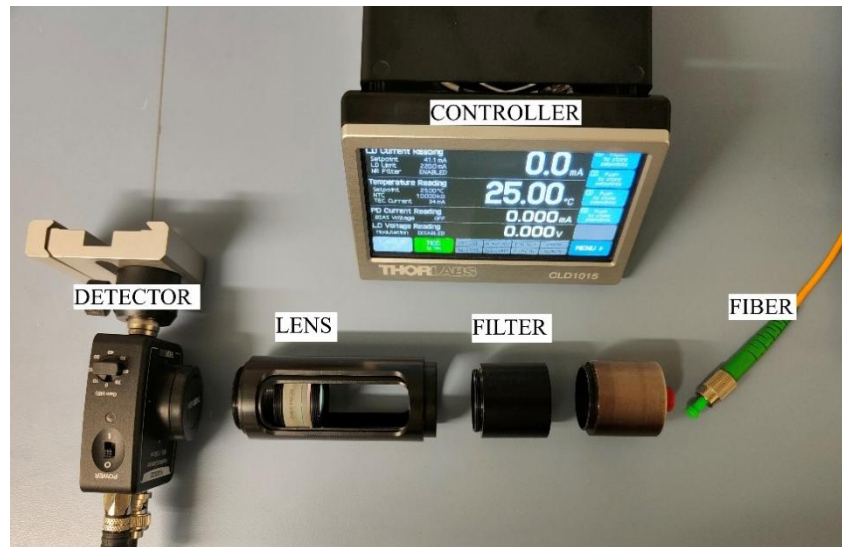


Figure 35: Filter test setup

The measurements can be seen on the table below.

Setup	Gain (dB)	Output power (mW)	Voltage detected on detector directly with lens (V)	Voltage detected in detector with filter and lens (V)	Transmission coefficient
Left detector with controller A	30	0.5	8.0987	7.8688	1.029
Right detector with controller B	30	0.5	9.2842	9.6202	0.965

Table 10: Results for the transmission coefficient calculations for FBH1550-30 filter with 30dB gain

By the results, even though in the data sheet a transmissivity of approximately 40% was assumed, it can be clearly seen that it is not the case. The measurements indicate a transmissivity of approximately 0.98. However, for the purpose of calculations and to account for potential variations, a value of 0.9 will be used, representing a worst-case scenario.

### 3.3.3 Link Budget

In this section, the theoretically received power is calculated and analyzed using the link budget. Two distinct links are considered: the link from the beacons to the photodetectors, and the link that allows the camera to capture the illuminated pixels.

A system must be designed so that the transmitted power is sufficient for the camera to detect the beam reflection without saturating the photodetector. Since the retroreflective foil test demonstrated that the camera has adequate sensitivity to observe the beam, the limiting factor in this setup is the link budget between the beacon and the photodetectors.

All link budgets are calculated with the distance of 325 m and for the four fixed divergence collimators at 1562 nm wavelength.

#### 3.3.3.1 Beacon to photodetector Link Budget

To begin with, the limitation factor for the photodetector's aperture is the filter. While the photodetector tube and the lens have a diameter of approximately 25 mm, the filter has a clear aperture of 21.1 mm.

For the link budget calculations, the effective aperture radius is taken as  $r = \frac{21.1}{2} \text{ mm} = 10.5 \text{ mm}$ .

The table below presents the calculations of the received power at the photodetectors, based on the formulas described in the theoretical section.

Parameter	Unit	Value for each collimator				Formula
Full divergence at FWHM	mrad	0.925	0.545	0.329	0.164	-
Power at source ( $P_{tx}$ )	W	0.01	0.01	0.001	0.001	-
Distance	m	325	325	325	325	-
Filter transmissivity	1	0.9	0.9	0.9	0.9	-
Lens transmissivity	1	0.95	0.95	0.95	0.95	-
Receiver aperture ( $r$ )	m	0.0105	0.0105	0.0105	0.0105	-

Power after losses ( $P_o$ )	W	8.55E-03	8.55E-03	8.55E-04	8.55E-04	$P_{tx} \cdot t_{filter} \cdot t_{lens}$
FWHM diameter at target ( $\phi_{FWHM}$ )	m	0.30	0.18	0.11	0.05	$2 \cdot dist \cdot \tan\left(\frac{div_{FWHM}}{2}\right)$
Gauss-1/e <sup>2</sup> -Radius after Distance( $\phi_{e^{-2}}$ )	m	0.26	0.15	0.09	0.05	$\phi_{FWHM} / \sqrt{2 \cdot \ln(2)}$
Axial intensity ( $I_o$ )	W/m <sup>2</sup>	8.35E-02	2.41E-01	6.60E-02	2.66E-01	$\frac{2P_o}{\pi w_o^2(z)}$
Received power ( $P_{rx}$ ) (Gaussian)	W	2.91E-05	8.37E-05	2.28E-05	8.80E-05	$P_o \left[ 1 - e^{-\frac{2r^2}{w_o^2(z)}} \right]$
Received power ( $P_{rx}$ ) (Flat top)	W	2.92E-05	8.41E-05	2.31E-05	9.29E-05	$I_o \cdot \pi r^2$

Table 11: One-way link budget

As shown in Table 11, the received power was calculated using two different approaches to determine whether the beam size is large enough to neglect the Gaussian distribution. For larger divergences, the difference between the two calculations is minimal. However, as divergence decreases, a slightly greater change appears, so the calculations that account for the Gaussian distribution were selected.

It should also be noted that the photodetector gain was set to 30 dB. This ensures that, when combining the powers of 1 mW and 10 mW with the collimators of larger divergence (0.925 mrad and 0.545 mrad) and small divergence (0.329 mrad and 0.164 mrad) respectively, the photodetector does not become saturated.

The photodetector produces an output voltage in the range of 0 and 10 V. To convert the received power to voltage, the data from Table 5 and Figure 28 were used, along with a responsivity 1.02 A/W and a gain of 47.5kV/A.

General Data		
Parameter	Unit	Value
Peak Response (1590 nm)	A/W	1.04
Peak Response (1562 nm)	A/W	1.02
Gain (30 dB)	V/A	4.75E+04

Table 12: General data for power to voltage conversion [36]

The power to voltage conversion can be seen in the table below.

Parameter	Unit	Value for each collimator			
Full divergence at FWHM	mrad	0.925	0.545	0.329	0.164
Power at source ( $P_{tx}$ )	W	0.01	0.01	0.001	0.001
Received power ( $P_{rx}$ ) (Gaussian)	W	2.91E-05	8.37E-05	2.28E-05	8.80E-05

PIN-current from optical power	A	2.97E-05	8.54E-05	2.32E-05	8.98E-05
Voltage from detector	V	1.4121	4.0547	1.1032	4.2640

Table 13: Power to voltage conversion for photodetector

### 3.3.3.2 Beacon to camera

Next, the link budget between the beacon, the retroreflective foil, and the camera is considered. The first step is to calculate the minimum power required for the camera to detect a few illuminated pixels. Since specific data for the exact camera used in this project was not available, an approximation is made based on measurements performed by a colleague using a camera with the same InGaAs sensor but larger pixels (30 x 30  $\mu\text{m}$  pixels instead of 5 x 5  $\mu\text{m}$ ).

For the setup, it is essential that the camera can register the beam at the Test Target. Therefore, the beam must transmit a minimum power at the camera's distance. Using 100 milliseconds exposure setting along with the retroreflective foil and previous measurements from our colleague, the minimum power required for at least one pixel to reach a brightness value of 100 is determined.

Our colleague's measurements are taken with a 20 ms exposure. Considering a 100 ms exposure, the power needed is 5 times less than what our colleague's formula considers.

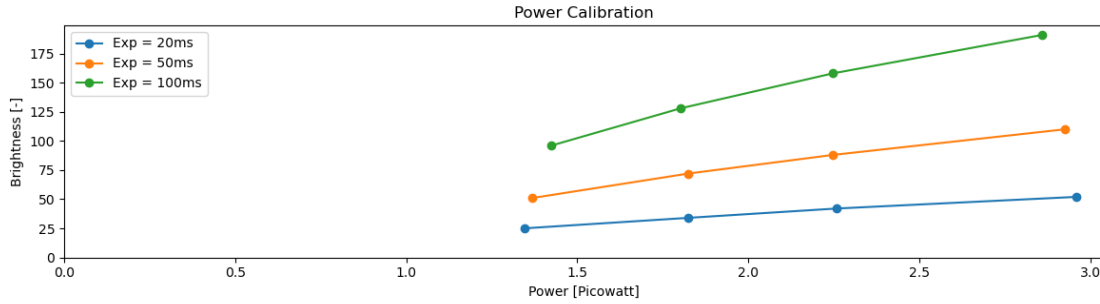


Figure 36: Colleague's measurements in order to correlate the brightness value of a pixel with the incident power depending on the exposure

Our colleague's calculations say the following for a 20 ms exposure:

$$P_{\text{pixel}} \text{ (nW)} = 0.0000775413 \cdot \text{pixel brightness value} \quad (10)$$

For only one pixel to be illuminated with 100 ms exposure, the power at the camera should be:

$$\frac{1}{5} \cdot 0.0000775413 \cdot 100 = 0.03877 \text{ nW}$$

Only one illuminated pixel is not enough. The power for a 20 x 20 pixel area that all have 100 brightness value.

$$\frac{1}{5} \cdot 0.0000775413 \cdot (20 \cdot 20 \cdot 100) = 0.6203 \text{ nW} = 620.3 \text{ pW}$$

In order to capture an image of the reflected beam, a minimum power of 620.6 pW is required.

With this value established, the link budget can be calculated. The link budget consists of two parts: the first part with a divergence according to the collimator in use in which the link goes from the beacon to the Test Target. At the Test Target, the power received by the photodetector is absorbed. The second part of the link goes from the retroreflective foil to the camera. For this path, the beam divergence is not precisely known, as the foil specifications only provide information on the visible light spectrum. Therefore, a divergence of approximately 1° FWHM has been assumed.

Using the specifications above, the link budget was calculated, and the results are presented in Table 14.

Parameter	Unit	Value				Formula
Full divergence at FWHM	mrad	0.925	0.545	0.329	0.164	-
Power at source ( $P_{tx}$ )	W	0.01	0.01	0.001	0.001	-
Distance	m	325	325	325	325	-
First link attenuation ( $\alpha$ )	1	0.9	0.9	0.9	0.9	-

Power after losses	W	9.00E-03	9.00E-03	9.00E-04	9.00E-04	$P_{tx} \cdot \alpha$
FWHM diameter at target	m	0.30	0.18	0.11	0.05	$2 \cdot dist \cdot \tan\left(\frac{div_{FWHM}}{2}\right)$
Gauss-1/e <sup>2</sup> -Radius after Distance	m	0.26	0.15	0.09	0.05	$\phi_{FWHM} / \sqrt{2 \cdot \ln(2)}$
Axial intensity	W/m <sup>2</sup>	8.79E-02	2.53E-01	6.95E-02	2.80E-01	$\frac{2P_o}{\pi w_o^2(z)}$
Received power ( $P_{rx1}$ ) (Gaussian)	W	4.44E-05	1.27E-04	3.45E-05	1.31E-04	$P_o \left[ 1 - e^{-\frac{2r^2}{w_o^2(z)}} \right]$
Power on foil ( $P_{foil}$ )	W	8.96E-03	8.87E-03	8.65E-04	7.69E-04	$P_o - P_{rx1}$
Reflected power by the foil (50%) ( $P_{refl}$ )	1	4.48E-03	4.44E-03	4.33E-04	3.84E-04	$P_{foil} \cdot 0.5$

Full divergence at FWHM	mrad	0.017	0.017	0.017	0.017	-
Filter transmissivity	1	0.9	0.9	0.9	0.9	-
Lens transmissivity	1	0.95	0.95	0.95	0.95	-
Receiver aperture ( $r$ )	m	0.0105	0.0105	0.0105	0.0105	-

Power after losses	W	3.83E-03	3.79E-03	3.70E-04	3.29E-04	$P_{refl} \cdot t_{filter} \cdot t_{lens}$
FWHM diameter at target	m	5.97	5.85	5.78	5.73	$2(dist \tan\left(\frac{div_{FWHM}}{2}\right) - \frac{\phi_{FWHM}}{2})$
Gauss-1/e <sup>2</sup> -Radius after Distance	m	5.07	4.97	4.91	4.86	$\phi_{FWHM} / \sqrt{2 \cdot \ln(2)}$
Axial intensity	W/m <sup>2</sup>	9.47E-05	9.78E-05	9.78E-06	8.85E-06	$\frac{2P_o}{\pi w_o^2(z)}$
Received power ( $P_{rx}$ ) (Gaussian)	W	4.80E-08	4.96E-08	4.95E-09	4.48E-09	$P_o \left[ 1 - e^{-\frac{2r^2}{w_o^2(z)}} \right]$

Table 14: Camera link budget calculation

With the link budget calculation done, even with the smallest divergence where the photodetector receives most of the power, the camera should be able to at least see 20 x 20 pixels beam with 100 ms exposure and a minimum value of 100.

$$4.48 \cdot 10^{-9} > 0.62 \cdot 10^{-9}$$

With this, all the previous calculations have been made, and the validation data has been acquired.

### 3.4 Telemetry

Before beginning this section, it is important to note that no data is transmitted via the optical link described above. This is because the aim of the project is to align the beam and verify that the beam parameters match the expected values.

Here, “data transmission” refers to transmitting the measurements collected by the photodetectors on the Test Target. The Test Target is designed so that the operator, positioned on the transmitter side, can monitor the beacons. This position provides direct access to the images collected by the camera, as it is located in the transmitter. Additionally, the operator must have access to the photodetector data for the complete analysis. To transmit the analog data from the photodetectors to the transmitter side a radio frequency (RF) link and a data acquisition device have been used.

The setup is as follows. The photodetectors provide an analogue output of 0 to 10 V in our case. This BNC output is connected to the data acquisition device via screw pin terminals, noting that the output is single ended rather than differential, which is important for the configuration. The data acquisition device mentioned is the Multifunction Ethernet DAQ Device (MCC E-1608) [39], which can be seen in the left of Figure 37. It has the option of connecting an RJ42 Ethernet cable, which allows data to be sent directly through the RF link antenna. Regarding the important specifications, the DAQ has the option of using 8 single-ended analogue inputs if more photodetectors are needed. Its input bandwidth (BW) is 700 kHz. Since the relevant signal is below 5kHz, post processing is required to remove the noise and interference. In hindsight, no filtering is done, but it should be noted that in other scenarios this could be a problem.

On the other hand, the radio frequency link is composed by two Airmax Powerbeam 5ac gen2 [40], shown on the right of the Figure 37. This RF link consists of one antenna that acts as an access point and another that acts as a station. It works as follows: the access point connects to the device containing the data (the DAQ on the Test Target) while the device requesting data (a computer) connects via the antenna configured as a station.



Figure 37: Multifunction Ethernet DAQ Device (MCC E-1608) (Left) and Airmax Powerbeam 5ac gen2 (Right) used for telemetry [39], [40]

Each antenna is configured differently, and the explanation can be found in the Second Annex (Radio frequency link setup). Now that the operation has been explained, there are several things to keep in mind for the setup to work. To begin with, the antennas must have good visibility and there must be no objects obstructing the connection, in addition to being connected to a power source.

On the other hand, the power beams were initially purchased with the “plug and play” configuration. It has been shown that this configuration is not necessary since the antennas are configured to be able to attach to an existing network with DHCP active. In our case, there is no existing network or router with DHCP, as it is not needed for our project.

Since this is a small network with few components and no plan for expansion, a static network was chosen. This static network is composed of four elements that need an IP address, and the address management is not as complex as implementing DHCP in the network. All components support static IP configuration, which was set during the initial setup with no plan to change them.

All electronic devices connected to the network must have IP addresses within the created network range. In this project, the global network is 192.168.0.0/24 since the default IP of the DAQ is 192.168.0.101, as can be seen in the appendix and its datasheet [39]. The configuration of each device can be seen in Figure 38 below.

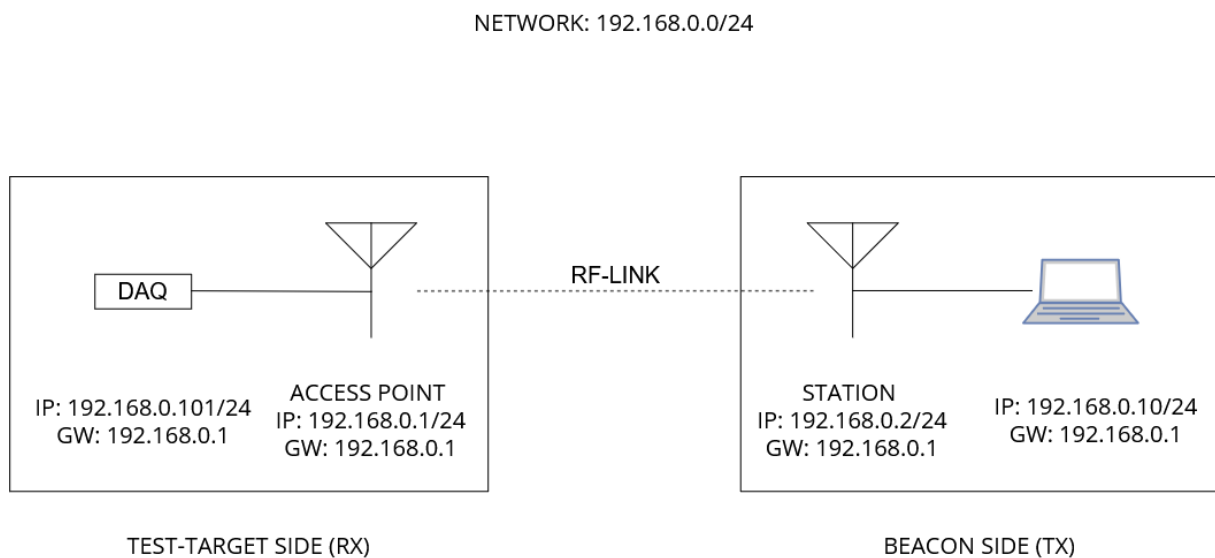


Figure 38: RF Link setup

The configuration shown in Figure 38 is the one that has been used in our project, but it can be adapted depending on the needs of future projects and setups.

Additionally, to display the data from the photodetectors, a pre-existing interface has been used. The interface is called DAQAmi and, in addition to being intuitive, it allows data to be saved. It is explained in subsection 4.1.1.

## 4 Experimental development

Now that the theory and calculations prior to the tests have been presented, this section describes the methods used to acquire the data for analyzed. The interfaces employed throughout the project are also discussed, along with the alignment procedures and divergence calculations.

To determine the beam divergence, the data processing steps used to extract the relevant parameters are explained, and the results obtained from various tests are presented and analyzed. This is followed by an evaluation of these results.

Before starting with the data acquisition methods, a final summary of all parameters considered for the tests is provided in the table below and the list of components used in this project is provided in Table 16.

Parameter	Value
Distance	325 m
Wavelength	1550nm → 1562 nm
Number of transmitters	2
Number of receivers	2
Photodetector Gain	30 dB (47.5kV/A)
Collimators used	0.925mrad, 0.545mrad, 0.329mrad, 0.164mrad
Power used for each collimator	10 mW, 10 mW, 1 mW, 1 mW
Expected power at receiver	29.1 $\mu$ W, 83.7 $\mu$ W, 22.8 $\mu$ W, 88 $\mu$ W
Expected voltage values	1.4121 V, 4.0547 V, 1.1032 V, 4.2640 V

Table 15: Final specifications for test

Purpose	Component	Thorlabs code
TRANSMISOR	0.925mrad collimator	F110FC-1550
	0.545mrad collimator	F220FC-1550
	0.329mrad collimator	F280FC-C
	0.164mrad collimator	F810FC-1550
	Adjustable focus collimator	RCF15A-P01
	Precision Kinematic Mirror	KS1
	Patch Cables FC/PC to	P5-1064Y-FC-2
	Mating Sleeve	ADAF4
	Butterfly Laser Diode	FPL1009S
	Temperature Controller	CLD1015
	Goldeye G-130 TEC1	-
	f <sub>l</sub> = 200 mm lens for camera	AC254-200-C
	1550nm filter	FBH1550-30
TEST TARGET	InGaAs Detector	PDA20CS2
	f <sub>l</sub> =30mm lens for detector	AC254-030-C
	Retroreflective foil	03120020-1220-10
RF-LINK	Airmax Powerbeam 5ac gen2	-
	Multifunction Ethernet DAQ	MCC E-1608

Table 16: Components used for the project

In Figure 39, the implemented setup is shown. The Test Target, located on the IKN rooftop, is displayed on the right, while the transmitter with the collimators and the camera can be seen on the left.



Figure 39: Test setup. Test Target at IKN (Left) and Transmitter at GSOC (Right)

## 4.1 Data acquisition

The different data acquisitions methods for each parameter are discussed in this section. The available pre-existing interfaces are listed, as well as the alignment procedure previously carried out to obtain the data from these interfaces.

The two main parameters analyzed in this project are the received power and the divergence of the beam. The received power can be directly obtained from the photodetectors and analyzed using an interface recommended by the data acquisition device's manufacturer. This interface will be discussed in the following subsection.

In contrast, the divergence of the beam cannot be directly measured without post processing. In this project, the camera images are used as the data source for calculating the divergence. These images are handled in two ways: by saving a 10 second interval of frames and then processing them afterwards, or by processing the frames in real time without saving them. The first method is applied for the fixed divergence collimators, where a pre-existing interface is employed to save the images. The second method, based on real time processing, is used for the adjustable collimator, for which a custom interface was specifically developed to meet the project requirements.

The process of developing this custom interface is explained in section 4.2 while the pre-existing interfaces are discussed in the next subsection.

### 4.1.1 DAQami

DAQami is a user-friendly, drag-and-drop data acquisition software from Measurement Computing (MCC). It allows users to acquire, view, and log data from supported DAQ devices, such as the one used for this project (MCC E-1608). DAQami supports analog, digital, and counter input channels, as well as analog and digital output channels [41].



Figure 40: DAQami interface example [41]

For the input channels, it offers both single-ended and differential modes. In this project, the single-ended mode is used, with a voltage range between 0 – 10 V, and only two of the eight available channels are required. Despite this limited use, the number of available channels makes both the DAQ device and the interface highly scalable, but the project only uses two. It also provides the option to modify the sample rate, which in this case was set to 10000 samples per second. Additionally, it allows users to select different display types for effective data visualization.

All of the choices are consistent with the selected photodetectors: they provide an output range of 0 – 10 V and deliver the signal in a single-ended form, not differential.

Since the received power at the photodetectors has already been converted to voltage, simply visualizing the data on screen and comparing it to the calculated link budget values is sufficient for tasks such as verifying alignment.

To process the data, the interface includes an option to export the acquired data as an Excel file. For this project, 15 seconds of data were first recorded with the lasers switched off in order to estimate background noise, followed by 15 seconds of data acquisition with the beams on. The data was then stored and labeled accordingly for later analysis.

### 4.1.2 Vimba X Viewer

For the image data acquisition and storage, the Vimba X Viewer interface was used. Vimba X Viewer is a component of Allied Vision's Vimba X SDK that allows users to control and configure Allied Vision cameras, including the Goldeye G-130 TEC1 used in this project. It provides a graphical interface for adjusting camera features and acquiring images without the need for programming. The viewer is part of the larger Vimba X SDK, which is a comprehensive software development kit for machine vision and embedded vision cameras [42].

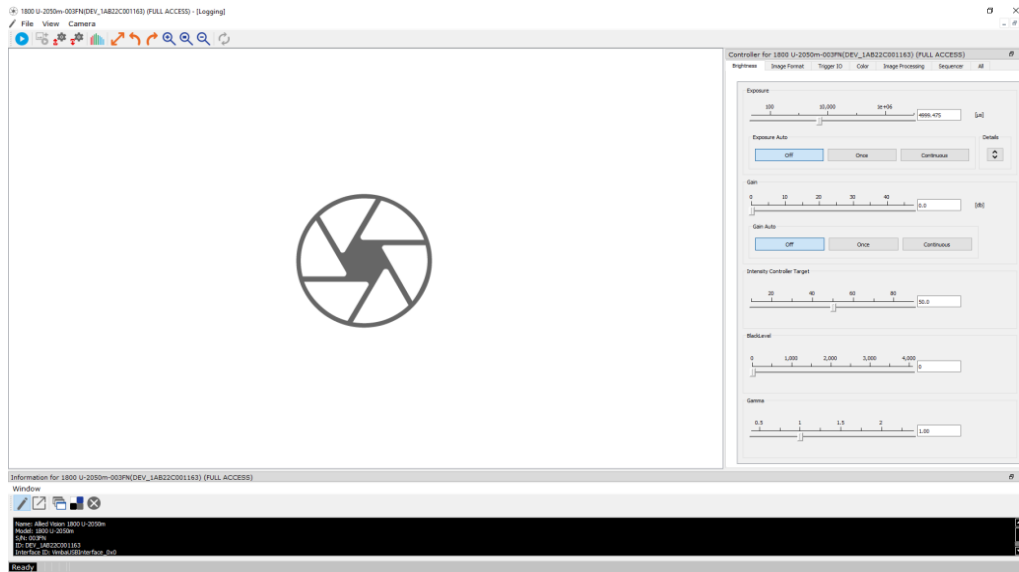


Figure 41: Vimba X Viewer interface example [42]

Within this interface, it is possible to adjust parameters such as exposure, gain and black level of the images being recorded. In this project, all parameters were left at their default values except for the exposure time. Exposure had to be adapted for each collimator and power level to ensure the beam was correctly captured. The chosen exposure range was between 0 ms to up to 1 ms. Exposure times longer than 1 ms were avoided, as capturing images more than 1ms apart could make scintillation effects more apparent. If the exposure time is less than 1 ms, the averaging of the images could be used to mitigate the scintillation effect.

To maximize data accuracy, the 16-bit acquisition mode was selected. As expected, this setting saved the images as 16-bit files. However, when analyzing the images, it was revealed that the images contained 12-bit of actual data with 4-bit of padding.

Finally, similar to the photodetector measurements, image data was recorded in 15 second intervals for each acquisition.

### 4.1.3 Alignment process

Aside from the beam's divergence, the directional alignment of the beacons is also crucial to achieve precise tracking. Using the Test Target, the beam can be directionally adjusted to ensure proper alignment. This section describes the alignment process carried out during the tests.

Both the retroreflective foil and the photodetectors play a significant role in adjusting the beams. In the tests, the retroreflective foil and the camera were first used to roughly locate the beam and center it onto the photodetector. Figure 42 shows two images: one with a higher exposure, highlighting the test environment and another with a lower exposure, illustrating how the beam can be identified and how it appears on the camera.

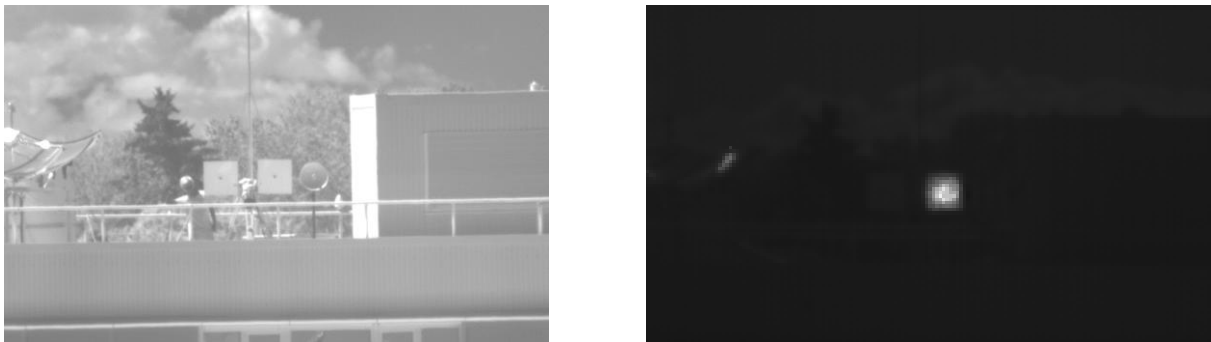


Figure 42: Directional alignment with camera and reflective foil. Camera image with high exposure to see the test target (Left). Lower exposure to show the beam alignment in the test target (Right)

The camera and retroreflective foil are used for the initial alignment. Once the beam is located, the photodetectors are employed for the fine adjustment. The alignment process with the photodetectors is quite simple: the voltage displayed in the DAQami interface must be maximized to consider the beacon properly aligned. To determine the point of maximum power, a strip window is used, and the mean of the signal within this window is taken as a reference value. Figure 43 shows the DAQami interface, where the different colors represent the two different photodetectors. Their value changes over time. By adjusting the tip tilt mount, the beacon's direction was modified, and the beacons were adjusted.

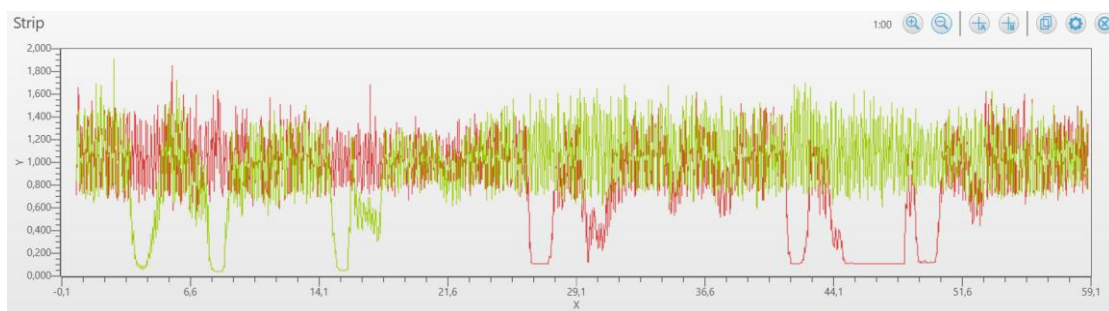


Figure 43: Directional alignment with photodetectors received power/voltage. Green and red plots are the voltage values of the two photodetectors. X axis is time and Y axis is the voltage value

As mentioned above, a correct alignment is considered when the received value from the photodetector is as high as possible. With this, the first objective on beacon adjustment is complete.

### 4.1.4 Divergence calculation

For the divergence calculation tests, the four previously established fixed divergence collimators were used. These tests not only served to verify that our methodology was valid but also to confirm that the fixed divergence collimators sold by the fiber manufacturer were properly adjusted and matched the values specified in their datasheets.

After completing the tests with the fixed divergence collimators, an adjustable focus collimator was also tested. To do this, an interface capable of calculating the divergence angle in real time was developed. In practice, this interface would be used to adjust the divergence angle of the OGS beacons.

Two different approaches were chosen to calculate divergence. Using the camera images to calculate the divergence and using the detected power at the receiver. This section explains both methods for extracting the beam divergence and discusses the challenges of each of the processes.

The interface created for real-time divergence calculation with the adjustable focus collimator is also described.

#### 4.1.4.1 Camera image processing

This subsection describes the processing of the images taken with the Goldeye camera. Before addressing the processing steps, it is important to note that the exposure settings differed for each collimator. To acquire useful images, the beam spot cannot be saturated. Thus, the exposure was adjusted in each case to fit said condition.

The first step on obtaining the divergence from images is to correct the pixel intensity fluctuations caused by atmospheric turbulence, specifically scintillation. This was achieved by using an exposure time of less than one millisecond and averaging at least 5 seconds of image acquisition.

Scintillation refers to the rapid fluctuation in the intensity of a light beam caused by propagation through atmospheric turbulence. Random variations in the air's refractive index induce fluctuating interference patterns in the beam plane [24]. These fluctuations deform the gaussian shape of the beam, and preserving the Gaussian distribution is essential for the divergence analysis.

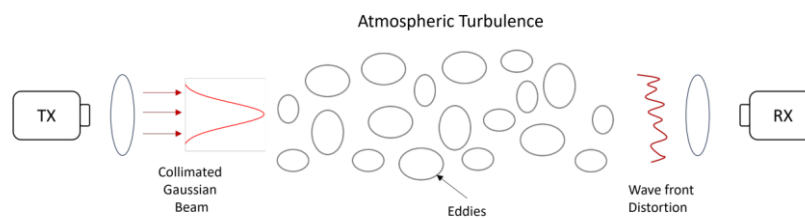


Figure 44: Atmospheric turbulences [13]

To clearly capture scintillation, the camera must operate with an exposure time much shorter than the characteristic speed of atmospheric turbulence. Studies in speckle imaging show that exposure times shorter than the atmospheric coherence time, which is typically a few milliseconds in infrared, is required to see the true speckle structure [43],[44].

With this said, a mean of the recorded images was computed. An example of this averaged result is shown in the figure below. The averaging process produces an image that resembles a Gaussian distribution, with the maximum intensity located at the center and a gradual decay towards the edges.

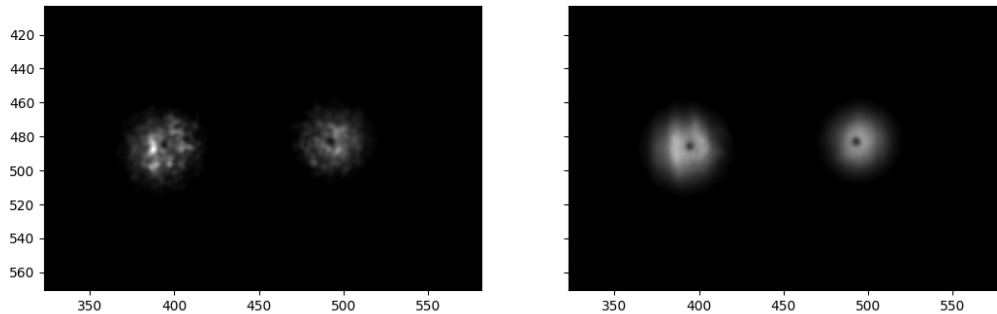


Figure 45: Single captured image (Left) and the mean of 200 captured images (Right)

After averaging, the beam's intensity distribution is extracted. To get the intensity distribution, the beam center is first located, and then the intensity values along the central column of pixels were taken. During this step, filtering was applied to remove unwanted artifacts from the image. In some cases, strong reflections were seen in the images and it was decided to filter them by size, roundness and saturated pixel. Since the beams cannot be saturated in order to get the Gaussian shape, the saturated pixels can be used as a filtering method. The beams are also round and for the divergences used in the project, their area is more than a few pixels large. With that knowledge and the dedicated python libraries, the unwanted elements were filtered successfully.



Figure 46: Example of captured images with unwanted reflections that were filtered in image processing

To calculate the beam centers, a mask was created using an adaptive threshold. The mask was then processed using functions from the skimage library to identify the connected components, extract their borders, and automatically calculate their centers.

However, while calculating the beam centers and extracting the intensity distribution, some drawbacks were identified. If the images are taken with the beam centered in the photodetector, the photodetector cuts off the Gaussian distribution that is needed for the divergence analysis. To fix this, the beams were intentionally shifted to the side, ensuring the full Gaussian shape could be captured in the images.

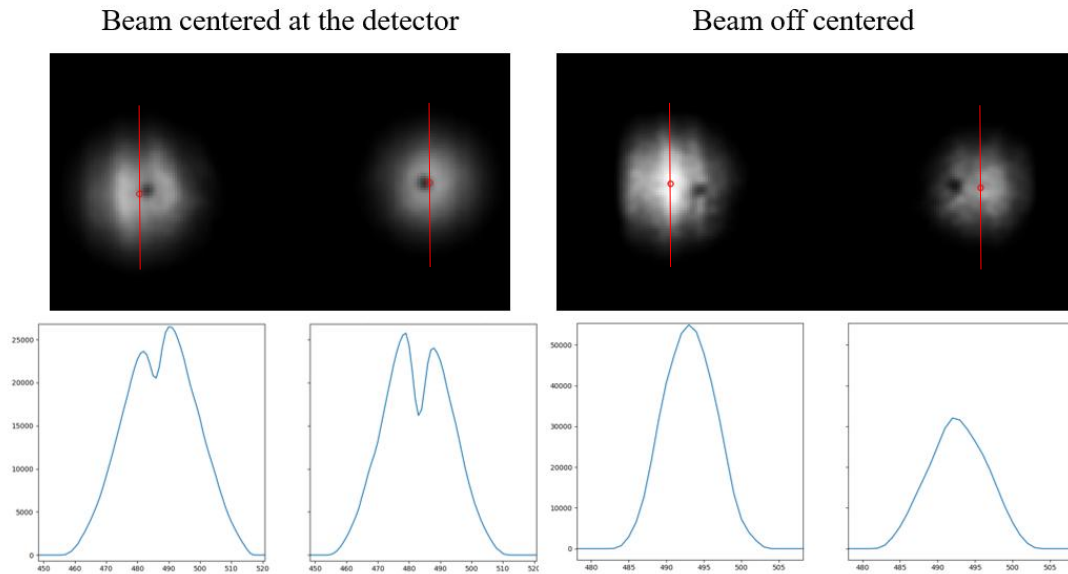


Figure 47: Beam centered and not centered on photodetectors. Center of the beam indicated with a red circle. Vertical cut for intensity distribution below each beam spot. Non-Gaussian distribution (Left) and Gaussian distribution (Right)

Once the intensity distribution was extracted, an interpolation with a resolution factor of 4 was applied in order to increase the effective pixel density beyond the actual resolution of the camera. This interpolation step was necessary to achieve a more accurate estimation of the beam divergence. After interpolation, the intensity distribution was normalized, and the two points where the normalized intensity reached 0.5 were identified. For these points, the beam's FWHM diameter was determined, which was then used to calculate the divergence of the beam.

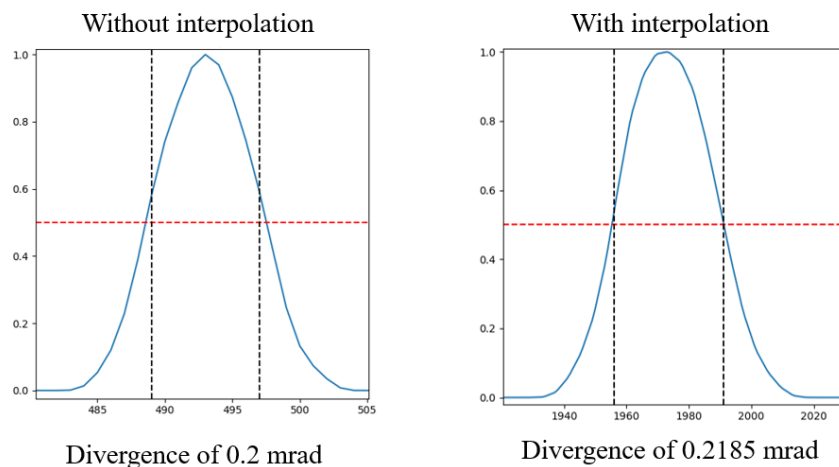


Figure 48: Divergence calculation with and without interpolation. Both zoomed in for better representation

In the image above illustrates the effect of interpolation. In the right graph, the x-axis corresponds to the 4x interpolated resolution, while the left graph shows the original data. Although both methods obtain similar divergence estimates, the interpolated data provides a smoother profile and therefore a more reliable measurement.

The divergence calculation requires converting the measured spot size in pixels into a physical dimension. This was achieved by using the known focal length of the camera lens, the physical size in the measurement plane and the field of view per pixel.

$$FOV_{pixel} = \frac{pixel\ size}{camera's\ focal\ length} = \frac{0.005}{200} = 25\mu rad \quad (11)$$

$$Physical\ size\ of\ object\ seen\ by\ 1\ pixel\ (mm) = FOV \cdot distance = 25\mu rad \cdot 325\ m = 8.125\ mm \quad (12)$$

The conversion from beam diameter to beam divergence is the one shown in equation 13, the divergence can be calculated.

$$\theta_{FWHM} = 2 \cdot \arctg\left(\frac{\phi_{FWHM}}{2 \cdot dist}\right) \quad (13)$$

As an example for Figure 48, each pixel corresponds to approximately 8.125mm on the image. The calculated diameter of the Gaussian beams at FWHM are 8 pixels in case of non-interpolation and 8.74 pixels in case of interpolation, the beam diameter can be convert to mm by multiplying the values. After getting the diameter value in mm, the divergence can be calculated with equation 13 obtaining the values show in Figure 48.

Finally, a flow graph summarizing the entire image processing and divergence calculation procedure is provided in the figure below. More details of the code can be found in Annex 1.

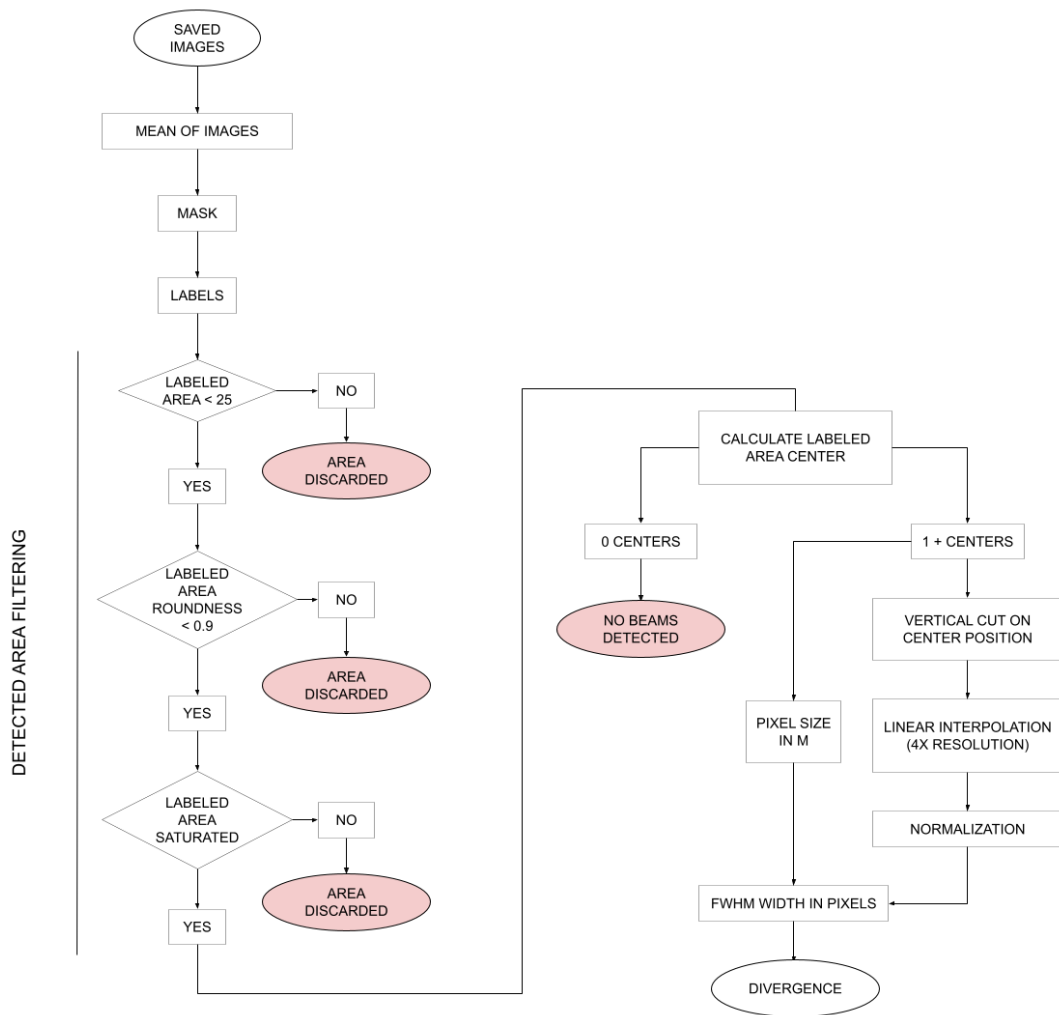


Figure 49: Flow graph of divergence calculation process from camera images

## 4.1.4.2 Photodetector data processing

In this second method, the beam divergence is determined by using the photodetector measurements. As described in the DAQami interface section, a 15 second recording is first taken with the lasers turned off to estimate the background noise. Then, another 15 second acquisition is performed with the beams on.

Similar to the camera image processing, fluctuations in the intensity caused by atmospheric turbulence are mitigated by averaging the recorded voltage. The measured voltage is then converted into the received optical power following the procedure described in section 3.3.3.1. This allows a direct comparison with the theoretical power obtained from the link budget.

If the measured powers match the link budget calculations, it can be assumed that the beacons are well aligned within a certain error margin. However, the beams divergence is also calculated in our project. To do that, an inverse version of the link budget is calculated to get the divergence associated to the received power at the detector.

An example of the procedure shown in the table below. All formulas are the explained in sections 2.3 and 2.4.

Parameter	Unit	Divergence calculation	Formula
Power at source ( $P_{tx}$ )	W	0.01	-
Distance	m	325	-
Filter transmissivity	1	0.9	-
Lens transmissivity	1	0.95	-
Receiver aperture ( $r$ )	m	0.0105	-
Power after losses ( $P_o$ )	W	8.55E-03	$P_{tx} \cdot t_{filter} \cdot t_{lens}$
Received power ( $P_{rx}$ )	W	22.82E-06	detected
Gauss-1/e <sup>2</sup> -Radius after Distance( $\phi_{e^{-2}}$ )	m	0.2886	$\sqrt{\frac{-2r^2}{\ln\left(1 - \frac{P_{rx}}{P_o}\right)}}$
FWHM diameter at target ( $\phi_{FWHM}$ )	m	0.3398	$\phi_{e^{-2}} \cdot \sqrt{2 \cdot \ln(2)}$
Full divergence at FWHM	mrad	1.046	$2 \cdot \arctg\left(\frac{\phi_{FWHM}}{dist \cdot 2}\right)$

Table 17: Example of divergence calculation from detected power

## 4.1.4.3 Interface for real time processing

In this section, the interface created to calibrate adjustable collimators is explained. The actual image processing follows the same steps as for the saved images described in section 4.1.4.1, so it is not explained in this section for a second time.

The interface was created using Vmbpy, the Python API that is provided by Vimba X SDK. Vmbpy provides access to the full functionality of Vimba X in a pythonic way, allowing for rapid development of applications [45]. Using the provided examples, a custom interface was developed, as shown in Figure 50.

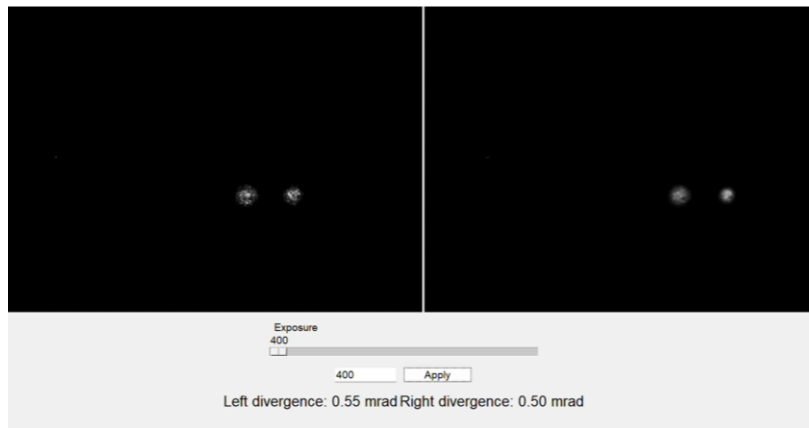


Figure 50: Interface created for adjustable collimator calibration with low exposure

In this interface, the exposure can be adjusted to prevent the beam saturation. The left images display the real time capture, where any saturated pixels are highlighted red for easier identification and adjustment. The right images show the mean of the last 20 frames to counter the scintillation effects. They also display the contours of the detected elements and their centers. Both the saturated pixels and the detected elements with their centers can be seen in Figure 50. Lastly, the divergences of the left and right beams can be seen at the bottom of the interface.

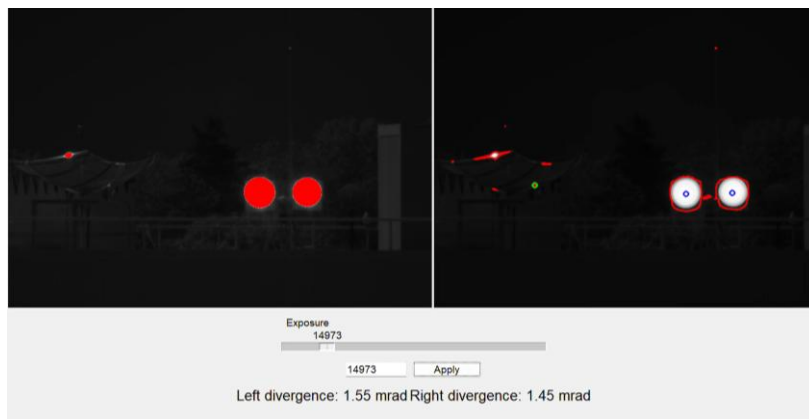


Figure 51: Interface created for adjustable collimator calibration with high exposure

The interface was updated so that the mean of the images is calculated with fewer frames, and a buffer was created to store said images for real time processing.

With this, all the processes for data acquisition have been explained, to show the results in the next section.

## 4.2 Results & Discussion

This section presents and analyzes the results obtained in the tests conducted in this project. The main purpose is to clearly show the most relevant information and discuss the significance of the results in relation to the objectives that have been previously defined.

First, the results obtained from the camera images are presented and compared with the theoretical expectations established previously. Next, the results from the detected power are discussed, concluding with a comparison between the two methods used to measure beam divergence.

Throughout the project, tests were conducted on multiple days under different conditions. Early tests have been discarded due to improvements made afterward, including: aligning the Test Target correctly so that the photodetectors receive the maximum power, properly focusing the photodetectors lenses, and using a single gain setting instead of multiple ones, as was done in earlier tests.

Although several tests were carried out, the most optimal and best implemented test was the final one, which is analyzed in detail in this section. Regarding the camera images, reference is also made to earlier tests because, while the alignment, focus of the sensor and gain were improved, the reflected beam itself remained the same.

### 4.2.1 Divergence from camera images

This section presents the results obtained from processing the images collected by the camera. As shown in the example in Figure 52, atmospheric turbulence is easily observable causing fluctuations in beam intensity. These fluctuations were consistently seen across all tests conducted during the project.

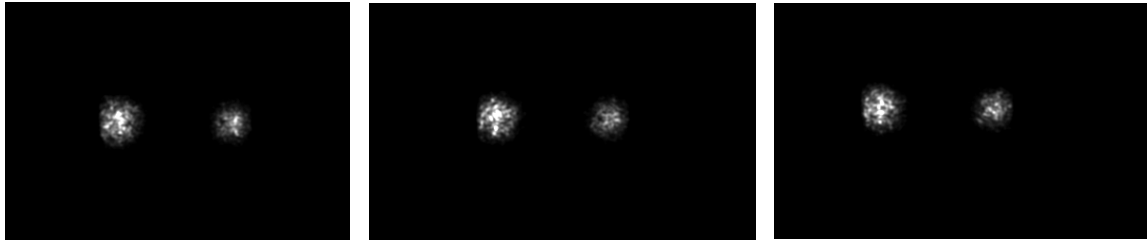


Figure 52: Atmospheric turbulence example: 0.545 mrad beam at 500 $\mu$ s exposure at different times

After processing the images according to the method described in section 4.1.4.1, the results for each group of images are summarized in Table 18. This first table shows the measurements obtained during the final and most optimized test, where the images were taken both with the beam centered at the photodetectors and slightly offset.

Parameter	Unit	Beam	Fixed divergence collimators			
Collimator $\theta_{FWHM}$ from datasheet	mrad	-	0.926	0.545	0.329	0.164
Recorded $\theta_{FWHM}$ beam centered	mrad	L	0.8806	0.7681	0.6058	0.143
		R	0.7931	0.5433	0.4808	0.162
L		1.0367	0.7119	0.6869	0.2185	
R		1.0679	0.662	0.5808	0.2435	

Table 18: Divergence calculation results from camera images with fixed divergence collimators

The graph of the measurements is made for better representation, some tendencies can be seen (Figure 53).

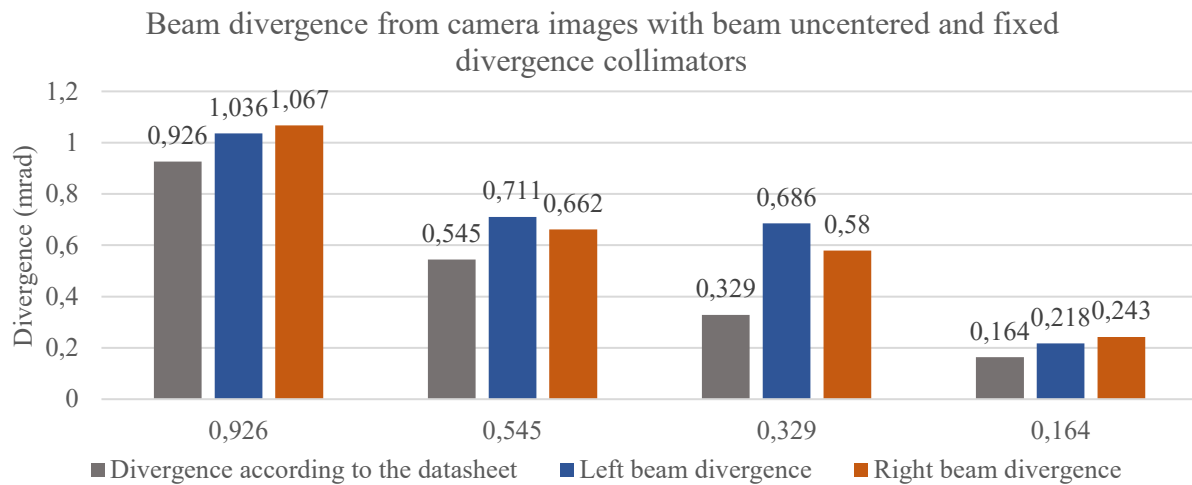


Figure 53: Graphical representation of the divergence calculations from camera images with uncentered beam in photodetector and fixed divergence collimators

The graph shows the different measurements done for each collimator. In each group of three columns, the first column indicates the expected divergence as specified in the datasheet, while the other two columns show the measured divergences of the left and right beams obtained from the camera images.

Two clear tendencies can be observed in the data. First, all measured divergences are slightly larger than the values given by the datasheet. This enlargement is expected because the divergence is calculated using the mean of multiple images. Averaging the images causes the beam spot to appear larger due to the beam wander, which results in a slightly larger measured divergence.

Beam wander refers to the random displacement of a laser beam's central position as it propagates through the atmosphere. Atmospheric turbulence introduces fluctuation in the air's refractive index, which act like small lenses that deflect the beam, leading to a wandering motion on the spot at the receiver plane [46], [47].

The amount of beam wander is dependent on the divergence of a laser beam, a narrow beam with a small divergence is more sensitive to turbulence and experiences a larger beam wander. This effect is visible in the measurements: the 0.164 mrad divergence beam has a larger deviation than the 0.925 mrad divergence beam. Wider beams tend to average over more turbulence spots, which reduces the beam wander and results in smaller beam wander variations.

However, even though the beam wander explains the larger measured divergences for most collimators, when analyzing the 0.329 mrad divergence collimators, the divergence mismatch is too large to be considered an effect of beam wander.

In Figure 54, the results of a test done previously are shown and even though the measurements vary a little bit because the final adjustments weren't done correctly, the 0.329 mrad divergence collimator has the same behavior as in the final test: its divergence is considerably larger than what it is described in the datasheet.

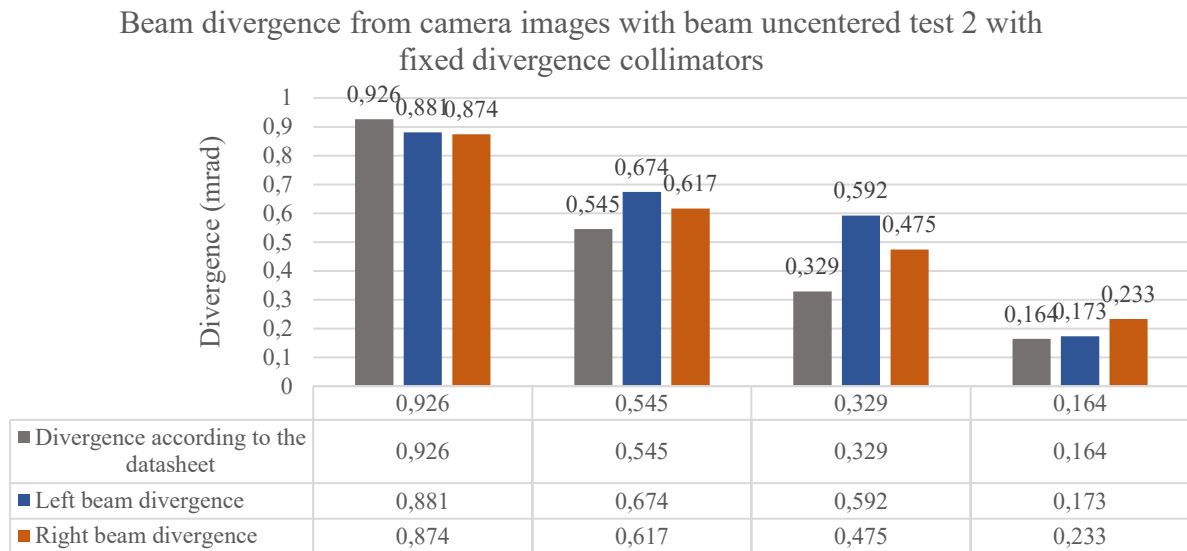


Figure 54: Graphical representation of the divergence calculations from camera images with beam uncentered in photodetector from previous test with fixed divergence collimators

When analyzing the camera images and noticing the unexpected behavior of the 0.329 mrad divergence collimators, the following sections take this behavior into account to either corroborate the calculated divergences or identify potential errors in the divergence measurements.

## 4.2.2 Divergence from detected power

The power recorded at the photodetector was obtained following the procedure described in section 4.1.4.2. The results are summarized in the table below.

Parameter	Unit	Beam	Value			
Output power ( $P_{tx}$ )	mW	L	10	10	1	1
		R				
Collimator divergence $\theta_{FWHM}$	mrad	-	0.926	0.545	0.329	0.164
Equivalent voltage at photodetector	V	L	0.4700	1.3500	0.3600	1.4200
		R				
Recorded background light at photodetector		L	0.1265	0.1044	0.0550	0.0333
		R	0.0464	0.0420	0.0556	0.0320
Recorded mean voltage at photodetector		L	1.23200	2.90590	0.4089	3.4167
		R	1.44130	2.58280	0.7431	2.7111
Final received voltage without the noise	$\mu$ W	L	1.10550	2.80150	0.35390	3.38340
		R	1.39490	2.54084	0.68750	2.67910
Power at photodetector		L	29.1	83.7	22.8	88
		R				
Recorded mean power ( $P_{rx}$ )	$\mu$ W	L	22.82	57.82	7.30	69.83
		R	28.79	52.44	14.19	55.30

Table 19: Power detected at the photodetector with the theoretical power for comparison with fixed divergence collimators

The graph shown below is made to better understand the data that has been collected.

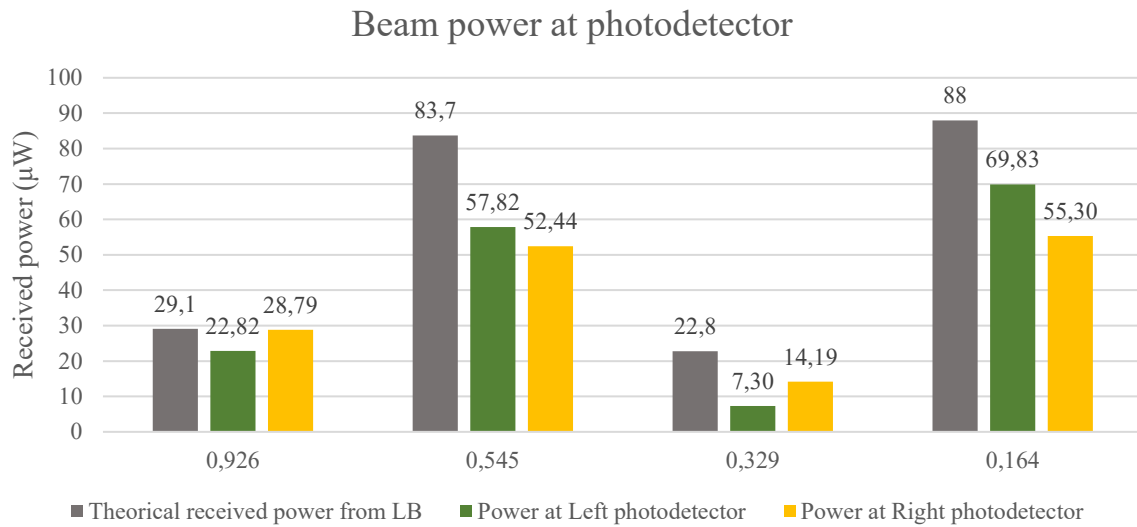


Figure 55: Graphical representation of the results of the received power at the photodetectors with fixed divergence collimators

The graph shows the measurements obtained with each collimator. The first column of each trio indicates the expected received power calculated using the link budget in section 3.3.3.1. The other two columns show the actual received power recorded by the photodetectors.

All values match the expected results within a certain error threshold, except for the collimator with 0.325 mrad divergence. When analyzing the behavior of the collimators, the two tendencies mentioned in the previous section are observed again.

First, in all cases, the value received is slightly lower than expected. This may be due to beam wander and scintillation, both caused by atmospheric turbulence. This margin of error is to be expected, as these possible attenuations were not included in the link budget calculation.

Second, as in the previous section, the collimator with a divergence of 0.329 mrad does not perform as expected. The received power is too low to be associated with losses due to atmospheric effects. In the previous section, the collimators' divergences were greater than specified, and the increase in divergence coincides with the decrease in received power. With a larger divergence, the beam spot becomes wider, and the power density decreases, which explains the power drop seen in the results.

To determine the divergence corresponding to the received power measured by the photodetectors, the procedure escribed in section 4.1.4.2 was followed. The results can be seen in the Table 20.

Parameter	Unit	Beam	Power updated to gaussian			
Full divergence at FWHM from datasheet	rad	-	0.926	0.545	0.329	0.164
Receiver aperture ( $r$ )	m	-	0.0105	0.0105	0.0105	0.0105
Recorded mean equivalent power	$\mu\text{W}$	L	22.817	57.822	7.304	69.833
		R	28.791	52.443	14.190	55.296
Gauss-1/e <sup>2</sup> -Radius	m	L	0.289	0.181	0.161	0.051
		R	0.257	0.190	0.115	0.058
FWHM diameter at target	m	L	0.340	0.213	0.190	0.060
		R	0.302	0.224	0.136	0.068
Estimated full divergence at FWHM	rad	L	1.05E-03	6.56E-04	5.84E-04	1.85E-04
		R	9.31E-04	6.89E-04	4.18E-04	2.09E-04

Table 20: Conversion from received power to Full Width at Half Maximum divergence

A graphical representation of the results can be seen in Figure 56.

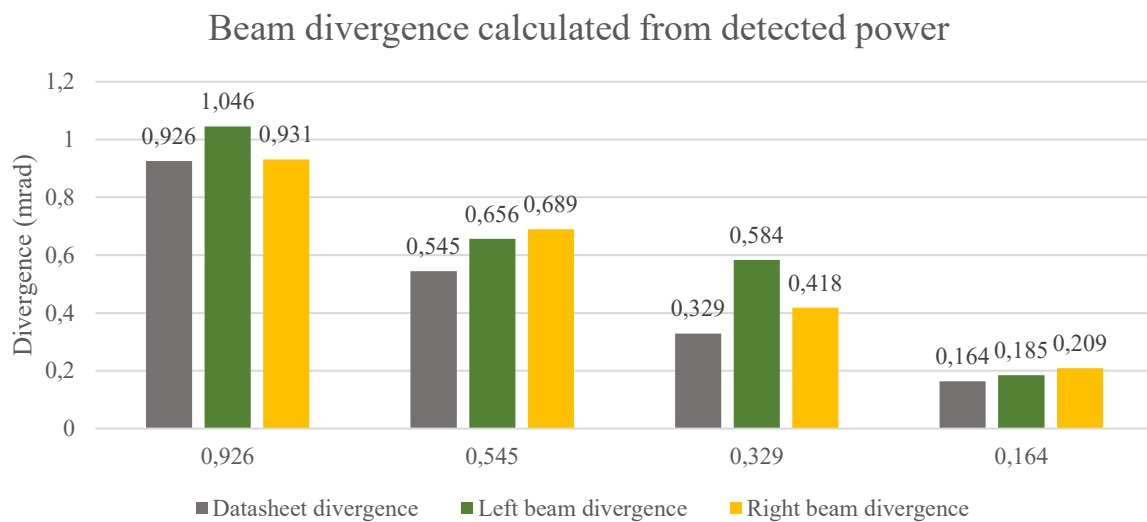


Figure 56: Divergence calculation from receiver power

As expected, the divergence calculated through the received power also indicates that the collimator with 0.329 mrad divergences behavior is not the one that the datasheets state.

### 4.2.3 Discussion

Having obtained the divergences of the collimators from the camera images and the received powers, this section discusses the results. All possible sources of error in the tests are considered and listed, as well as determining a possible solution for them.

Figure 57 presents a comparison between the two methods used to determine divergence and also compares the results with the collimator divergences specified in the datasheets.

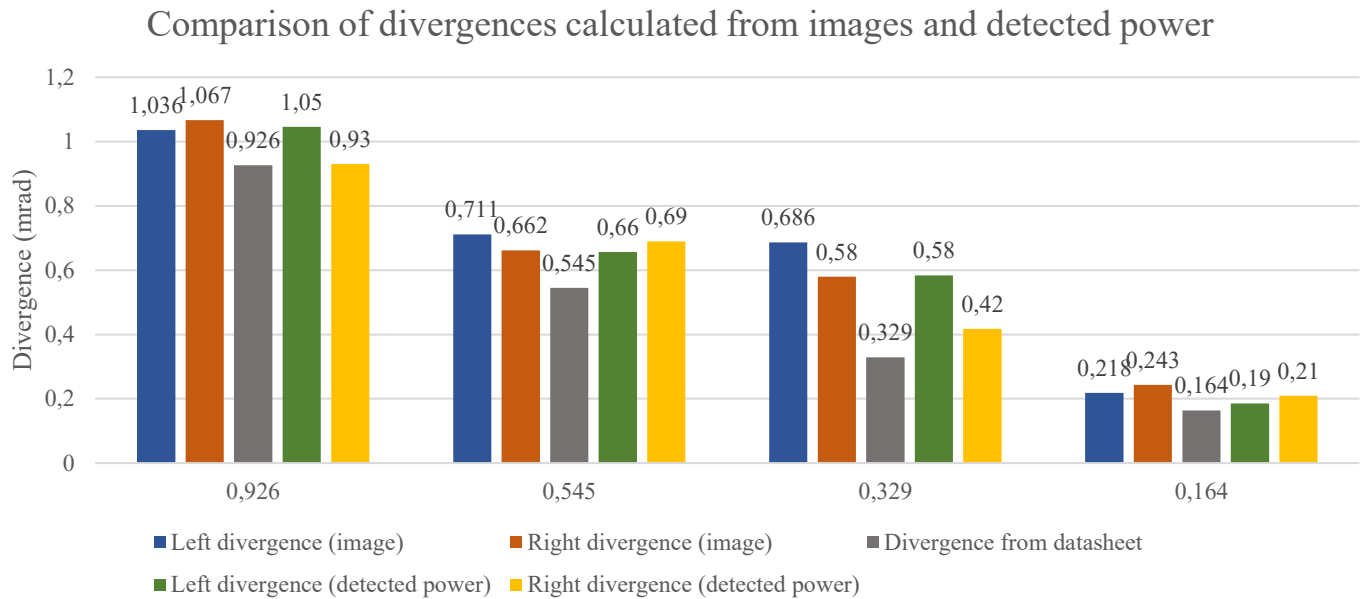


Figure 57: Comparison graph of calculated divergences from images and detected power as well as the datasheet divergences

In the graph above, five values are shown for each collimator divergence. The center value indicates the FWHM divergence specified in the datasheets. The two columns to the left of the center column correspond to the divergence values calculated from the camera images, while the values to the right correspond to the divergences calculated from the detected power. As observed, both measurement methods produce similar results within a certain range. Both methods also confirm the abnormalities of the collimators with 0.329 mrad divergence and both methods calculated a larger divergence because of atmospheric turbulences. Therefore, no single method can be considered definitively better, both methods provide comparable results.

Calculating divergences via the received power has advantages in terms of robustness, as it avoids interference from other reflected beams. It is also more reliable for beam alignment, since it does not depend on the camera's resolution or sensitivity. Adjustments to transmitted power or photodetector gain can be made to improve sensitivity if necessary.

Using camera images relies on the normalized Gaussian intensity distribution rather than the total power at the receiver, which can be affected by scintillation. A limitation of the image-based method is its dependance on pixel size: if the divergence to be calculated is too small and the resolution is insufficient, the calculated divergence can be overestimated. This was observed when attempting to calculate the divergence of a 50  $\mu$ rad collimator, where the gaussian beam could not be detected precisely and a way larger divergence was calculated. Beam wander also has a say in the enlargement of the beams.

Both methods have their advantages and disadvantages. Common sources of error in both cases include environmental conditions, such as performing the tests in broad daylight and high temperatures. These conditions caused the lasers and controllers to heat up, leading to fluctuations in the output power. Part of this issue was solved by moving the controllers to the shade for the tests, but temperature of the setup does affect the outcome of the tests.

Additionally, the filter used should also be considered. Even though a test was done to see the effects of the filter, some of the power could be attenuated more than calculated.

Another potential source of misalignment that could have affected the tests is the focus of the lenses, both on the photodetectors and the camera. If the lenses are not properly adjusted, power is lost in the photodetectors and the camera cannot distinguish the beam with the required precision.

All the misadjustments mentioned above were addressed and corrected before the final test to ensure that the measurements were as accurate as possible.

However, the issue of beam wander, which was initially considered negligible with larger divergence beams, becomes a problem when working with small divergences. In early tests with wider beams, the beam center moved less than a pixel and was therefore disregarded, but this is no longer the case for narrow beams.

Given the unexpected behavior of the 0.329 mrad divergence collimator, a manufacturing defect is considered a likely cause for the divergence discrepancy. These tests highlight the importance of verifying fixed divergence collimators before use, as they can be unreliable.

With that in mind, adjustable focus collimators are therefore a preferable option to achieve exactly the divergence that is required. This is where the custom interface becomes valuable.

The adjustable focus collimator selected was tested after the fixed divergence collimators to create an easier and faster divergence adjusting process. As described in section 4.1.4.3, the interface successfully calculates the divergence.

For example, a collimated stage was firstly tested where the datasheet stated the divergence to be 0.411 mrad. The interface calculated a divergence of 0.47 mrad (Figure 58). Considering the beam wander as an error margin, the calculation can be considered adequate.

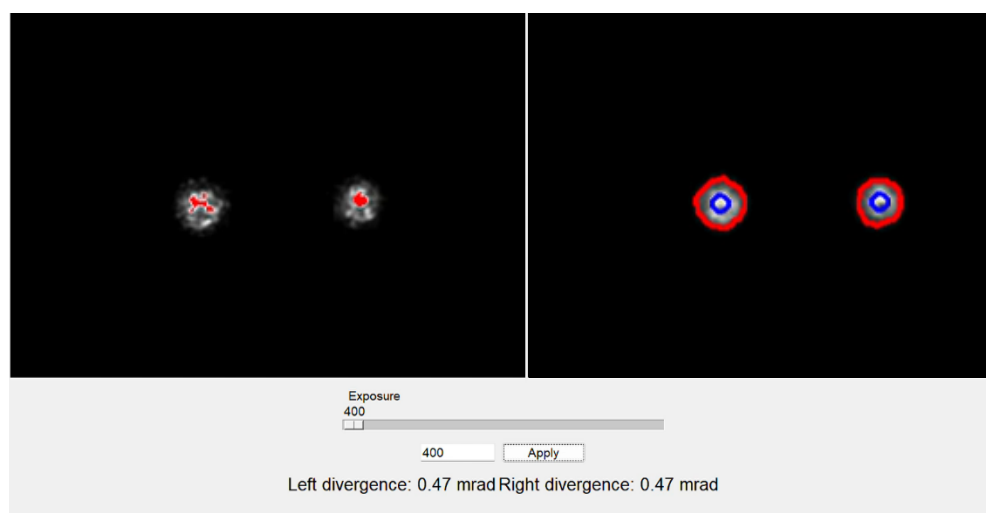


Figure 58: Interface with collimated beams of adjustable collimators

As shown, the beams are successfully detected, and the divergences are calculated. Additional examples, where the collimator was adjusted to produce a divergent beam, are represented in the following figures.

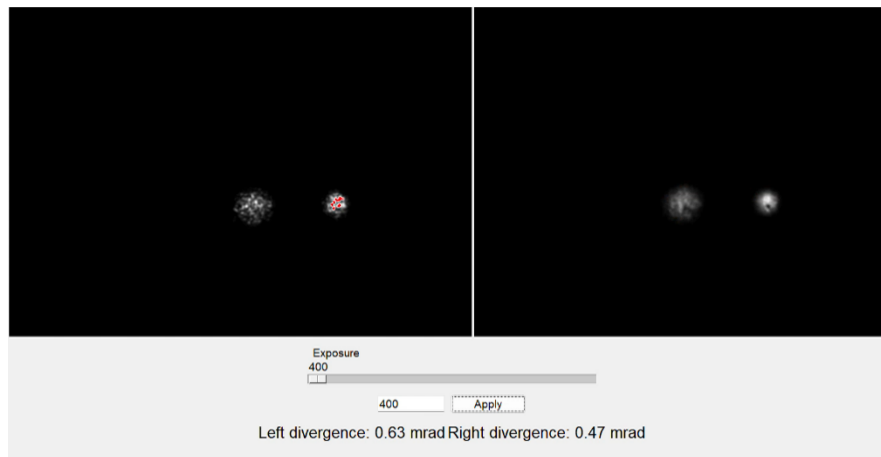


Figure 60: Interface with one collimated beam (Right) and one divergent beam (Left) of the adjustable collimators

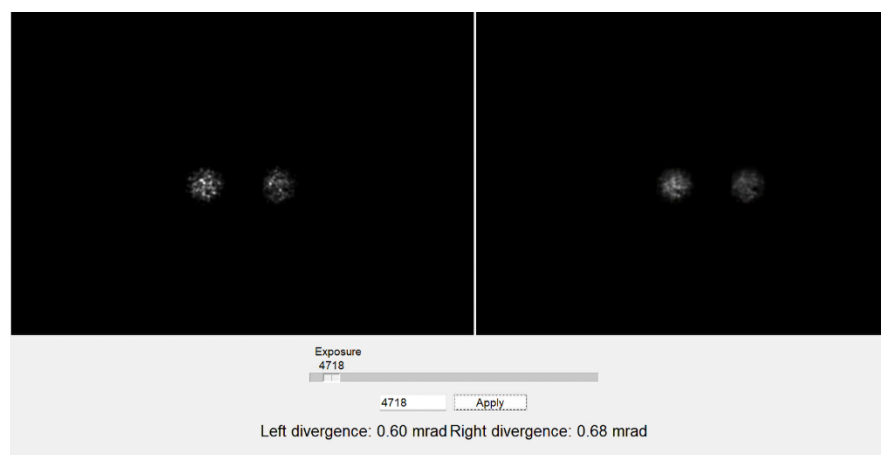


Figure 59: Interface with two divergent beams of the adjustable collimators

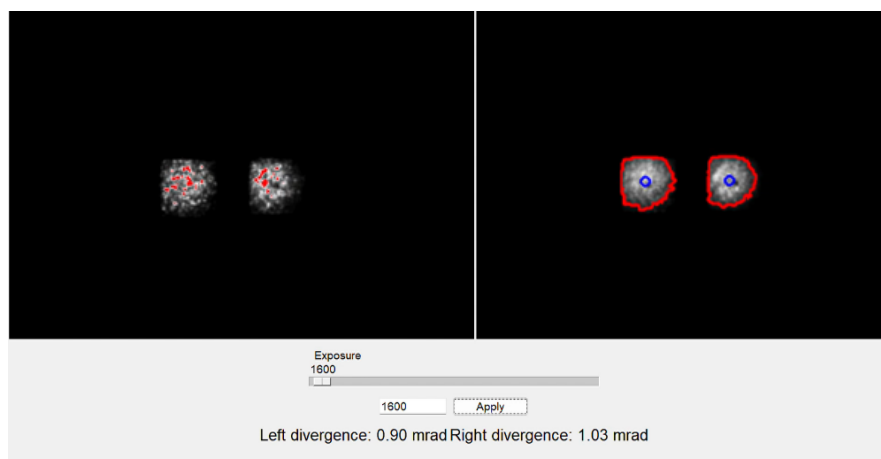


Figure 61: Interface with the maximum divergence adjustable collimators

With this, an interface for the proper adjustment of adjustable focus collimators has been created. It should be noted that during the tests, a problem arose when obtaining data from the photodetectors: when the adjustable focus collimator was defocused, the direction of the beam shifted, causing the beam to become misaligned while acquiring data from the photodetectors. Due to time constraints, these tests could not be repeated, but they should be redone in the future to ensure accurate measurements.

## 5 Conclusion

Free space optical (FSO) communications are an emerging technology that enables wireless high speed data transmission through light propagation. Unlike traditional radio frequency, FSO offers a larger bandwidth, lower latency, and high security, making it a promising solution for satellite communications, especially in low Earth orbit (LEO) networks.

In the context of LEO data downlinks, one of the challenges is to maintain precise alignment between the satellite and the optical ground station (OGS). This is where the beacons play a significant role. Beacons are used for satellite tracking, serving as a reference point for the satellite's optical terminal to lock on to. The adjustment of said beacons must be precise for the pointing of the satellite to be successful and various sources of error exist.

This project focuses on the design of a dedicated device to optimize beacon alignment, both directionally and divergence wise. The system can analyze the beams direction, divergence, and power to accurately adjust the beacon. Experimental results demonstrate the need for such a device.

After performing the necessary tests, the manufacturing error of a fixed divergence collimator was detected. This implies the possibility that more collimators with manufacturing errors are being produced and need to be identified and supervised. The collimation defects of the beacons affect the beam quality and alignment. To ensure the use of a collimator with the specific divergence required in each project, the use of focus-adjustable collimators is recommended.

Moreover, the proposed device and additional interface simplify and facilitate the alignment process for adjustable focus collimators by calculating the beams divergence in real time. This function not only improves the reliability of beacon alignment but also facilitates and speeds up the setup process, reducing error margins.

In conclusion, the device and interface designed in this project have proven to be a useful tool for beacon alignment. Its integration facilitates both the directional alignment and the divergence adjustments of the beacons, contributing greatly to the efficiency of optical satellite communications infrastructure.

### 5.1 Future work

Although the proposed device has demonstrated its utility in aligning beacon systems, there are several ways to improve the device that could make the Test Target more robust as well as expanding its functionality.

One key improvement would be the correction of the beam wander. As explained in the result section, the beam wander currently affects the accuracy of the measurements, particularly for small divergence beams. Stabilizing the beam position during camera image processing would make the device more accurate and less affected by the atmospheric turbulence, making it more dependable.

Another area of improvement is the optical filtering system. Replacing the chosen filter with one centered in the selected wavelength or with one with a bigger bandwidth would also improve the measurement accuracy.

The Test Target itself could also be reinforced. For example, stabilizing the retroreflective foil would make the target more robust in windy conditions, making a more consistent and stable reading possible.

In addition, future tests could account for atmospheric irradiance (IRT) effects. While IRT influences the measurements performed during broad daylight on hot summer days, observing the system during the evening or nighttime could reduce these effects. This would lead to a less beam broadening and improve measurement accuracy, particularly for small divergence beams. Larger divergence beams are less affected by IRT, so their measurements are expected to be more reliable.

Moreover, future designs should also consider the implementation of larger transmitter apertures. Larger apertures are advantageous because they reduce the relative impact of atmospheric turbulence on the beam by averaging over more turbulent cells, which results in less beam broadening and wander.

From a practical standpoint, larger optical components are also easier to align and adjust during setup, improving the overall robustness of the system. Furthermore, from an eye safety perspective, larger apertures allow the same transmitted power to be spread over a wider area, lowering the power density and making the system safer.

For fiber-based transmitters, the use of adjustable collimators becomes essential to properly account for single mode fiber (SMF) defocus and to mitigate end cap effects. This ensures that the divergence can be turned precisely to the system requirements, increasing reliability and flexibility.

In summary, this work has shown the potential and necessity of a dedicated device for beacon alignment in optical satellite communications. While the prototype already provides accurate and practical tools for measuring divergence and direction, future improvements will make the Test Target more dependable and robust. With these developments, the system can evolve into a versatile tool for ensuring a precise beacon alignment.

## 6 Bibliography

- [1] Sun, N.; Wang, Y.; Wu, Y.; Liu, J. High-Precision Tracking of Free-Space Optical Communication System on Mobile Platforms. *Photonics* 2024, 11, 900. <https://doi.org/10.3390/photonics11100900>
- [2] G. Zhang *et al.*, “A Review of Variable-Beam Divergence Angle FSO Communication Systems,” *Photonics*, vol. 10, no. 7, p. 756, July 2023, doi: 10.3390/photonics10070756.
- [3] A. Carrasco-Casado *et al.*, “Prototype Development and Validation of a Beam-Divergence Control System for Free-Space Laser Communications,” *Front. Phys.*, vol. 10, p. 878488, May 2022, doi: 10.3389/fphy.2022.878488.
- [4] A. Malik and P. Singh, “Free Space Optics: Current Applications and Future Challenges,” *Int. J. Opt.*, vol. 2015, pp. 1–7, 2015, doi: 10.1155/2015/945483.
- [5] H. Kaushal and G. Kaddoum, “Free Space Optical Communication: Challenges and Mitigation Techniques,” June 16, 2015, *arXiv*: arXiv:1506.04836. doi: 10.48550/arXiv.1506.04836.
- [6] “fSONA: Technology.” Available: [http://www.fsona.com/technology.php?sec=fso\\_guide](http://www.fsona.com/technology.php?sec=fso_guide)
- [7] M. N. O. Sadiku, S. M. Musa, and S. R. Nelatury, “Free Space Optical Communications: An Overview,” *Eur. Sci. J. ESJ*, vol. 12, no. 9, p. 55, Mar. 2016, doi: 10.19044/esj.2016.v12n9p55
- [8] “SCaN Glossary - NASA.” Available: <https://www.nasa.gov/reference/scan-glossary/>
- [9] A. Carrasco-Casado and R. Mata Calvo, “Space Optical Links for Communication Networks,” 2020, pp. 1057–1103. doi: 10.1007/978-3-030-16250-4\_34.
- [10] L. Chen *et al.*, “Pointing Acquisition and Tracking System for Free Space Optical Communication Based on Integrated Optical Phased Array,” *IEEE Photonics J.*, vol. 17, no. 4, pp. 1–8, Aug. 2025, doi: 10.1109/JPHOT.2025.3582266.
- [11] R. Paschotta, article on "Collimated Beams" in the RP Photonics Encyclopedia, retrieved 2025-08-25, <https://doi.org/10.61835/0gv>
- [12] C. Fuchs, C. Schmidt, F. Moll, D. Giggenbach, and A. Shrestha, “system aspects of optical LEO-to-ground links,” in *International Conference on Space Optics — ICSO 2016*, N. Karafolas, B. Cugny, and Z. Sodnik, Eds., Biarritz, France: SPIE, Sept. 2017, p. 25. doi: 10.1117/12.2296054.
- [13] J. Kim, “Data Acquisition of Atmospherically Induced Optical Signal Fluctuations,” masters, KIT, 2024.
- [14] J. Bao, S. Wei, J. Lv, and W. Zhang, “Optimized Faster-RCNN in Real-time Facial Expression Classification,” *IOP Conf. Ser. Mater. Sci. Eng.*, vol. 790, p. 012148, Apr. 2020, doi: 10.1088/1757-899X/790/1/012148.
- [15] “Gaussian Beam Propagation.” Accessed: Aug. 25, 2025. [Online]. Available: <https://www.edmundoptics.com/knowledge-center/application-notes/lasers/gaussian-beam-propagation/>
- [16] “Gaussian-Beam-Optics.pdf.” Accessed: Aug. 25, 2025. [Online]. Available: <https://experimentationlab.berkeley.edu/sites/default/files/MOT/Gaussian-Beam-Optics.pdf>
- [17] D. Giggenbach, M. T. Knopp, and C. Fuchs, “Link budget calculation in optical LEO satellite downlinks with on/off-keying and large signal divergence: A simplified methodology,” *Int. J. Satell. Commun. Netw.*, vol. 41, no. 5, pp. 460–476, Sept. 2023, doi: 10.1002/sat.1478.
- [18] Siegman, A. E. (1986). *Lasers*. University Science Books.
- [19] H. Kogelnik and T. Li, “Laser Beams and Resonators,” *Appl. Opt.*, vol. 5, no. 10, pp. 1550–1567, Oct. 1966, doi: 10.1364/AO.5.001550.
- [20] B. E. A. Saleh and M. C. Teich, *Fundamentals of photonics*, Third edition. Hoboken, NJ: Wiley, 2019.
- [21] “Modified Thin-Lens Equation for Laser Light.” Accessed: Aug. 25, 2025. [Online]. Available: <https://www.thorlabs.com>
- [22] P. L. Greene and D. G. Hall, “Focal shift in vector beams,” *Opt. Express*, vol. 4, no. 10, pp. 411–419, May 1999, doi: 10.1364/OE.4.000411.
- [23] “Control Beam Path Through a Corner-Cube Retroreflector.” Accessed: Aug. 25, 2025. [Online]. Available: <https://www.thorlabs.com>
- [24] G. F. Marshall and G. E. Stutz, Eds., *Handbook of Optical and Laser Scanning*. Taylor & Francis, 2012. doi: 10.1201/9781315218243.
- [25] G. Zhang *et al.*, “A Review of Variable-Beam Divergence Angle FSO Communication Systems,” *Photonics*, vol. 10, no. 7, p. 756, July 2023, doi: 10.3390/photonics10070756.
- [26] “Fiber End Caps | Altechna,” Altechna - Custom Laser Optics & Technologies. Accessed: Aug. 25, 2025. [Online]. Available: <https://www.altechna.com/products/fiber-end-caps/fiber-end-caps/>
- [27] “End Caps for single-mode and polarization-maintaining fibers.” Accessed: Aug. 25, 2025. [Online]. Available: <https://www.sukhamburg.com/support/technotes/fiberoptics/cablebasics/endcap.html>
- [28] H. Kaushal, V. Jain, and S. Kar, “Free-Space Optical Channel Models,” 2017, pp. 41–89. doi: 10.1007/978-81-322-3691-7\_2.

- [29] “FPL1009P-SpecSheet.pdf.” Accessed: Aug. 25, 2025. [Online]. Available: <https://www.thorlabs.com/drawings/3d7a96d67087086a-D35FE98B-E37A-6BA2-FA9CD38E724C88E6/FPL1009P-SpecSheet.pdf>
- [30] “Goldeye\_G-130\_VSWIR\_TEC1\_DataSheet\_en.pdf.” Accessed: Aug. 25, 2025. [Online]. Available: [https://cdn.alliedvision.com/fileadmin/pdf/en/Goldeye\\_G-130\\_VSWIR\\_TEC1\\_DataSheet\\_en.pdf](https://cdn.alliedvision.com/fileadmin/pdf/en/Goldeye_G-130_VSWIR_TEC1_DataSheet_en.pdf)
- [31] A. Carrasco-Casado and R. Mata Calvo, *Free-space optical links for space communication networks*. 2020. doi: 10.48550/arXiv.2012.13166.
- [32] “Field of View | MEETOPTICS Academy.” Accessed: Aug. 25, 2025. [Online]. Available: <https://www.meetoptics.com/academy/field-of-view#using-wd-and-fov-to-determine-focal-length>
- [33] “Chromatic and Monochromatic Optical Aberrations.” Accessed: Aug. 25, 2025. [Online]. Available: <https://www.edmundoptics.com/Knowledge-Center/application-notes/optics/chromatic-and-monochromatic-optical-aberrations/>
- [34] “Thorlabs - FBH1550-30 Hard-Coated Bandpass Filter, Ø25 mm, CWL = 1550 nm, FWHM = 30 nm.” Available: <https://www.thorlabs.com>
- [35] “Adjustable Focus Reflective Collimators, Protected Silver Coating.” Accessed: Aug. 25, 2025. [Online]. Available: <https://www.thorlabs.com>
- [36] “PDA20CS2-Manual.pdf.” Accessed: Aug. 25, 2025. [Online]. Available: <https://www.thorlabs.com/drawings/3d7a96d67087086a-D35FE98B-E37A-6BA2-FA9CD38E724C88E6/PDA20CS2-Manual.pdf>
- [37] “2. Technologies | Avery Dennison.” Accessed: Aug. 25, 2025. [Online]. Available: <https://label.averydennison.com>
- [38] “astm-d4956-04-standard-specification.pdf.” Accessed: Aug. 25, 2025. [Online]. Available: <https://multimedia.3m.com/mws/media/315459O/astm-d4956-04-standard-specification.pdf>
- [39] “MCC E-1608: Multifunction Ethernet DAQ Device - Digilent.” Accessed: Aug. 25, 2025. [Online]. Available: [https://diligent.com/shop/mcc-e-1608-multifunction-ethernet-daq-device/?srsltid=AfmBOorOMB7iz5YXrpe4S7ZVK\\_1Xg4hyomkWSH-EIvNzQ4-5GGTuDLII](https://diligent.com/shop/mcc-e-1608-multifunction-ethernet-daq-device/?srsltid=AfmBOorOMB7iz5YXrpe4S7ZVK_1Xg4hyomkWSH-EIvNzQ4-5GGTuDLII)
- [40] “PowerBeam\_AC\_Gen2\_DS.pdf.” Accessed: Aug. 25, 2025. [Online]. Available: [https://dl.ubnt.com/datasheets/PowerBeam\\_ac/PowerBeam\\_AC\\_Gen2\\_DS.pdf](https://dl.ubnt.com/datasheets/PowerBeam_ac/PowerBeam_AC_Gen2_DS.pdf)
- [41] “DAQami-data.pdf.” Accessed: Aug. 25, 2025. [Online]. Available: <https://files.digilent.com/datasheets/DAQami-data.pdf>
- [42] “About Vimba X — Vimba X Developer Guide 2025-2 documentation.” Accessed: Aug. 25, 2025. [Online]. Available: [https://docs.alliedvision.com/Vimba\\_X/Vimba\\_X\\_DeveloperGuide/about.html](https://docs.alliedvision.com/Vimba_X/Vimba_X_DeveloperGuide/about.html)
- [43] “Speckle imaging,” *Wikipedia*. Aug. 11, 2025. Accessed: Aug. 25, 2025. [Online]. Available: [https://en.wikipedia.org/w/index.php?title=Speckle\\_imaging&oldid=1305277757](https://en.wikipedia.org/w/index.php?title=Speckle_imaging&oldid=1305277757)
- [44] V. Kornilov, “Stellar scintillation in the short exposure regime and atmospheric coherence time evaluation,” *Astron. Astrophys.*, vol. 530, p. A56, June 2011, doi: 10.1051/0004-6361/201116553.
- [45] “Viewer Guide — Vimba X Developer Guide 2025-2 documentation.” Accessed: Aug. 25, 2025. [Online]. Available: [https://docs.alliedvision.com/Vimba\\_X/Vimba\\_X\\_DeveloperGuide/viewerGuide.html](https://docs.alliedvision.com/Vimba_X/Vimba_X_DeveloperGuide/viewerGuide.html)
- [46] D. T. Wayne, R. L. Phillips, L. C. Andrews, and B. Griffis, “Beam wander of a collimated beam: comparing theory and experiment,” in *Free-Space Laser Communications VIII*, SPIE, Aug. 2008, pp. 210–220. doi: 10.1117/12.796503.
- [47] S. M. Augustine and N. Chetty, “Experimental verification of the turbulent effects on laser beam propagation in space,” *Atmósfera*, vol. 27, no. 4, pp. 385–401, Oct. 2014, doi: 10.1016/S0187-6236(14)70037-2.
- [48] A. V. Arecchi, T. Messadi, and R. J. Koshel, *Field Guide to Illumination*, SPIE Press, Bellingham, WA (2007)
- [49] Sidney A. Self, “Focusing of spherical Gaussian beams,” *Appl. Opt.* 22, 658-661 (1983).
- [50] Giggenbach, Dirk and Fuchs, Christian and Schmidt, Christopher and Rödiger, Benjamin and Gaißer, Steffen and Klinkner, Sabine and Phung, Duy-Ha and Chabé, Julien and Courde, Clément and Maurice, Nicolas and Mariey, Hervé and Samain, Etienne and Artaud, Géraldine (2022) Downlink communication experiments with OSIRISv1 laser terminal onboard Flying Laptop satellite. *Applied Optics*, 61 (8), pp. 1938-1946. Optical Society of America. doi: 10.1364/AO.446771
- [51] Giggenbach, Dirk and Karafillis, Petro and Rittershofer, Jonas and Immerz, Andreas and Spörl, Andreas and Gaisser, Steffen and Klinkner, Sabine and Knopp, Marcus Thomas (2022) Transmitter Beam Bias Verification for Optical Satellite Data Downlinks with Open-Loop Pointing – the 3-OGS-Experiment. In: 2022 International Conference on Space Optics, ICSO 2022. International Conference on Space Optics (ICSO), 2022-10-02 - 2022-10-07, Dubrovnik, Kroatien. doi: 10.1117/12.2689023
- [52] Dong He, Qiang Wang, Jian-Wei Zhou, Zhi-Jun Song, Dai-Jun Zhong, Yu Jiang, Wan-Sheng Liu, Yong-Mei Huang, “A method for optical ground station reduce alignment error in satellite-ground quantum experiments,” *Proc. SPIE* 10710, Young Scientists Forum 2017, 1071004 (5 March 2018); <https://doi.org/10.1117/12.2306707>
- [53] Vincent W. S. Chan, “Free-Space Optical Communications,” *J. Lightwave Technol.* 24, 4750-4762 (2006)

- [54] Knopp, Marcus Thomas and Immerz, Andreas and Giggenbach, Dirk and Köhler, Alexander (2022) The Small Optical Ground Stations Focal-Optics Assembly (SOFA). In: 73rd International Astronautical Congress, IAC 2022. 73rd International Astronautical Congress (IAC), 2022-09-18 - 2022-09-22, Paris, Frankreich. ISSN 0074-1795.
- [55] Aldasoro Marculeta, Iker (2024) AllSky-Camera system for Monitoring of Optical Satellite Downlinks. Bachelor's, Universidad Publica de Navarra.
- [56] Giggenbach, Dirk and Moll, Florian and Schmidt, Christopher and Fuchs, Christian and Shrestha, Amita (2018) Optical on-off keying data links for low Earth orbit downlink applications. In: Satellite Communications in the 5G Era IET TELECOMMUNICATIONS SERIES, 79. The Institution of Engineering and Technology. pp. 307-339. doi: 10.1049/PBTE079E\_ch11
- [57] Giggenbach, Dirk (2017) Signal Control in Optical Ground-to-Space Links. P 9
- [58] Mata Calvo, Ramon and Becker, Peter and Giggenbach, Dirk and Moll, Florian and Schwarzer, Malte and Hinz, Martin and Sodnik, Zoran (2014) Transmitter diversity verification on ARTEMIS geostationary satellite. In: Photonics West Conference (ISSN: 1062-3701), 8971 (4), pp. 897104-1. SPIE. SPIE Photonics West 2014, 2014-02-02 - 2014-02-04, San Francisco, USA. doi: 10.1117/12.2036554
- [59] Giggenbach, Dirk (2014) Optical Free Space Links for Satellite-Ground Communications. ASMS/SPSC, 2014-09-08, Livorno.
- [60] Rödiger, Benjamin and Rüddenklau, René and Morab Vishwanath, Anil and Roubal, Christian and Moll, Florian and Fuchs, Christian (2024) Verification of laser communication terminals for CubeSats as preparation for missions PIXL-1 and QUBE under atmospheric conditions. In: 75th International Astronautical Congress, IAC 2024. 75th International Astronautical Congress (IAC), 2024-10-14 - 2024-10-18, Miland, Italien. ISSN 0074-1795.
- [61] R. Paschotta, article on "Core-less End Caps" in the RP Photonics Encyclopedia, retrieved 2025-08-25, <https://doi.org/10.61835/ooh>
- [62] R. Paschotta, article on "Fibers" in the RP Photonics Encyclopedia, retrieved 2025-08-25, <https://doi.org/10.61835/11k>
- [63] Khaled Jum'ah, Katarzyna Kamieniecka, Krzysztof Poterlowicz, Working with Beacon V2: A Comprehensive Guide to Creating, Uploading, and Searching for Variants with Beacons (Galaxy Training Materials). [https://training.galaxyproject.org/training-material/topics/variant-analysis/tutorials/beaconise\\_1000hg/tutorial.html](https://training.galaxyproject.org/training-material/topics/variant-analysis/tutorials/beaconise_1000hg/tutorial.html) Online; accessed Mon Aug 25 2025
- [64] René Rüddenklau, Fabian Rein, Christian Roubal, Benjamin Rödiger, and Christopher Schmidt, "In-orbit demonstration of acquisition and tracking on OSIRIS4CubeSat," Opt. Express 32, 41188-41200 (2024)
- [65] A. Carrasco-Casado, K. Shiratama, D. Kolev, F. Ono, H. Tsuji, and M. Toyoshima, "Miniaturized Multi-Platform Free-Space Laser-Communication Terminals for Beyond-5G Networks and Space Applications," Photonics, vol. 11, no. 6, p. 545, June 2024, doi: 10.3390/photonics11060545.
- [66] C. Fuchs, D. Giggenbach, R. M. Calvo and W. Rosenkranz, "Transmitter Diversity With Phase-Division Applied to Optical GEO Feeder Links," in IEEE Photonics Technology Letters, vol. 33, no. 11, pp. 541-544, 1 June1, 2021, doi: 10.1109/LPT.2021.3073959.
- [67] Shreya S. Patil, Chinchu Joseph, D. T. Varpe, & A. A. Bazil Raj. (2024). A Comprehensive Review on Security in Free-Space Optical Communication. International Journal of Engineering Research and Reviews, 12(3), 150–180.
- [68] H. Singh, R. Miglani, N. Mittal, G. S. Gaba, M. Masud, and S. Aljahdali, "Design and Analysis of Commercially Viable Free-Space Optical Communication Link for Diverse Beam Divergence Profiles," Front. Phys., vol. 9, Dec. 2021, doi: 10.3389/fphy.2021.778734.
- [69] Tzung-Hsien Ho, Stuart D. Milner, Christopher C. Davis, "Fully optical real-time pointing, acquisition, and tracking system for free space optical link," Proc. SPIE 5712, Free-Space Laser Communication Technologies XVII, (18 April 2005); <https://doi.org/10.1117/12.590982>
- [70] Lavrinov, D. Handbook of Optical and Laser Scanning.
- [71] Wu, J., Zhang, Y., Li, Q., Yu, S., & Yu, J. (2025). Performance Analysis of Space-to-Ground Downlink for Polarization Shift Keying Optical Communications with a Gaussian-Schell Model Beam. Photonics, 12(7), 643. <https://doi.org/10.3390/photonics12070643>

## 7 Annex 1 (Camera interface scripts)

Main.py: all the image acquisition and processing are done via the vmbpy library in this script.

```
import sys
from typing import Optional
from queue import Queue
from vmbpy import *
import cv2
import numpy as np
from collections import deque
import time
from skimage import measure, filters
from scipy.interpolate import interp1d
# All frames will either be recorded in this format, or transformed to it before being displayed
opencv_display_format = PixelFormat.Bgr8
def get_camera(camera_id: Optional[str]) -> Camera: # Camera connection
    with VmbSystem.get_instance() as vmb:
        if camera_id:
            try:
                return vmb.get_camera_by_id(camera_id)
            except VmbCameraError:
                print('Failed to access Camera \'{ }\'. Abort.'.format(camera_id))
        else:
            cams = vmb.get_all_cameras()
            if not cams:
                print('No Cameras accessible. Abort.')
            return cams[0]
def setup_camera(cam: Camera): # Default settings
    with cam: # Enable auto exposure time setting if camera supports it
        try:
            cam.ExposureAuto.set('Off') # To be able to set the exposure manually
            cam.ExposureTime.set(1000)
        except (AttributeError, VmbFeatureError):
            pass
        try: # Enable white balancing if camera supports it
            cam.BalanceWhiteAuto.set('Continuous')
        except (AttributeError, VmbFeatureError):
            pass
        try: # Try to adjust GeV packet size. This Feature is only available for GigE - Cameras
            stream = cam.get_streams()[0]
            stream.GVSPAdjustPacketSize.run()
            while not stream.GVSPAdjustPacketSize.is_done():
                pass
        except (AttributeError, VmbFeatureError):
            pass
def setup_pixel_format(cam: Camera):
    try: # Set a 12 bit (max) pixel format if possible
        cam.set_pixel_format(PixelFormat.Mono12)
        print("Using Mono12 format.")
```

```

except VmbFeatureError:
    print('Camera does not support Mono12. Abort.')
class Handler:
    def __init__(self): # Define buffer and global variables
        self.display_queue = Queue(1)
        self.frame_buffer = deque(maxlen=20)
        self.divL = 0
        self.divR = 0
    def __call__(self, cam: Camera, stream: Stream, frame: Frame):
        if frame.get_status() == FrameStatus.Complete:
            if frame.get_pixel_format() == PixelFormat.Mono12:
                width = frame.get_width()
                height = frame.get_height()
                buffer = frame.get_buffer()
                # Reed image of 12 bits (16 bits unsigned)
                img_12bit = np.frombuffer(buffer, dtype=np.uint16).reshape((height, width))
                self.frame_buffer.append(img_12bit.copy())
                # Convert to 8 bits (Mono8) for representation
                img_8bit = (img_12bit / 16).astype(np.uint8)
                # Convert to BGR for OpenCV GUI
                img = cv2.cvtColor(img_8bit, cv2.COLOR_GRAY2BGR)
            else: # Other formats
                if frame.get_pixel_format() != opencv_display_format:
                    display = frame.convert_pixel_format(opencv_display_format)
                else:
                    display = frame
                img = display.as_opencv_image()
                self.frame_buffer.append(cv2.cvtColor(img, cv2.COLOR_BGR2GRAY).astype(np.uint16))
            mean_img = None
            divL, divR = None, None
            if len(self.frame_buffer) == 20: # If buffer is full, calculate divergences
                mean_img, divL, divR = self.compute_mean()
                self.divL = divL
                self.divR = divR
            else:
                mean_img = None
                self.divL = 0
                self.divR = 0
            # Detect saturated pixels for irt visualization
            saturated_mask = (img[:, :, 0] == 255) & (img[:, :, 1] == 255) & (img[:, :, 2] == 255)
            img[saturated_mask] = [0, 0, 255]
            processed = img
            if not self.display_queue.full():
                self.display_queue.put_nowait((processed, mean_img, divL, divR))
            else:
                try:
                    self.display_queue.get_nowait()
                except:
                    pass

```

```

        self.display_queue.put_nowait((processed, mean_img, divL, divR))
    cam.queue_frame(frame)
def compute_mean(self): # Image processing
    stacked = np.stack(self.frame_buffer).astype(np.float32)
    mean_img = np.mean(stacked, axis=0).astype(np.uint16)
    thresh = filters.threshold_otsu(mean_img)
    mask = (mean_img > thresh).astype(np.uint8)
    labels = measure.label(mask)
    props = measure.regionprops(labels)
    valid_props = []
    for prop in props:
        if prop.area < 20:
            continue # Too small
        if prop.eccentricity > 0.8:
            continue # Not circular (0 = circular, 1 = rectangular)
        # Check for saturation in region
        minr, minc, maxr, maxc = prop.bbox
        roi = mean_img[minr:maxr, minc:maxc]
        if np.any(roi == 4095): # saturated pixels in 12bit change if needed
            continue
        valid_props.append(prop)
    # Find shape contours
    contours, _ = cv2.findContours(mask.astype(np.uint8), cv2.RETR_EXTERNAL,
cv2.CHAIN_APPROX_SIMPLE)
    props_sorted = sorted(valid_props, key=lambda p: p.area, reverse=True)
    if len(props_sorted) < 2:
        img_8bit = (mean_img / 16).astype(np.uint8)
        mean_bgr = cv2.cvtColor(img_8bit, cv2.COLOR_GRAY2BGR)
        return mean_bgr, None, None
    centros = [prop.centroid for prop in props_sorted[:2]]
    centros = sorted(centros, key=lambda c: c[1]) # Sort by x
    centroL = centros[0]
    centroR = centros[1]
    xL = round(centroL[1])
    xR = round(centroR[1])
    intensityYL = mean_img[:, xL]
    intensityYR = mean_img[:, xR]
    intensityYL_norm = intensityYL / intensityYL.max()
    halfMax = 0.5
    pixel_size_irl = (0.005 / 200) * 350 # m for pixel
    dist = 350 # m
    # New x axis for interpolation
    x_newL = np.arange(intensityYL.size) * pixel_size_irl
    x_newR = np.arange(intensityYR.size) * pixel_size_irl
    # Interpolation
    fL = interp1d(x_newL, intensityYL, kind='linear')
    fR = interp1d(x_newR, intensityYR, kind='linear')
    x_denseL = np.linspace(x_newL.min(), x_newL.max(), 4*len(x_newL))
    x_denseR = np.linspace(x_newR.min(), x_newR.max(), 4*len(x_newR))

```

```

y_denseL = fL(x_denseL)
y_denseR = fR(x_denseR)
y_dense_normL = y_denseL/y_denseL.max()
y_dense_normR = y_denseR/y_denseR.max()
indexL = np.where(y_dense_normL >= halfMax)[0]
indexR = np.where(y_dense_normR >= halfMax)[0]
if len(indexL) < 2 or len(indexR) < 2:
    print("We couldn't get the 2 cuts well for divergence calculation")
    img_8bit = (mean_img / 16).astype(np.uint8)
    mean_bgr = cv2.cvtColor(img_8bit, cv2.COLOR_GRAY2BGR)
    maskbgr = cv2.cvtColor(mask.astype(np.uint8) * 255, cv2.COLOR_GRAY2BGR)
    return mean_bgr, None, None
x = np.arange(len(intensityYL_norm))
FWHML = x_denseL[indexL[-1]] - x_denseL[indexL[0]]
FWHMR = x_denseR[indexR[-1]] - x_denseR[indexR[0]]
divL = FWHML / dist * 1000 # mrad
divR = FWHMR / dist * 1000 # mrad
img_8bit = (mean_img / 16).astype(np.uint8)
mean_bgr = cv2.cvtColor(img_8bit, cv2.COLOR_GRAY2BGR)
# Draw contours and centers on mean image
for (y, x) in centros:
    cv2.circle(mean_bgr, (int(round(x)), int(round(y))), radius=5, color=(255, 0, 0),
thickness=2)
cv2.drawContours(mean_bgr, contours, -1, (0, 0, 255), 2)
for prop in valid_props:
    y, x = prop.centroid
    cv2.circle(mean_bgr, (int(round(x)), int(round(y))), 5, (0, 255, 0), 2)
for (y, x) in centros:
    cv2.circle(mean_bgr, (int(round(x)), int(round(y))), radius=5, color=(255, 0, 0),
thickness=2)

    return mean_bgr, divL, divR
def get_images(self):
    try:
        img, mean, divL, divR = self.display_queue.get_nowait()
        return img, mean, divL, divR
    except:
        return None, None, None, None
class CameraStream:
    def __init__(self, camera_id: Optional[str] = None):
        self.camera_id = camera_id
        self.cam = None
        self.handler = Handler()
        self.running = False
    def set_exposure(self, value: int):
        if self.cam:
            try:
                self.cam.ExposureAuto.set('Off')
                self.cam.ExposureTime.set(value)
            except Exception as e:

```

```

        print(f"Error setting exposure: {e}")
def start(self):
    with VmbSystem.get_instance():
        with get_camera(self.camera_id) as cam:
            self.cam = cam
            setup_camera(cam)
            setup_pixel_format(cam)
            cam.start_streaming(handler=self.handler, buffer_count=10)
            self.running = True
            try:
                while self.running:
                    time.sleep(0.01) # Evita consumir CPU
            finally:
                cam.stop_streaming()
def stop(self):
    self.running = False
def get_exposure(self) -> int:
    if self.cam:
        try:
            return int(self.cam.ExposureTime.get())
        except Exception as e:
            print(f"Error reading exposure: {e}")
    return -1

```

GUI.py: script that controls the interface updates and data visualization.

```

import tkinter as tk
from tkinter import ttk
from PIL import Image, ImageTk
import threading
import cv2
from Main import CameraStream
class App:
    def __init__(self, root): # Construction of the interface
        self.root = root
        self.root.title("GoldenEye Camera Viewer")
        self.default_font = ("Helvetica", 20)
        # Top part: 2 horizontal labels for the images
        self.label_frame = ttk.Frame(root)
        self.label_frame.pack()
        self.label1 = ttk.Label(self.label_frame)
        self.label1.pack(side=tk.LEFT)
        self.label2 = ttk.Label(self.label_frame)
        self.label2.pack(side=tk.LEFT)
        # Exposure slider
        self.exposure_slider = tk.Scale(
            self.root,
            from_=18,
            to=100000,

```

```

        orient=tk.HORIZONTAL,
        label="Exposure",
        length=500,
        command=self.on_slider_change,
        font=("Helvetica", 14)
    )
    self.exposure_slider.set(1000)
    self.exposure_slider.pack(pady=10)
    # Frame for input + button
    entry_frame = ttk.Frame(self.root)
    entry_frame.pack(pady=5)
    # Manual input section
    self.exposure_entry = ttk.Entry(entry_frame, width=10, font=("Helvetica", 14) )
    self.exposure_entry.insert(0, "100000")
    self.exposure_entry.pack(side=tk.LEFT, padx=5)
    # Button to apply change
    style = ttk.Style()
    style.configure("Big.TButton", font=("Helvetica", 14))
    apply_button = ttk.Button(entry_frame, text="Apply",
command=self.apply_exposure_entry, style="Big.TButton")
    apply_button.pack(side=tk.LEFT, padx=5)
    # Frame for divergencia
    div_frame = ttk.Frame(self.root)
    div_frame.pack(pady=5)
    # Add divergence labels
    self.div_label = ttk.Label(div_frame, text="Left divergence: -- mrad", font=self.default_font)
    self.div_label.pack(side=tk.LEFT, pady=5)
    self.div2_label = ttk.Label(div_frame, text="Right divergence: -- mrad",
font=self.default_font)
    self.div2_label.pack(side=tk.LEFT, pady=5)
    self.camera = CameraStream() # Camara
    self.handler = self.camera.handler
    self.running = True
    self.stream_thread = threading.Thread(target=self.stream_loop) # Initialize stream
    self.stream_thread.daemon = True
    self.stream_thread.start()
    self.update_image() # Update section
    self.root.protocol("WM_DELETE_WINDOW", self.on_close)
def on_slider_change(self, val):
    try:
        val = int(float(val))
        self.camera.set_exposure(val)
        self.exposure_entry.delete(0, tk.END)
        self.exposure_entry.insert(0, str(val))
    except Exception as e:
        print(f"Error when changing the exposure: {e}")
def stream_loop(self):
    self.camera.start()
    self.camera.stop()

```

```

def update_image(self):
    live_img, mean_img, divL, divR = self.handler.get_images() # Data acquisition from the api
    if live_img is not None:
        image = cv2.cvtColor(live_img, cv2.COLOR_BGR2RGB)
        h, w = image.shape[:2]
        cropped = image[200:h-200, 200:w-200]
        image = self.resize_image(cropped)
        photo = ImageTk.PhotoImage(Image.fromarray(image))
        self.label1.imgtk = photo
        self.label1.config(image=photo)
    if mean_img is not None:
        image = cv2.cvtColor(mean_img, cv2.COLOR_BGR2RGB)
        h, w = image.shape[:2]
        cropped = image[200:h-200, 200:w-200]
        image = self.resize_image(cropped)
        photo = ImageTk.PhotoImage(Image.fromarray(image))
        self.label2.imgtk = photo
        self.label2.config(image=photo)
    if divL is not None:
        self.div_label.config(text=f"Left divergence: {divL:.2f} mrad")
    if divR is not None:
        self.div2_label.config(text=f"Right divergence: {divR:.2f} mrad")
    if self.running:
        self.root.after(33, self.update_image)
def resize_image(self, image, max_width=800, max_height=600): # Zoom for better visualization
    height, width, _ = image.shape
    scale = min(max_width / width, max_height / height)
    if scale < 1.0:
        new_size = (int(width * scale), int(height * scale))
        image = cv2.resize(image, new_size, interpolation=cv2.INTER_AREA)
    return image
def apply_exposure_entry(self):
    try:
        val = int(self.exposure_entry.get())
        val = max(1, min(1000000, val)) # Clamp the value
        self.camera.set_exposure(val)
        self.exposure_slider.set(val)
    except Exception as e:
        print(f"Error applying the exposure from manual input: {e}")
def on_close(self):
    self.running = False
    self.root.quit()
if __name__ == '__main__':
    root = tk.Tk()
    app = App(root)
    root.mainloop()

```

## 8 Annex 2 (Radio frequency link setup)

The objective of this annex is to explain the configuration of the link between the DAQ that receives photodetectors signals and a laptop that processes said signals. The components are necessary for the link to work:

- Two Airmax Powerbeam 5ac gen2 (one for the Access Point and one for the Station)
- A Multifunction Ethernet DAQ Device (MCC E-1608)
- A notebook
- Three cables that support PoE
- Power supply

The overview of the final setup is shown in Figure 65 where the network is 192.168.0.0/24 due to the DAQ's default IP address (192.168.0.101).

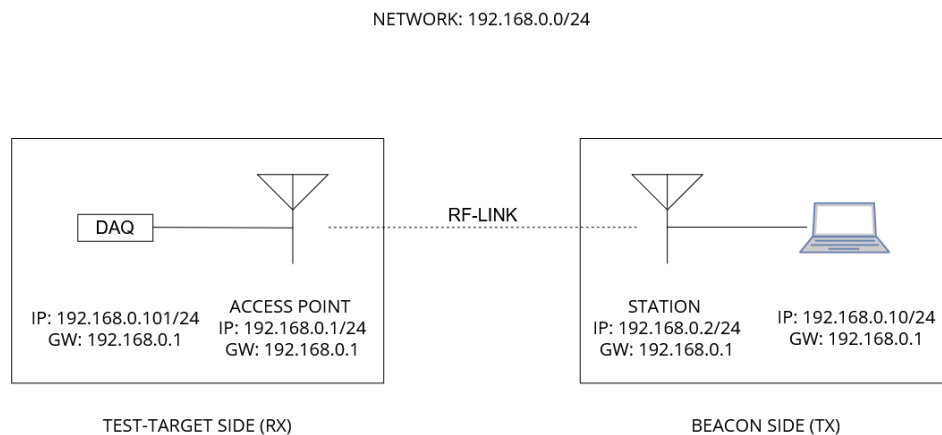


Figure 62: Final setup

### 8.1 Power beams

For the connection, two power beams will be needed to create a bridge between the computer and the DAQ. One of them will be at the “server’s” end (the DAQ in our case, it will be the one replying to the notebooks requests) and will be configured as an Access Point. The other one will be at the client’s end (the notebook in our case, it will be the one making the requests to the DAQ) and will be configured as a Station.

#### 8.1.1 Access Point

Configuration process:

1. If the power beam is already configured, restart it.
2. Connect the power beam to the PoE outlet in the Gigabit PoE.
3. Connect the Gigabit PoE to a power source. The power beam’s power LED must be on.
4. Connect the notebook to the LAN outlet in the Gigabit PoE.

5. In the notebook, change the Ethernet channel's IP address to the one in range with the power beam's default IP address (192.168.1.20). In our case the 192.168.1.50.

Go to Control Panel > Network and Internet > Network and sharing center > change adapter settings (left column) > Ethernet Properties > Internet protocol v4 > use the following IP address and change the IP to 192.168.1.50 (Figure 66).

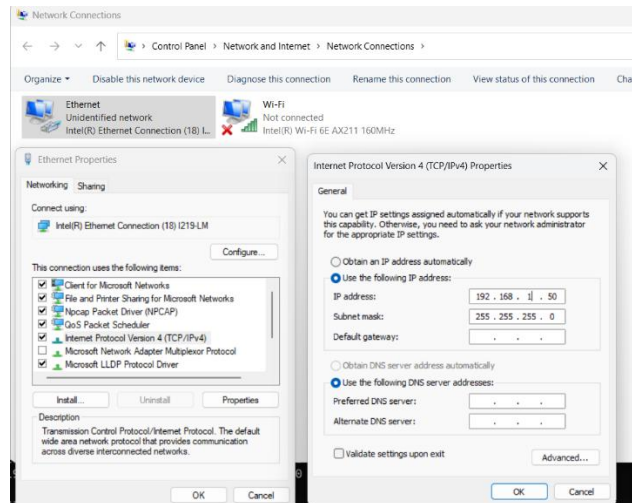


Figure 63: Ip change

6. In the notebook, open the cmd and with the command `arp -a`. The IP of all the devices connected to the notebook can be seen. Check if the power beam's default IP address appears (192.168.1.20) or if it can be reached by ping. If not, it can be a sign that the power beam is already configured, so restart it.
7. In the notebook, go to a browser and type the default IP address (192.168.1.20). A portal should appear. Configure the country, language and create an account to configurate the power beam. After entering, another portal should initialize in the URL 192.168.1.20/#dashboard (Figure 67).

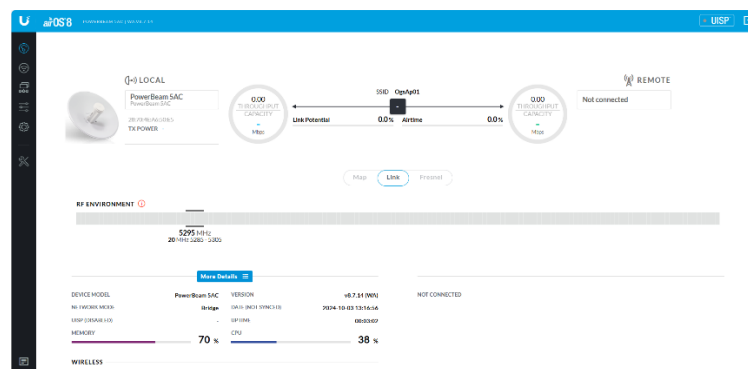


Figure 64: Starting portal

8. In the wireless page, select the ACCESS POINT icon, the PTP mode, the desired central frequency (5745 MHz, in our case) and change the SSID to something recognizable: OgsAp01. For the test period, the OUTPUT POWER can be lowered to the minimum.

Figure 65: Access Point's wireless configuration

9. In the network page, select the NETWORK MODE to bridge and in the Management Network Settings do the following: change the MANAGEMENT IP ADDRESS to Static and configure the IP ADDRESS to 192.168.0.1, NETMASK 255.255.255.0 and GATEWAY IP to 192.168.0.1. The GATEWAY IP can be left blank but an IP was assigned just in case.

Figure 66: Access Point's network configuration

10. Save the changes and they will be applied automatically.
11. Now that the power beam's IP (new IP: 192.168.0.1) has been changed, the site won't be accessible anymore. Change the notebook's IP to a new one in the same range (192.168.0.50 in our case) and go to the cmd. Try pinging the new IP or using `arp -a` to see the new IP and confirm the IP change has been made.

```
C:\Users\ogste>ping 192.168.0.1

Pinging 192.168.0.1 with 32 bytes of data:
Reply from 192.168.0.1: bytes=32 time<1ms TTL=64
Reply from 192.168.0.1: bytes=32 time=1ms TTL=64
Reply from 192.168.0.1: bytes=32 time=1ms TTL=64
Reply from 192.168.0.1: bytes=32 time=1ms TTL=64

Ping statistics for 192.168.0.1:
    Packets: Sent = 4, Received = 4, Lost = 0 (0% loss),
    Approximate round trip times in milli-seconds:
        Minimum = 0ms, Maximum = 1ms, Average = 0ms
```

Figure 67: Access Point's configuration's verifying ping

If do additional configurations are wanted, the new address can be used as a way to enter the configuration page, and the user and password are the ones selected in the starting configuration (Step 7).

To configure the Station Powerbeam, the disconnection of the notebook's ethernet port will be needed but the Access Point power beam should remain powered on.

### 8.1.2 Station

For the Station Powerbeam, the process is quite similar. Follow the same steps as the Access Point Powerbeam until Step 8, to the configuration interface.

1. In the wireless page, do not select the ACCESS POINT option and just select the PTP option. If one is in the test period, it can lower the OUTPUT POWER to a minimum. Ignore the SSID for now.

Figure 68: Station's wireless configuration

2. In the network page, select the NETWORK MODE to bridge and in the Management Network Settings do the following: change the MANAGEMENT IP ADDRESS to Static and configure the IP ADDRESS to 192.168.0.2, NETMASK 255.255.255.0 and GATEWAY IP to 192.168.0.1. The GATEWAY IP can be left blank but an IP was assigned just in case.

Figure 69: Station's network configuration

- Save the changes and they will be applied automatically.
- Now that the Power beams IP (new IP: 192.168.0.2) has been changed, the site won't be accessible anymore. Change the notebook's IP to a new one in the same range (192.168.0.50 in our case) and go to the cmd. Try pinging the new IP or using `arp -a` to see the new IP and confirm the IP change has been made.

```
Pinging 192.168.0.2 with 32 bytes of data:
Reply from 192.168.0.2: bytes=32 time=1ms TTL=64
Reply from 192.168.0.2: bytes=32 time=1ms TTL=64
Reply from 192.168.0.2: bytes=32 time=1ms TTL=64
Reply from 192.168.0.2: bytes=32 time=1ms TTL=64

Ping statistics for 192.168.0.2:
    Packets: Sent = 4, Received = 4, Lost = 0 (0% loss),
    Approximate round trip times in milli-seconds:
        Minimum = 1ms, Maximum = 1ms, Average = 1ms
```

Figure 70: Station's configuration's verifying ping

- For the last step, the two antennas must sync using the same SSID. Please note that the Access Point antenna should be on and the one connected to the notebook is still the Station antenna. Go to the configuration page using the notebook's browser and the Station's new IP address (192.168.0.2). In the wireless page, click the SELECT button below SSID and select the option with the name that was previously assigned in the Access Point's configuration (OgsAp01, Figure 72). Click on the *lock on to* option and, in the starting page, a stablished connection must be seen between the two antennas (Figure 74).

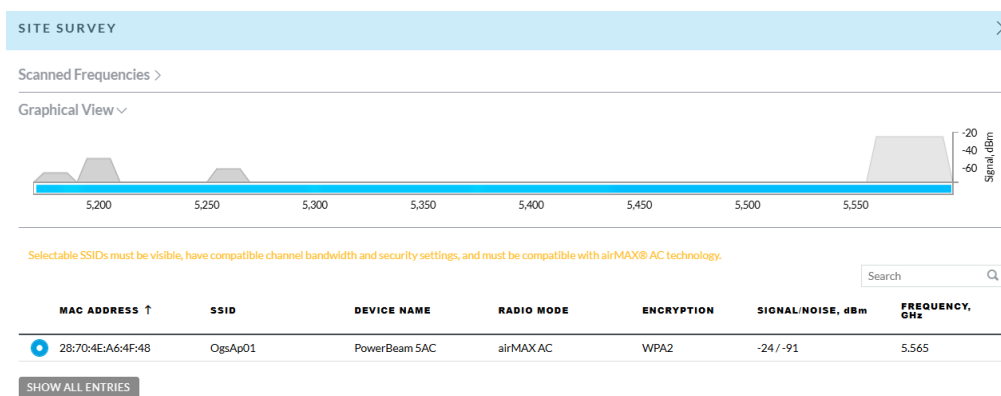


Figure 71: SSID options in the Station antenna 's wireless configuration

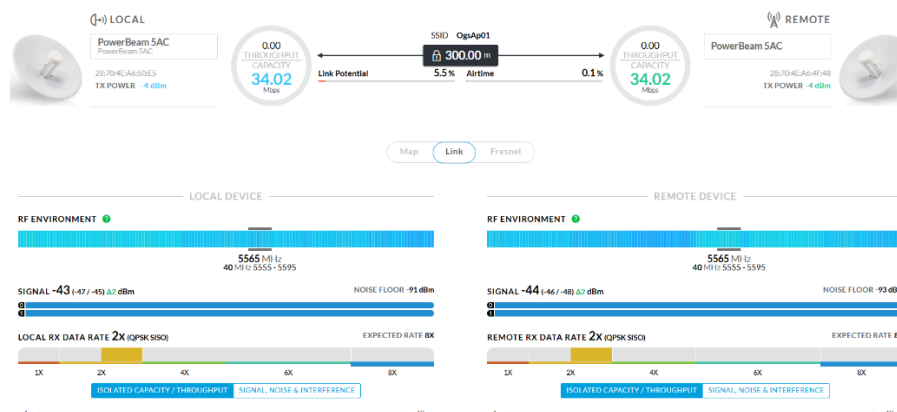


Figure 72: Starting portal where the connection can be seen

## 8.2 MCC DAQ

As it is mentioned in the User's Guide, when connecting the E-1608-OEM for the first time, make sure that DHCP is enabled in the network. It also states that if there are uncertainties in the network DHCP service, the device can be directly connected to the notebook for the configuration. In this case, the device should use the default IP (192.168.0.101), mask (255.255.255.0) and gateway (192.168.0.1).

To make sure the setup is correct, plug the DAQ to a notebook and use the *arp -a* command or a ping to see if the connection has been established. If it has not, restart the DAQ and try again. If there is still no connection with the 192.168.0.101 IP address, which has been our case, continue the following way.

For the proper IP configuration, the *Instacal* program mentioned in the DAQ's User's Guide is needed. Before doing any of the steps, install said program. In this section WIFI access and the MAC address will be necessary. The device's MAC address can be found on the backside of the DAQ.

First, the communication that is going on between the DAQ and the notebook should be understood, if there is any. Skip this paragraph to go straight to configuration. Use a network traffic analyzer like Wireshark and record the information that is being sent and received in the ethernet port when the DAQ is restarted or plug. When the DAQ restarts, there is an ARP message that has the DAQ's default IP as the source. After that, the DAQ sends a few Gratuituity messages announcing a random IP (detect them by the source's MAC address). Finally, it starts sending DHCP Discover messages nonstop so that it can get assigned an IP address. With this, that the DAQ actually needs a DHCP enabled network on its first use can be concluded.

To solve the problem, our notebook's WIFI connection was used. This are the steps:

Firstly, check the IP of the connections already established using the WIFI and the ethernet connection of the notebook. Connect to a WIFI network and then go to the cmd to use the *arp -a* command to print a log that will be used afterwards. Two sections will be seen on the response, one with the *Interface: IP that you assigned to the ethernet port* and the other one, *Interface: random IP that was assigned to you by the WIFI network*. Focus on the WIFI section. Don't close the cmd window and continue.

All the devices connected to the computer to be able to connect to the WIFI via the notebook. For that, go to Control Panel > Network and Internet > Network and sharing center > change adapter settings (left column) > Wi-Fi properties > Sharing and allow other network users to connect through this computer's Internet connection.

The DAQ will connect to the WIFI and the WIFI will assign a new IP to the DAQ. Check the new IP doing the *arp -a* in the cmd and looking at the new IP address that has appeared on the WIFI section.

Now, open *Instacal* and add the DAQ with the new IP address to the board. That has to be made using the *new board* option and in the ENET window, selecting the manual option and entering the DAQ's MAC address manually. After adding it and seeing the device pop on the screen with a MAC address, use the *Instacal Configure* button to configure the devices IP address to the one needed. Select the static option instead of the dynamic option that was selected by default and, in the following section, write the designated IP mask and gateway (192.168.0.101, 255.255.255.0 and 192.168.0.1).

Accepting the change will automatically change the DAQ's IP address. Ping the new address, making sure that the notebook's ethernet port's IP address is in the same range (192.168.0.50 for example).

### 8.3 Final setup

After assigning the correct IP address to each of the elements, the whole network can be set up:

- Connect the Access Point antenna to the PoE port in the Gigabit PoE.
- Connect the LAN port of the same Gigabit PoE to the DAQ.
- Connect the DAQ and the Gigabit PoE to a power source.
  
- Connect the Station antenna to the PoE port in the Gigabit PoE.
- Connect the Lan port of the same Gigabit PoE to the notebook.
- Connect the Gigabit PoE to a power source.

After connecting all the elements, observe the power LED, ethernet LED and the Signal strength LEDs light up both in the Access Point and the Station antennas. Look at the DAQ's power led and Link/Activity LED light up. If all the LED's are on, try pinging all the elements from the computer. If the ping is correct, the link has been established correctly (Figure 76).

```
C:\Users\ogste>ping 192.168.0.1

Pinging 192.168.0.1 with 32 bytes of data:
Reply from 192.168.0.1: bytes=32 time<1ms TTL=64
Reply from 192.168.0.1: bytes=32 time=1ms TTL=64
Reply from 192.168.0.1: bytes=32 time=1ms TTL=64
Reply from 192.168.0.1: bytes=32 time=1ms TTL=64

Ping statistics for 192.168.0.1:
    Packets: Sent = 4, Received = 4, Lost = 0 (0% loss),
    Approximate round trip times in milli-seconds:
        Minimum = 0ms, Maximum = 1ms, Average = 0ms

C:\Users\ogste>ping 192.168.0.2

Pinging 192.168.0.2 with 32 bytes of data:
Reply from 192.168.0.2: bytes=32 time=1ms TTL=64
Reply from 192.168.0.2: bytes=32 time=1ms TTL=64
Reply from 192.168.0.2: bytes=32 time=1ms TTL=64
Reply from 192.168.0.2: bytes=32 time=1ms TTL=64

Ping statistics for 192.168.0.2:
    Packets: Sent = 4, Received = 4, Lost = 0 (0% loss),
    Approximate round trip times in milli-seconds:
        Minimum = 1ms, Maximum = 1ms, Average = 1ms

C:\Users\ogste>ping 192.168.0.101

Pinging 192.168.0.101 with 32 bytes of data:
Reply from 192.168.0.101: bytes=32 time=1ms TTL=100
Reply from 192.168.0.101: bytes=32 time<1ms TTL=100
Reply from 192.168.0.101: bytes=32 time=1ms TTL=100
Reply from 192.168.0.101: bytes=32 time<1ms TTL=100

Ping statistics for 192.168.0.101:
    Packets: Sent = 4, Received = 4, Lost = 0 (0% loss),
    Approximate round trip times in milli-seconds:
        Minimum = 0ms, Maximum = 1ms, Average = 0ms
```

Figure 73: All pings from notebook to check the connections